PHYSIK-DEPARTMENT

Zentralinstitut für Medizintechnik

Efficient Acquisition Strategies for Nuclear Magnetic Resonance Imaging with Hyperpolarised Biomarkers

Markus Durst

Vollständiger Abdruck der von der Fakultät für Physik der Technischen Universität München zur Erlangung des akademischen Grades eines

Doktors der Naturwissenschaften (Dr. rer. nat.)

genehmigten Dissertation.

Vorsitzender: Prof. Dr. Martin Zacharias

Prüfer der Dissertation:
      1. Prof. Dr. Axel Haase
      2. Prof. Dr. Franz Pfeiffer

Die Dissertation wurde am 24.11.2015 bei der Technischen Universität München eingereicht und durch die Fakultät für Physik am 14.09.2016 angenommen.

"Wahrlich es ist nicht das Wissen, sondern das Lernen, nicht das Besitzen sondern das Erwerben, nicht das Da-Seyn, sondern das Hinkommen, was den grössten Genuss gewährt."
Carl Friedrich Gauß

Abstract

Dynamic nuclear polarisation (DNP) with subsequent dissolution can increase the nuclear magnetic resonance (NMR) signal of certain biomarkers by several orders of magnitude, thus permitting the investigation of a wide range of diseases. As a result of the substantial differences between acquisitions with hyperpolarised compounds and conventional thermal magnetic resonance imaging (MRI), the design and optimisation of imaging sequences currently constitutes a highly active field of research. During the short lifetime of the hyperpolarised signal, a wealth of information such as the spatial distribution and the metabolic conversion of the hyperpolarised substrate has to be encoded. Therefore, fast and efficient imaging pulse sequences must be developed. The goal of the research described in this thesis was to improve current imaging methods for acquisitions with hyperpolarised biomarkers, and to apply these improved techniques to preclinical in vivo studies in order to validate their performance. My research is structured in five sections:

- An extensive comparison of existing pulse sequences for hyperpolarised agents is conducted in order to reveal their strengths and weaknesses and to find general guidelines for pulse sequence design in this field.

- A bolus tracking sequence that evaluates the hyperpolarised signal in real-time is presented. It is shown that this method reduces artefacts caused by signal change, allows to use the hyperpolarised magnetisation more efficiently and enables a more reliable and consistent evaluation of metabolic activity.

- A spiral chemical shift imaging sequence for cardiac imaging in healthy pigs after injection of hyperpolarised [1-^{13}C]pyruvate is described. The potential for parallel imaging reconstructions is explored using in vivo data from healthy pigs.

- First in vivo tests of a novel hyperpolarised perfusion marker with an especially long spin-lattice relaxation time, α-trideuteromethyl[^{15}N]glutamine, are reported. This marker is demonstrated to be a highly promising candidate for renal studies because of its long signal lifetime, distinct localisation and rapid excretion.

- A new method to measure cell membrane transport in vivo for the first time using hyperpolarised biomarkers in combination with a tailored relaxation agent is introduced. Indications of high lactate efflux rates are shown in rats with mammary carcinoma after injection of hyperpolarised [1-^{13}C]pyruvate.

Beginning with advanced pulse sequence design and reconstruction methods, a broad spectrum of biomedical applications is discussed and new methods to improve the diagnostic value of hyperpolarised examinations are presented. These contributions are highly relevant for the application of the DNP technique in preclinical studies, and also for its ongoing translation to clinical applications.

Kurzzusammenfassung

Die dynamische nukleare Polarisation (DNP) mit anschließendem Lösungsprozess kann das Magnetresonanz-Signal von speziellen Biomarkern um mehrere Größenordnungen erhöhen und ermöglicht es dadurch, ein breites Spektrum an Krankheitsbildern zu erforschen. Durch die großen Unterschiede im Vergleich zu herkömmlicher thermischer Magnetresonanzbildgebung stellen die Entwicklung und Optimierung von neuen Bildgebungssequenzen ein höchst aktives Forschungsfeld dar. Innerhalb der kurzen Lebensdauer des hyperpolarisierten Signals müssen vielfältige Informationen wie etwa die räumliche Verteilung und die metabolische Umwandlung des hyperpolarisierten Substrats kodiert werden. Dies erfordert schnelle und effiziente Aufnahmestrategien. Das Ziel dieser Arbeit war es, bestehende Bildgebungsmethoden für Untersuchungen mit hyperpolarisierten Biomarkern zu verbessern und diese verbesserten Methoden in präklinischen Studien anzuwenden. Meine Forschung gliedert sich in fünf Teile:

- Ein tiefgehender Vergleich von existierenden Pulssequenzen für hyperpolarisierte Stoffe wird durchgeführt, um die jeweiligen Stärken und Schwächen der Methoden zu charakterisieren.

- Eine vollautomatische Echtzeit-Pulssequenz für hyperpolarisierte Substrate wird präsentiert, welche die Bildgebung an einem vordefinierten Punkt der Boluskurve startet. Dies reduziert Artefakte, ermöglicht eine effizientere Nutzung der hyperpolarisierten Magnetisierung und stellt eine verlässlichere und konsistentere Möglichkeit zu Quantifizierung des Metabolismus dar.

- Eine spektroskopische Bildgebungssequenz mit Spiraltrajektorien zur Herzbildgebung mit hyperpolarisiertem Pyruvat wird beschrieben. Mittels Daten von gesunden Schweinen werden die Vor- und Nachteile von paralleler Bildgebung erörtert.

- Die ersten in vivo Versuche mit einem neuen hyperpolarisierten Perfusionsmarker, α-trideuteromethyl[^{15}N]glutamin, werden vorgestellt. Es wird gezeigt, dass dieses Molekül durch seine sehr lange Relaxationszeit, ausgeprägte Lokalisierung und rasche Ausscheidung einen vielversprechenden Kandidaten für Nierenstudien darstellt.

- Eine neue Methode zur Messung von Zellmembrantransport in vivo mit hyperpolarisierten Biomarkern in Kombination mit einem speziellen Kontrastmittel wird eingeführt und an einem Tumormodell in Ratten erprobt.

Ausgehend von hochentwickelten Pulssequenz- und Rekonstruktionsmethoden werden eine Vielzahl an biomedizinischen Anwendungen behandelt und neue Methoden präsentiert welche den diagnostischen Wert von Untersuchungen mit hyperpolarisierten Biomarkern erhöhen. Diese Fortschritte sind höchst relevant für die Anwendung von DNP in präklinischen Studien und die andauernde Umsetzung für klinische Anwendungen.

Contents

1 Introduction

1.1 Motivation and Outline of the PhD Thesis

Over recent decades, magnetic resonance imaging (MRI) [1, 2] has evolved into a routine clinical tool for the non-invasive investigation of many aspects of anatomy and physiology. It works by exploiting the interaction of certain atomic nuclei with magnetic fields to obtain image contrast. Most medical applications focus on the hydrogen isotope ^{1}H, as it is detectable by MRI methods and highly abundant in the human body. Unlike X-ray-based computed tomography (CT) methods, MRI does not rely on ionising radiation and no long-term health risks are known. With its unparalleled soft tissue contrast and its flexibility to generate many different contrast types through variation of the acquisition parameters, it has a wide range of applications in medical diagnosis. Its primary fields of use include neurological, cardiovascular, musculoskeletal, gastrointestinal and oncological examinations.

Furthermore, magnetic resonance spectroscopy (MRS) is applicable to the examination of in vivo tissue metabolism [3, 4]. However, due to the low metabolite concentration and the corresponding low sensitivity of MRS, the clinical use of this technique is limited. Recently, dynamic nuclear polarisation (DNP) with subsequent dissolution has demonstrated an NMR signal increase of several 10.000-fold for endogenous biomarkers [5], allowing to non-invasively detect metabolism in real-time in a living organism. Early preclinical studies have since introduced a multitude of applications for the examination of various disease states such as cancer, necrosis, cardiovascular diseases, and pH alterations [6]. However, the signal of these hyperpolarised biomarkers rapidly decays after the hyperpolarisation process. Moreover, a wealth of information such as the spatial distribution and the time evolution of the hyperpolarised signals has to be encoded. Therefore, fast and efficient imaging pulse sequences must be developed. Moreover, as the signal reflects not only the metabolic conversion, but also other biological processes such as perfusion, cellular uptake, and label exchange of different endogenous pools, new methods for distinguishing these contributions are required.

This PhD thesis presents efficient acquisition strategies for nuclear magnetic resonance imaging with hyperpolarised biomarkers. In **chapter 2**, a general introduction to nuclear magnetic resonance, dynamic nuclear polarisation and other topics relevant for the research described in this thesis is given.

As a first project, in **chapter 3**, four of the most widely used acquisition strategies for hyperpolarised ^{13}C imaging are characterised and compared in extensive simulations. Free induction decay chemical shift imaging (FIDCSI) [7–12], echo-planar spectroscopic imaging (EPSI) [13–17], IDEAL spiral chemical shift imaging (ISPCSI) [18–21] and spiral chemical shift imaging (SPCSI) [22–27] sequences were analysed for theoretical efficiency, SNR and artefact behaviour. The goal was to reveal the strengths and weaknesses of the individual sequences and to reach general conclusions regarding sequence design for imaging hyperpolarised biomarkers.

Chapter 4 presents a real-time bolus tracking method for improved metabolic imaging

of hyperpolarised compounds. Varying levels of perfusion can significantly influence the quality and reliability of conventional hyperpolarised imaging acquisitions that use fixed parameters. Unfavorable timing of the measurement can cause artefacts, decrease the signal-to-noise ratio, and hinder the assessment of metabolic activity. The described bolus tracking sequence evaluates the hyperpolarised signal in real-time and dynamically adjusts the starting point of the imaging acquisition based on the bolus curve of the hyperpolarised substrate.

In **chapter 5**, a spiral chemical shift imaging sequence is described which was applied to cardiac imaging of healthy pigs after injection of hyperpolarised [1-^{13}C]pyruvate. A flexible 16-channel ^{13}C coil was used for data reception. Multiple interleaves were sampled in order to study the quality of non-Cartesian parallel imaging reconstructions with different undersampling factors. The goal of this particular study was to investigate the potential of parallel imaging in the context of hyperpolarised cardiac acquisitions, and also to identify conditions in which parallel imaging will be beneficial in future clinical trials.

Next, in **chapter 6**, a novel hyperpolarised perfusion marker, α-trideuteromethyl[^{15}N]glutamine [28], was characterised and directly compared to [^{13}C]urea for the first time in vivo. Hyperpolarised agents based on ^{13}C have exhibited considerable potential for a wide variety of biomedical applications, however, their in vivo lifetimes are relatively short compared to the rates of many physiological processes. α-trideuteromethyl[^{15}N]glutamine exhibits a very long T_1 relaxation time as a result of its molecular structure and is therefore a promising candidate for in vivo studies.

In **chapter 7**, noninvasive in vivo measurement of cell membrane transporter activity is demonstrated using hyperpolarised pyruvate in combination with a tailored relaxation agent. Cancer cells usually exhibit an increased conversion from pyruvate to lactate in order to generate energy. To maintain this process, the cells need to rapidly export the generated lactate via specialised cell membrane transporter proteins. Therefore, characterising this transport is vital for a better evaluation of tumour metabolism and the hyperpolarised signal kinetics of pyruvate.

Chapter 8 discusses the future prospects of magnetic resonance imaging with hyperpolarised biomarkers. The current state of the technique is described and its advantages and disadvantages compared to positron emission tomography (PET) [29] are mentioned. Finally, **Chapter 9** summarises the results of this thesis and contains final conclusions.

1.2 Historical Overview

When the discovery that spectral lines are split within a magnetic field was made at the end of the 19th century [30], it is unlikely that anyone was aware that this finding would eventually lead to one of the most powerful diagnostic imaging methods to date: Nuclear magnetic resonance imaging (MRI).

At the beginning of the 20th century, a large number of phenomena that could not be described by established theories were discovered on the nanoscopic scale, which led to an entirely new branch of physics called quantum mechanics. Among the many strange characteristics of subatomic particles, the intrinsic angular momentum or so-called "spin"

became especially important for scientists, as it is associated with a magnetic moment and can therefore interact with magnetic fields. In 1938, Rabi et al. reported on the absorption of an oscillating magnetic field by a molecular beam of lithium chloride traversing a static magnetic field of specific magnitude, a phenomenon Rabi called "nuclear magnetic resonance" (NMR) [31]. In 1946, Bloch and Purcell independently studied this effect for the first time in solids and liquids [32, 33]. Shortly afterwards, it was discovered that nuclei exhibit a shifted resonance frequency depending on their chemical environment [34, 35], the so called "chemical shift", which allows individual molecular configurations to be identified. In 1966, Ernst advanced this technology to a new level by introducing pulsed NMR and a theoretical formulation based on the Fourier transform [36]. Since then, NMR spectroscopy has become one of the most important techniques in chemistry and biology to investigate molecules.

As optical imaging resolution is limited by wavelength, and NMR typically involves wavelengths of the order of a metre, traditional imaging methods are impractical. Almost three decades passed before Lauterbur [1] and Mansfield [2] presented methods to perform spatially resolved NMR experiments by employing position-dependent magnetic fields. This was the birth of magnetic resonance imaging, which quickly became one of the most important medical imaging techniques. Compared to X-ray computed tomography (CT) methods, MRI yields soft body tissue images with superior contrast and does not rely on ionising radiation.

However, NMR methods have an inherently low sensitivity because the energy levels of the spins in the magnetic field are almost equally populated due to thermal interactions. To obtain a higher detectable magnetisation, the population difference between the spin states can be increased using so-called hyperpolarisation methods. Various techniques have been developed, such as the optical pumping of noble gases [37], hyperpolarisation induced by chemical reactions (CIDNP [38], PHIP [39]), and the transfer of electron polarisation to nuclei (DNP) [40]. DNP of frozen samples with subsequent dissolution was introduced by Ardenkjær-Larsen et al. [5] in 2003. It can provide a signal increase by four orders of magnitude, permitting in vivo studies with hyperpolarised biomarkers. Based on this technology, a multitude of substrates have been studied in preclinical trials [6]. One of the most promising candidates is [1-^{13}C]pyruvate, which has been used to study cell energy metabolism in vivo for various disease states such as cancer [7] and ischemia [41]. Currently, the technique is being translated to clinical applications [42].

2 Basic Principles of Magnetic Resonance Imaging with Hyperpolarised Biomarkers

2.1 NMR Basics

2.1.1 Nuclear Spin and Magnetic Moment

Elementary particles and their composites possess an intrinsic angular momentum, the so-called "spin" [43]. Unlike angular momentum in classical mechanics, the spin $\mathbf{S}$ is quantised and its amplitude S can occupy discrete values only, with

$$S = \left(\frac{h}{2\pi}\right)\sqrt{I(I+1)} \tag{1}$$

where I is the spin quantum number which can take integer or half-integer values only, and h is Planck's constant. The component of the spin along the z direction, S_z, is given by:

$$S_z = \left(\frac{h}{2\pi}\right)m \tag{2}$$

where m is the secondary spin quantum number which can range from $-I$ to $+I$ in steps of one. This means there are $2I + 1$ different orientations for the spin along the z-axis.

Consequently, an atomic nucleus can have a nuclear spin formed by the coupling of the spins of its protons and neutrons. Depending on the structure of the nucleus, the spin quantum number can be zero (an even number of protons and an even number of neutrons), half-integer (an odd total number of neutrons plus protons) or integer (an odd number of neutrons and an odd number of protons). The spin is associated with a magnetic dipole moment $\boldsymbol{\mu}$ such that

$$\boldsymbol{\mu} = \gamma \mathbf{S} \tag{3}$$

where γ is termed the gyromagnetic ratio which depends on the specific nucleus.

Nucleus	I	gyromagnetic ratio $\frac{\gamma}{2\pi}[\frac{\text{MHz}}{\text{T}}]$	natural abundance [%]
^{1}H	$\frac{1}{2}$	42.58	99.98
^{2}H	1	6.54	0.02
^{12}C	0	-	98.89
^{13}C	$\frac{1}{2}$	10.71	1.11
^{14}N	1	3.08	99.63
^{15}N	$\frac{1}{2}$	-4.32	0.37

Table 1: Properties related to NMR of several isotopes (data from [43, 44])

2.1.2 Nuclear Zeeman Splitting

A magnetic moment $\boldsymbol{\mu}$ in an external magnetic field $\mathbf{B_0}$ has a magnetic energy E defined by

$$E = -\boldsymbol{\mu}\mathbf{B_0} \tag{4}$$

The quantisation of the spin states results in a quantisation of energy levels in a magnetic field. For a nucleus with $I = \frac{1}{2}$ (such as ^{1}H), two energy levels can be observed so that the energy difference ΔE between the two states $E_{\pm\frac{1}{2}}$ is given by

$$\Delta E = E_{-\frac{1}{2}} - E_{+\frac{1}{2}} = \hbar\gamma B_0 = \hbar\omega_0 \tag{5}$$

where $\hbar = \frac{h}{2\pi}$. This effect is known as nuclear Zeeman splitting [30]. Transitions between these energy states can occur via emission or absorption of a photon with the Larmor frequency ω_0.

$$\omega_0 = \gamma B_0 \tag{6}$$

The population of the different spin states in thermal equilibrium is then given by the Boltzmann distribution

$$\frac{n_{+\frac{1}{2}}}{n_{-\frac{1}{2}}} = e^{\left(\frac{\Delta E}{k_B T}\right)} = e^{\left(\frac{\gamma\hbar B_0}{k_B T}\right)} \tag{7}$$

where n_m denotes the occupation of the energy level m, k_B is the Boltzmann constant, and T is the temperature [45].

At 3 T and 37 °C (310 K), a population difference of only ≈ 10 ppm and ≈ 2 ppm for ^{1}H and ^{13}C can be observed, respectively. This is the reason why NMR is an inherently insensitive technique.

2.1.3 Chemical Shift

Besides the external magnetic field $\mathbf{B_0}$ and the gyromagnetic ratio γ, the Larmor frequency depends also on the molecular environment of the nucleus under investigation. The so-called chemical shift [34, 35] is caused by the different distribution of electrons surrounding the nucleus in a molecule, shielding the external magnetic field $\mathbf{B_0}$. This phenomenon is especially important for metabolic NMR measurements because it allows to distinguish between different metabolites.

In order to obtain a unit that does not depend on the strength of the external magnetic field, the chemical shift δ is usually defined in ppm such that

$$\delta = \frac{\omega - \omega_{ref}}{\omega_{ref}} \tag{8}$$

where ω and ω_{ref} are the measured Larmor frequency and a reference frequency, respectively. Usually, tetramethylsilane is used to reference 0.0 ppm for ^{13}C and ^{1}H NMR spectroscopy. The chemical shifts of some of the most important ^{13}C compounds that are used as hyperpolarised biomarkers can be found in Table 2 below.

6

Molecule	Chemical shift [ppm]
[1-^{13}C]pyruvate	171
[1-^{13}C]pyruvate hydrate	179
[1-^{13}C]lactate	182
^{13}C bicarbonate	161
^{13}C carbon dioxide	125

Table 2: Chemical shifts of [1-^{13}C]pyruvate and its metabolites (from [46])

2.1.4 Radiofrequency Excitation

At thermal equilibrium, the individual spins in a macroscopic sample are distributed over the surfaces of two cones (in the case of spin 1/2 particles) with parallel and anti-parallel orientation with respect to the static magnetic field $\mathbf{B_0}$ and precess around it with the Larmor frequency ω_0. A small surplus of spins can be found on the energetically favorable cone, however, the phase is randomly distributed. In a classical picture, this can be understood as a macroscopic net magnetisation along the static magnetic field (for $\gamma > 0$). If an oscillating magnetic field $\mathbf{B_1}$ with frequency ω_0 perpendicular to $\mathbf{B_0}$ is activated, the thermal equilibrium is disturbed and phase coherence is generated. The macroscopic magnetisation vector is tipped off axis and begins precessing around $\mathbf{B_0}$. The combined motion induced by the static magnetic field $\mathbf{B_0}$ and the oscillating magnetic field $\mathbf{B_1}$ results in a spiral motion of the tip of the magnetisation vector $\mathbf{M_0}$ on the surface of a sphere (Figure 1). If $\mathbf{B_1}$ is activated for a time τ_{RF}, $\mathbf{M_0}$ is deflected by an angle $\alpha = \gamma B_1 \tau_{RF}$, yielding a transverse magnetisation $M_{x,y}$ perpendicular to $\mathbf{B_0}$.
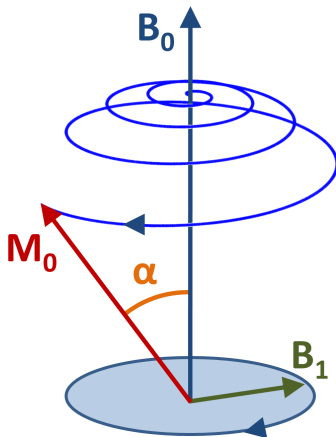
Figure 1: Effect of a radio frequency (RF) pulse $\mathbf{B_1}$ on a magnetisation vector $\mathbf{M_0}$ in a static magnetic field $\mathbf{B_0}$. $\mathbf{M_0}$ follows a spiral trajectory on the surface of a sphere, thus being tipped by an angle α relative to $\mathbf{B_0}$ (Figure based on [47]).

The precessing transverse magnetisation induces an oscillating voltage in a receiver coil circuit that is tuned to the respective Larmor frequency. Along with sufficient electronic

amplification, this allows the NMR signal to be measured after RF excitation.

2.1.5 Relaxation

As described above, a radiofrequency pulse at the Larmor frequency creates a non-equilibrium state with a measurable transverse magnetisation. After perturbation by the oscillating magnetic field $\mathbf{B_1}$, the spin system returns to its initial state, which can be phenomenologically described by an exponential decay model with associated relaxation time constants.

The relaxation of the longitudinal magnetisation is called the "spin-lattice relaxation", as it is caused by energy loss from the spins to the molecular environment. It is commonly identified with the time constant T_1. Because of thermal motion and field variations at the microscopic level induced by surrounding molecules, the spins are exposed to a slightly fluctuating magnetic field. When the fluctuations occur near the Larmor frequency, transitions between the spin's energy states are triggered, causing relaxation.

On the other hand, the transverse magnetisation decays as a result of the so-called "spin-spin relaxation", which means the loss of phase coherence within the spin ensemble due to local magnetic field variations. Different local magnetic fields result in a different Larmor frequency, and therefore in a different phase evolution within a sample. Thus, the individual spins do not align to a macroscopic magnetisation vector any more. This relaxation type is characterised by the time constant T_2. Due to the nature of this process, spin-spin relaxation can not only be caused by fluctuating local magnetic field variations, but also by static local magnetic field variations; therefore, $T_2 < T_1$.

In addition, variations of the static magnetic field $\mathbf{B_0}$ itself can cause dephasing of the transverse magnetisation. This is described by a characteristic relaxation time constant T_2^* where $T_2^* < T_2$.

Tissue-dependent variations in relaxation are one of the main reasons for the unparalleled flexibility of magnetic resonance imaging, which allows to generate many different contrast types. By varying the acquisition timings, either T_1, T_2 or spin-densitiy weighted images can be generated.

2.1.6 Bloch Equations

The empirical Bloch equations [33] describe the change of the macroscopic magnetisation vector $\mathbf{M(t)}$ in the presence of an arbitrary magnetic field $\mathbf{B(t)}$ and relaxation processes.

$$
\begin{aligned}
\frac{dM_x(t)}{dt} - \gamma(\mathbf{M(t)} \times \mathbf{B(t)})_x + \frac{M_x(t)}{T_2} &= 0 \\
\frac{dM_y(t)}{dt} - \gamma(\mathbf{M(t)} \times \mathbf{B(t)})_y + \frac{M_y(t)}{T_2} &= 0 \\
\frac{dM_z(t)}{dt} - \gamma(\mathbf{M(t)} \times \mathbf{B(t)})_z + \frac{M_z(t) - M_0}{T_1} &= 0
\end{aligned}
\tag{9}
$$

In this set of equations, the second term describes the Larmor precession, which is similar to the application of a classical torque to the magnetisation $\mathbf{M(t)}$ by the magnetic field

$\mathbf{B(t)}$, and the third term describes the transverse and longitudinal relaxation.

2.2 Magnetic Resonance Imaging

2.2.1 Signal Encoding

Since the Larmor frequency is typically in the radio frequency range which corresponds to wavelengths of the order of a metre, optical imaging approaches are not possible with NMR methods at sufficient resolutions. To obtain the spatial distribution of the spins from the measured NMR signal, additional magnetic fields that vary linearly over space are used [1, 2]. When a constant magnetic field gradient is activated along an arbitrary axis, the amplitude of the static magnetic field varies linearly along this axis, and with it the Larmor frequency of the spins.
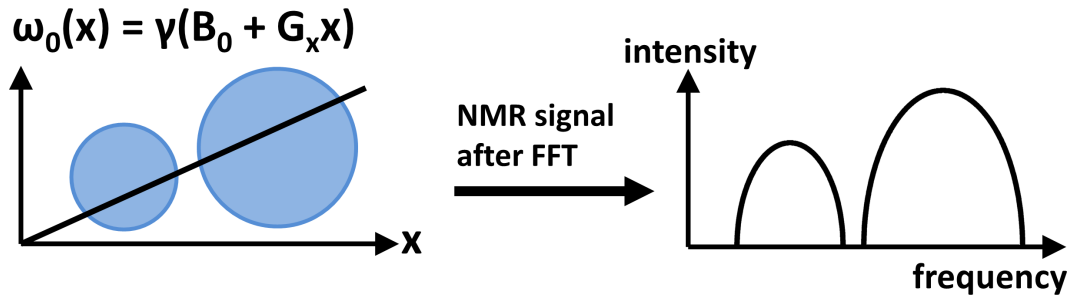
Figure 2: Effects of a constant magnetic field gradient G_x on the Larmor frequency along x and corresponding NMR signal after fast Fourier transform (FFT). Figure based on [48].

Together with a narrow-band RF excitation pulse, this can also be used to excite only spins from a defined slice perpendicular to the gradient axis that have the Larmor frequency corresponding to the RF pulse. To acquire a 3D distribution of spins within the excited volume, magnetic field gradients along all three dimensions can be used to create a position-dependent phase. According to Equation 5, the position-dependent Larmor frequency in the presence of a magnetic field gradient $\mathbf{G}(t)$ is given by

$$\omega_0(\mathbf{r}, t) = \gamma(\mathbf{B}_0 + \mathbf{rG}(t)) \tag{10}$$

If the precessing transverse magnetisation is expressed as $M_{x,y}(\mathbf{r}, t) = \rho(\mathbf{r})e^{-i\int_0^t \omega_0(\mathbf{r},t')\,dt'}$, the basic signal equation of an ideal MRI experiment of a single resonance at time t can be derived such that

$$s(t) = \int_V \rho(\mathbf{r})e^{i2\pi\mathbf{k}(t)\cdot\mathbf{r}}\,d^3r \tag{11}$$

$$\text{with } \mathbf{k}(t) = \frac{\gamma}{2\pi}\int_0^t \mathbf{G}(t')\,dt'$$

9

where $\rho(\mathbf{r})$ is proportional to the local spin density (neglecting relaxation), γ is the gyromagnetic ratio and $\mathbf{G}(t')$ is the gradient field.

This means that the measured signal is simply the Fourier transform of $\rho(\mathbf{r})$ at the frequency coordinate $\mathbf{k}(t)$ determined by the magnetic field gradients. The Fourier domain for magnetic resonance imaging is usually termed the k-space [49], and the integral over the gradients can be interpreted as a trajectory traversing k-space. The obtained field of view (FOV) then depends on the reciprocal sampling density, whereas the resolution is determined by the highest acquired spatial frequency (see also Section 2.2.2). To calculate $\rho(\mathbf{r})$ from the measured signal, an inverse Fourier transform can be employed.

For chemical shift imaging, multiple frequencies f originating from different molecules are present (see Section 2.1.3). In this case, the sampling must also be extended to the time dimension, so that the different chemical species can be resolved; this is usually achieved by measuring the same k-space point at multiple points in time. The extended signal equation is then given by

$$s(t) = \int\limits_F \int\limits_V \rho(\mathbf{r}, f) e^{i2\pi \mathbf{k}(t) \cdot \mathbf{r}} e^{i2\pi ft} \, d^3r \, df \tag{12}$$

where $\rho(\mathbf{r}, f)$ is now not only dependent on the spatial position, but also on the frequency f. Again, a multidimensional Fourier transform can be used to obtain $\rho(\mathbf{r}, f)$.

2.2.2 Nyquist-Shannon Sampling Theorem

The Nyquist-Shannon sampling theorem [50] states that, in order to perfectly recover a bandlimited signal with maximum frequency f_{max} from discrete samples, the sampling frequency f_s must fulfill the condition in Equation 13.

$$f_s \geq 2f_{max} \tag{13}$$

For the sampling rate in k-space, this means that data must be sampled at intervals smaller than $\frac{1}{FOV}$ to obtain an image for a desired field of view FOV. Otherwise, signals originating from outside the permitted FOV cannot be properly reconstructed, leading to artefacts in the image. The physical interpretation is that the phase of the spins can no longer be uniquely associated with a spatial position because spins within and without the allowed FOV exhibit an indistinguishable phase evolution at a sampling rate below the Nyquist frequency. For Cartesian sampling schemes, undersampling manifests as a folding inwards of the parts of the image that are outside the allowed FOV (see Figure 3). For non-Cartesian trajectories such as spirals, aliasing artefacts appear in the form of blurring and streaks.
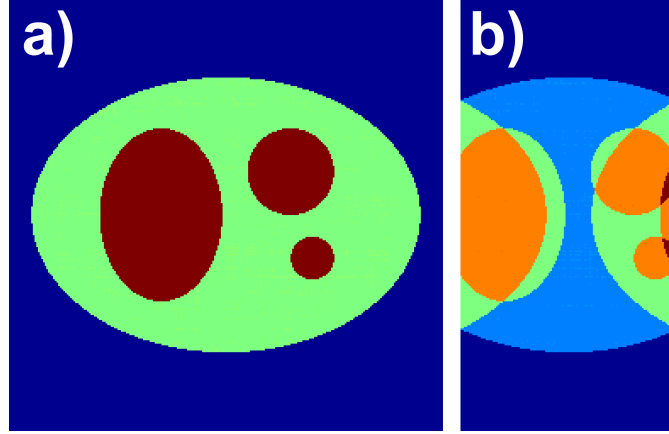
Figure 3: Standard Cartesian phase-encoded acquisition: a) fully sampled k-space, b) under-sampled k-space along horizontal axis

2.2.3 Spectral-Spatial Excitation Pulses

As discussed in Section 2.2.1, a frequency-selective RF pulse in combination with an applied magnetic field gradient can be used to perform a slice-selective excitation of spins along one spatial dimension. However, in some cases, RF pulses that are selective along multiple dimensions are required, for example, along one spatial dimension and also the spectral dimension. The excitation k-space formalism [51] facilitates an intuitive understanding of the functionality of the pulse and can be used to design such pulses in a straight-forward manner. Using an approximation for small flip angles, it follows directly from the Bloch equations that the transverse magnetisation $M_{xy}(r)$ under the influence of an RF field with amplitude $B_1(t)$ and a magnetic field gradient $\mathbf{G}(t)$ for the period τ can be described as

$$M_{xy}(r) = i\gamma M_0 \int_{\mathbf{K}} W(\mathbf{k})S(\mathbf{k})e^{i\mathbf{r}\cdot\mathbf{k}}\,d\mathbf{k} \tag{14}$$

$$\text{with } W(\mathbf{k}(t)) = \frac{B_1(t)}{|\gamma\mathbf{G}(t)|},\ \ S(\mathbf{k}) = \int_0^\tau \delta(\mathbf{k}(t)-\mathbf{k})\left|\frac{d\mathbf{k}(t)}{dt}\right|\,dt$$

where W is a time-independent spatial weighting function and S is a sampling structure that selects values lying on the k-space trajectory $\mathbf{k}(t)$ only [51]. This description is very similar to the readout k-space formalism presented in Equation 11, the excitation can be understood as scanning the applied RF energy in acquisition k-space, and the same design principles apply to the sampling regarding resolution and the Nyquist criterion.

For a spectral-spatial pulse, the k-space dimensions can be defined as

$$k_z(t) = -R\int_t^\tau G_z(t')\,dt',\ \ k_\omega(t) = t - \tau \tag{15}$$

where $k_z(t)$ is the spatial dimension with applied gradient $G_z(t)$, R is a constant mediating the natural units of the axes and $k_\omega(t)$ is the spectral dimension [52].

If a trajectory that sufficiently samples k-space along both dimensions is chosen, for example an EPSI trajectory (see Chapter 3), the desired RF waveform can be deduced from Equation 14. As the waveform used on the scanner is discrete, it is possible to solve this problem as a least-squares matrix inversion (see [53]). The spectral-spatial pulse used in Chapter 7 is shown below.
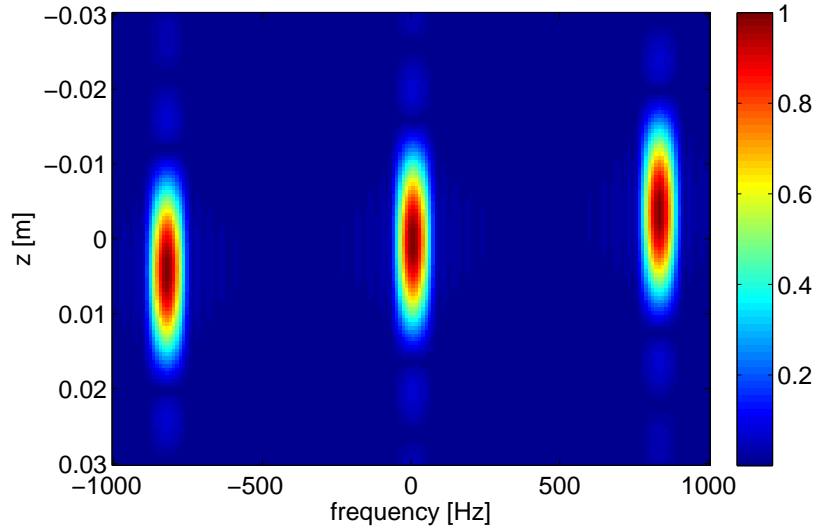
Figure 4: Simulated pulse profile for spectral-spatial RF excitation pulse: Slice thickness 14 mm, 85 Hz spectral bandwidth, 18 sublobes, flyback EPSI trajectory, pulse length 22.4ms.
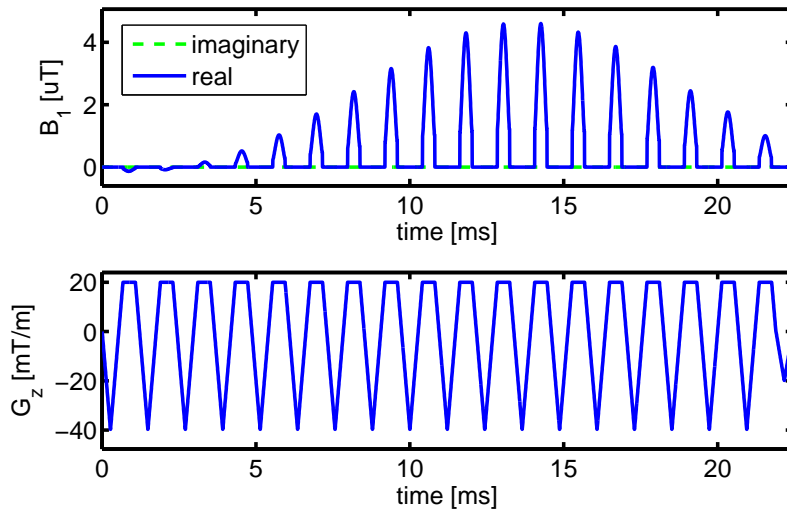
Figure 5: RF and gradient waveforms for spectral-spatial pulse shown in Figure 4

Pulses of this nature were first applied to the problem of fat-water separation in proton imaging [52, 54]. For hyperpolarised acquisitions, spectral-spatial pulses can help to spend the non-renewable magnetisation more efficiently [16, 55–57] by exciting the metabolite frequencies with a higher flip angle than the substrate frequency, because the substrate signal is usually much stronger. The pulse can either be designed to excite multiple species at different flip angles, or to perform a selective excitation on a single frequency, thereby removing the need for chemical shift separation via k-space encoding. The disadvantages of these pulses include increased T_2^* decay because of their length, along with susceptibility to gradient errors and B_0 inhomogeneities.

2.2.4 Pulse Sequences

As a comprehensive overview of MRI acquisition strategies is beyond the scope of this introduction, only two of the most essential pulse sequences, the spin echo sequence and the gradient echo sequence, are presented in the following. An extensive treatment of pulse sequence design is provided in [58], for example.

Spin Echo Sequence
After excitation, the transverse magnetisation decays with T_2^* as a result of spin-spin relaxation and additional dephasing caused by local inhomogeneities of the static magnetic field B_0. For the spin echo sequence, a 180° pulse is applied after a time of $\frac{T_E}{2}$ has passed relative to the excitation pulse. A 180° rotation of the transverse magnetisation corresponds to a reflection across the axis of rotation, therefore, the individual spins resynchronise after another period of $\frac{T_E}{2}$ when the accumulated phase differences caused by the B_0 inhomogeneity cancel. As a consequence, the signal will rise again and a so-called spin echo appears. The characteristic time T_E is therefore called the echo

time. This process can be repeated several times, until the signal has decayed with T_2 due to spin-spin relaxation. In between the excitation pulses, readout gradients can be applied for spatial encoding [59].
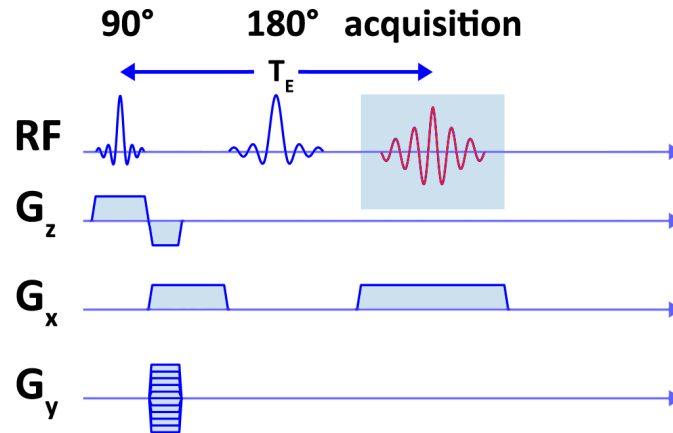
Figure 6: Spin echo sequence scheme, not to scale for illustration purposes (adapted from [60])

Gradient Echo Sequence

The gradient echo sequence creates an echo by de- and rephasing the magnetisation via the magnetic field gradients without employing a 180° pulse. Therefore, the signal decays with T_2^*.
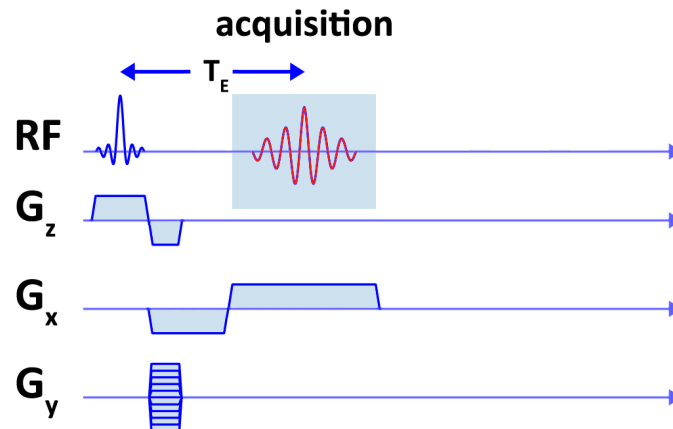
Figure 7: Gradient echo sequence scheme, not to scale for illustration purposes (adapted from [60])

Gradient echo acquisitions can be fast if performed with low flip angles because, for small flip angles α, most of the longitudinal magnetisation remains untouched ($\propto \cos(\alpha)$) while at the same time sufficient transverse magnetisation is generated ($\propto \sin(\alpha) > 1 - \cos(\alpha)$). Therefore, short repetition times T_R can be used because the longitudinal magnetisation does not have to completely build up again [61].

2.3 Parallel Magnetic Resonance Imaging

Parallel magnetic resonance imaging (PMRI) is a technique that can considerably accelerate the acquisition process. The complementary information obtained from multiple receiver coils with spatially varying sensitivity profiles can be used to reconstruct data sampled below the Nyquist limit. When a sample is measured with an array of multiple receiver coils, each coil receives different intensity values from a given voxel, depending on the alignment of the coils and their sensitivity profiles. This complementary information can be used to reconstruct the original image without artefacts. An overview of existing parallel imaging techniques can be found for example in [62]. In the following, two exemplary parallel imaging algorithms are presented.
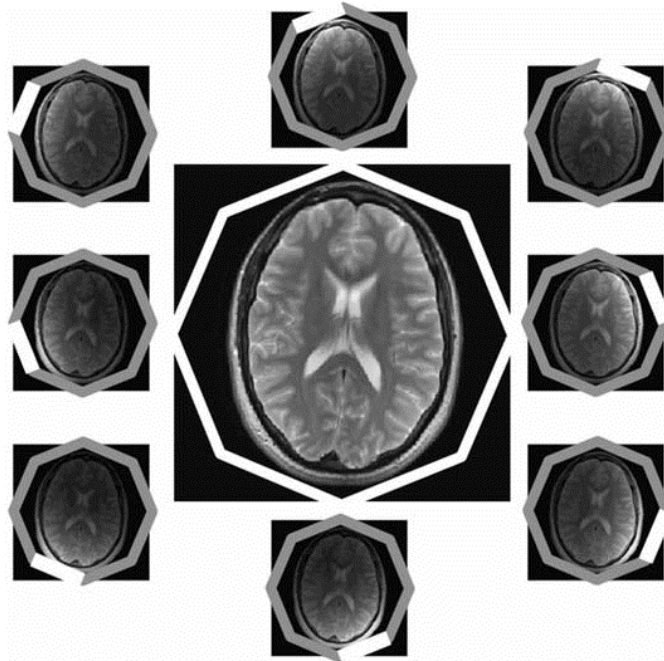
Figure 8: Brain scan with an eight-channel receiver array and respective single coil images with spatially varying sensitivity profiles (from [63], reprinted with permission of John Wiley and Sons. Copyright 2012 John Wiley and Sons.)

2.3.1 SENSE

SENSitivity Encoding (SENSE), developed by Pruessmann et al. [64], is one of the most widely used image-based parallel imaging algorithms. It requires the coil sensitivities to be known, which can be measured using a homogeneous phantom or a calibration scan of the sample prior to the parallel imaging acquisition. The algorithm can be intuitively understood through examination of the signal equations.

For a Cartesian k-space sampling pattern which is undersampled by a factor of R along the y-axis, an image pixel at (x, y) is superimposed with pixels from other locations

(x, y_i) because of aliasing. The signal from coil k for a single pixel at (x, y) is then given by [62]

$$I_k(x, y) = C_k(x, y_1)\rho(x, y_1) + C_k(x, y_2)\rho(x, y_2) + \ldots + C_k(x, y_R)\rho(x, y_R) \qquad (16)$$

where $C_k(x, y)$ is the coil sensitivity profile of coil k and $\rho(x, y_i)$ are the original image pixels without aliasing. This can also be expressed in matrix notation such that

$$\hat{C} = \begin{bmatrix} C_1(x, y_1) & \cdots & C_1(x, y_R) \\ \vdots & & \vdots \\ C_k(x, y_1) & \cdots & C_k(x, y_R) \end{bmatrix}, \ \vec{\rho} = \begin{bmatrix} \rho(x, y_1) \\ \vdots \\ \rho(x, y_R) \end{bmatrix} \qquad (17)$$

and Equation 16 can thus be rewritten for all coils as [62]

$$\vec{I} = \hat{C}\vec{\rho} \qquad (18)$$

Therefore, a generalised matrix inversion can be used to obtain the unaliased image pixels $\vec{\rho}$, where [62]

$$\vec{\rho} = (\hat{C}^H \hat{C})^{-1} \hat{C}^H \vec{I} = \hat{C}^\dagger \vec{I} \qquad (19)$$

with † denoting the Moore-Penrose pseudoinverse. A graphical outline of the algorithm is shown in Figure 9.
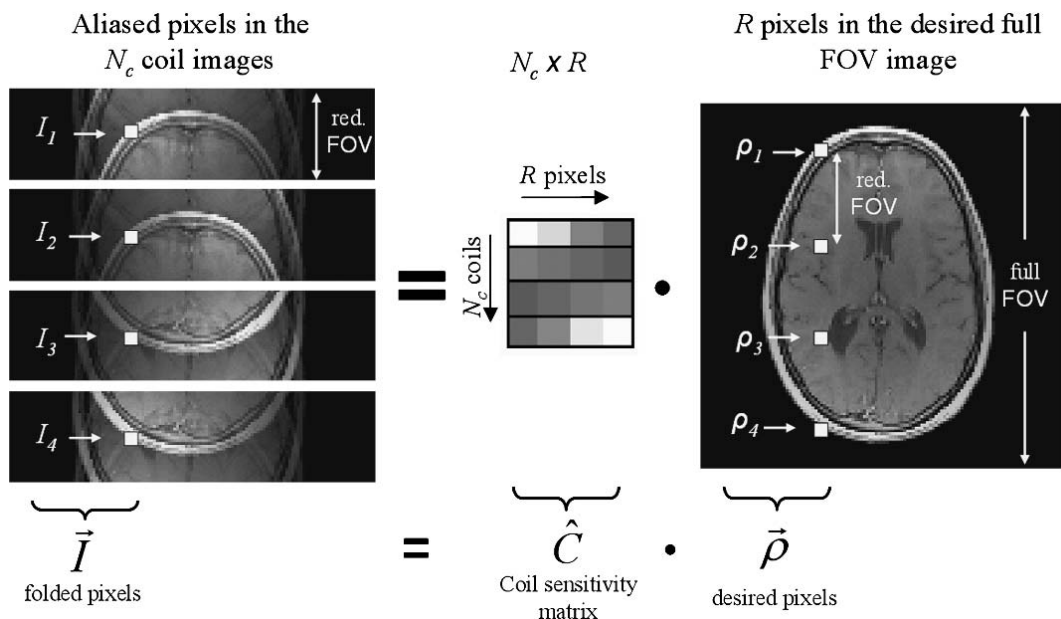
Figure 9: SENSE algorithm: The unaliased image can be obtained by inverting the signal equation (from [62], reprinted with permission of Wolters Kluwer Health, Inc. Copyright 2004 Wolters Kluwer Health, Inc.)

2.3.2 SPIRiT

SPIRiT [65] is an advanced parallel imaging algorithm that solves the parallel imaging reconstruction problem as a constrained optimisation problem in k-space. It does not require the explicit knowledge of the coil sensitivities, but exploits the complementary information from multiple coils directly in k-space. To do so, linear weights between a point in k-space and its neighbourhood (across all coils) are derived from a fully sampled k-space measurement in a process called autocalibration (see also [66, 67]). When defining the (unknown) fully sampled Cartesian k-space from all coils as a vector x, and the sampled k-space data from all coils as a vector y, the linear weights can be arranged in a matrix G so that when multiplied with x, each k-space point is recalculated as the linear weighted sum of its neighbourhood. Furthermore, if D is a matrix performing the transformation of x from fully sampled Cartesian space to the measured k-space (for example a transformation from fully sampled Cartesian space to undersampled non-Cartesian space), the constrained optimisation problem can be written as [65]

$$\arg\min_{x} \; \|Dx - y\|^2 + \lambda\|(G - I)x\|^2 \tag{20}$$

where I is the identity matrix of appropriate size and λ is a weighting parameter to balance the two terms. The first term enforces consistency to the measured k-space data y and the second term enforces consistency regarding the linear dependency of the k-space samples.
This approach allows for great flexibility, and can reconstruct Cartesian as well as non-Cartesian k-space data by properly choosing D. Furthermore, additional constraints (such as regularisation terms) can easily be added to Equation 20.

2.4 Image Quality Properties

2.4.1 Signal-to-Noise Ratio

The signal-to-noise ratio (SNR) is defined as the ratio of the mean signal over the standard deviation of the background noise, where

$$\text{SNR} = \frac{\text{mean(signal)}}{\text{std(noise)}} \tag{21}$$

(a) High SNR (peak value 100) (b) Low SNR (peak value 10)
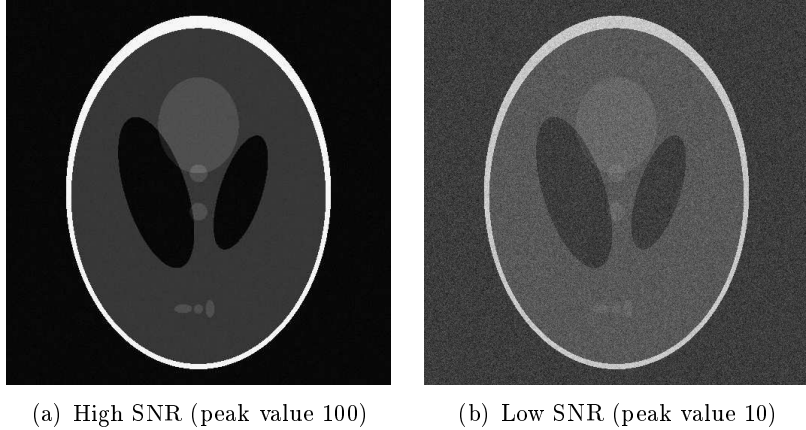
Figure 10: SNR comparison for a simulated Shepp-Logan phantom [68]. Lower SNR means that the image information is degraded

For MRI images, the noise data is either taken from multiple acquisitions or image regions with no signal. It is preferable to use complex data as input for the noise estimation, otherwise, the Rician distribution of the absolute-valued data must be taken into account [69].

For parallel imaging reconstructions, a spatially varying noise amplification based on the orthogonality of the coil sensitivity profiles occurs which can be described by the so-called geometry-factor (g-factor) [64]

$$\text{SNR}_{\text{pi}} = \frac{\text{SNR}}{g\sqrt{R}} \tag{22}$$

where SNR_{pi} is the SNR for the parallel imaging reconstruction, SNR here represents the SNR for a fully sampled dataset, g is the spatially dependent g-factor and R is the acceleration/undersampling factor.

Physically, the SNR of an acquisition of a thermally polarised sample is related to several key parameters of the NMR experiment [70]

$$\text{SNR} \ \propto \ \frac{\Delta V \sqrt{\tau} \omega_0 M_0}{\sqrt{4 k_B T R}} \tag{23}$$

where ΔV is the voxel volume, τ is the total acquisition time, ω_0 is the Larmor frequency of the investigated spin species, M_0 is the magnetisation, k_B is the Boltzmann constant, T is the temperature and R is the effective resistance of the coil loaded by the body. Here, the denominator describes the thermally induced electronic noise.

From electrodynamics, it can be derived that the voltage induced in the receiver coil by a precessing magnetisation is proportional to $\omega_0 M_0$. For thermally polarised samples, $M_0 \propto \omega_0$, and thus the signal is proportional to ω_0^2. Furthermore, as combined coil and electronics resistances have a dependence of $\sqrt{\omega_0}$, but the sample resistance is proportional to ω_0^2, the overall dependence of the SNR on the magnetic field strength is determined by the acquisition regime. At low field strengths, the SNR is approximately

proportional to $B_0^{\frac{7}{4}}$, whereas at high field strengths only a linear increase with field strength is observed. This can be expressed using a constant a, which describes the balance between coil/electronics noise and sample noise such that

$$\text{SNR} \propto \frac{\omega_0^2}{\sqrt{\omega_0^2 + a\sqrt{\omega_0}}} \tag{24}$$

For hyperpolarised samples, this relation reduces by a factor of ω_0, as the magnetisation is fixed by the polarisation level and does not depend on the magnetic field strength.

2.4.2 Signal-to-Noise Ratio for Hyperpolarised Acquisitions

Unlike for thermal MRI, the magnetisation of a hyperpolarised acquisition is non-renewable and decays rapidly because of T_1 relaxation and RF excitation. Therefore, the maximum achievable SNR is limited by the initial polarisation P_0 and the time window of the acquisition. After rotating the hyperpolarised magnetisation by a flip angle θ, the transverse magnetisation is proportional to $\sin(\theta)$, whereas the remaining longitudinal magnetisation is proportional to $\cos(\theta)$. Furthermore, when the measurements are executed with a repetition time T_R, the hyperpolarised longitudinal magnetisation decays by a factor of $e^{(\frac{-T_R}{T_1})}$ between two excitations. From these considerations, the transverse magnetisation M_n after n excitations with flip angles θ_j (neglecting thermal polarisation buildup) can be derived.

$$M_n = P_0 \prod_{j=1}^{n-1} \left[e^{(\frac{-T_R}{T_1})} \cos(\theta_j) \right] \sin(\theta_n) \tag{25}$$

This expression is valid for a hyperpolarised compound with a constant relaxation rate and a constant number of spins, however, more complicated models are required for in vivo measurements to account for effects such as perfusion, cellular uptake, and metabolic conversion (see Chapter 4).

The total signal of a hyperpolarised acquisition can be estimated by the sum of Equation 25 over all excitations. Through signal averaging, noise increases by a factor of $\sqrt{N}$. Then, the total SNR is described by

$$\text{SNR}_{\text{sum}} \propto \frac{P_0}{\sqrt{N}} \sum_{n=1}^{N} \left[\prod_{j=1}^{n-1} e^{(\frac{-T_R}{T_1})} \cos(\theta_j) \right] \sin(\theta_n) \tag{26}$$

Using Equation 26, solutions for a variable flip angle scheme that maximise the sum of all signals can be found, or those that yield a constant signal amplitude for each excitation [71]. However, usually, a constant flip angle is used to make the data evaluation easier. An exemplary SNR map for a constant flip angle, $T_R = 250$ ms, and $T_1 = 15$ s is shown below in Figure 11
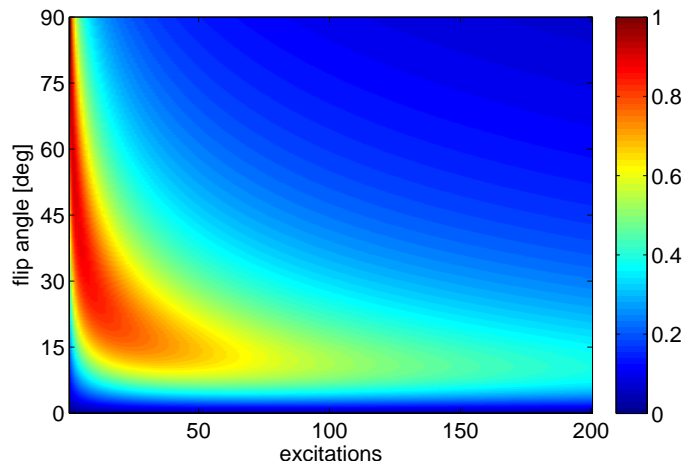
Figure 11: SNR distribution for a hyperpolarised NMR signal, constant flip angle, $T_1 = 15$ s, and $T_R = 250$ ms

As shown in Figure 11, it is important to choose the appropriate imaging parameters in order to maximise SNR.

2.4.3 Point Spread Function

The point spread function (PSF) represents the response of an imaging system to a point-shaped signal source. It describes how an ideal object is reproduced by the system, and characterises its spatial resolution. Therefore, the PSF is another very important parameter as regards image-quality assessment. In MRI, the PSF incoroporates all effects present in the image formation, from signal acquisition to postprocessing.

Assuming linearity and shift invariance, the image formation can be mathematically described by a convolution of the ideal object with the PSF

$$I(\mathbf{r}) = (\rho * F_{PSF})(\mathbf{r}) = \int \rho(\mathbf{r}') \, F_{PSF}(\mathbf{r} - \mathbf{r}') \, \mathrm{d}\mathbf{r}' \tag{27}$$

where I is the image, ρ is the ideal object, and F_{PSF} is the point spread function.

The k-space sampling pattern has a major impact on the PSF shape. A finite k-space sampling pattern corresponds to a multiplication of the data with a window function. Therefore, according to the Fourier convolution theorem, the image is convoluted with the Fourier transform of this window function. For Cartesian sampling patterns, the window function is usually a rectangular function, whose Fourier transform is a sinc function ($sinc = \frac{\sin(x)}{x}$) [72]. Thus, the image is convoluted with a sinc-shaped function. For disc-shaped sampling patterns such as spirals, it can be derived that the PSF is jinc-shaped, as the Fourier transform of a disc is the jinc function ($\frac{J_1(x)}{x}$, where J_1 is the Bessel-function of the first kind) [72].

20

disc-shaped sampling pattern   box-shaped sampling pattern

$\xi \approx 1.40$
isotropic
jinc-shaped

$\xi \approx 1.22$
anisotropic
sinc-shaped
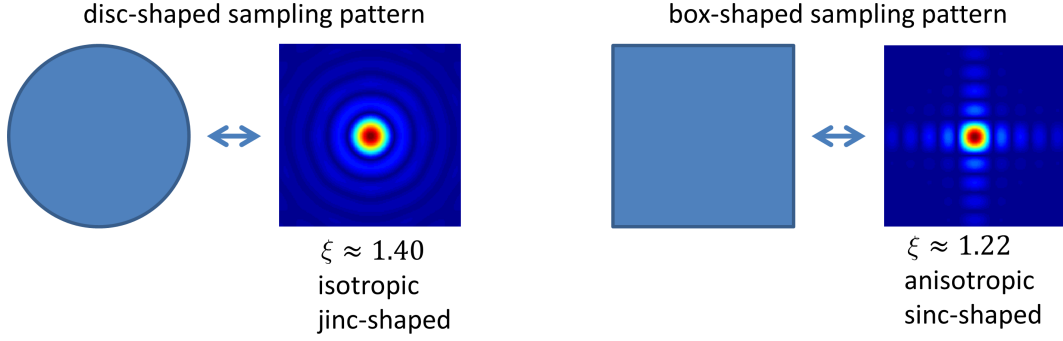
Figure 12: Illustration of the PSF shape depending on the Fourier transform of the corresponding k-space sampling pattern.

The real physical resolution can be described by the full width at half-maximum (FWHM) of the main lobe. It can be related to the field of view FOV and the nominal resolution in pixels n_{pix} such that

$$\phi = \xi \frac{\text{FOV}}{n_{pix}} \tag{28}$$

where ξ is a factor resulting from the shape of the PSF. Neglecting T_2^* decay, for a rectangular sampling scheme, $\xi \approx 1.22$. For a circular sampling pattern, $\xi \approx 1.40$.

Another important effect regarding the PSF is the T_2^* decay along the readout, which behaves like an additional window function. Moreover, off-resonance artefacts can lead to blurring for non-Cartesian trajectories because of a phase accrual along the readout. In sequence design and reconstruction, the goal is to obtain a satisfactory trade-off between the SNR and the PSF. For reconstruction, this can be balanced through the use of different estimators and filters.

2.5 Non-Cartesian k-space Sampling

Non-Cartesian k-space sampling strategies, for example, those involving spiral [73, 74] or radial trajectories [1, 75, 76], have certain advantages compared to Cartesian sampling schemes. They allow a more efficient sampling of k-space and produce incoherent undersampling artefacts. Moreover, if the k-space centre is oversampled, as it is the case for radial and spiral sampling patterns, the pulse sequence is more robust against motion. On the other hand, non-Cartesian acquisitions are more prone to artefacts due to gradient errors and B_0 inhomogeneity.
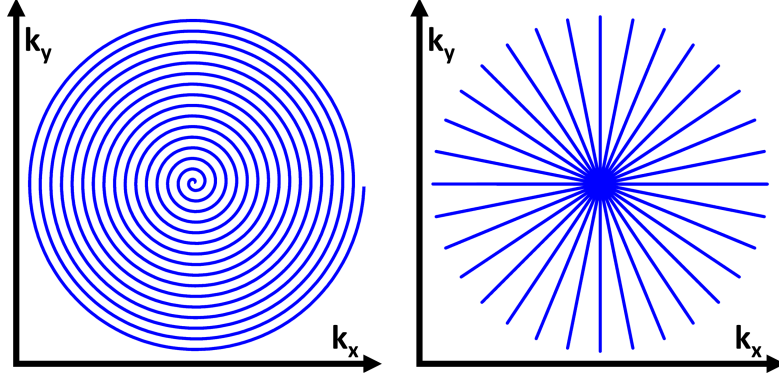
Figure 13: Exemplary non-Cartesian k-space trajectories. Left: spiral trajectory, right: radial trajectory.

2.5.1 Reconstruction

For Cartesian data, a simple fast Fourier transform (FFT) is sufficient for image reconstruction, however, non-Cartesian data require a more complicated reconstruction. The backtransform from arbitrary k-space to Cartesian image space for a 2D acquisition of a single resonance (compare [77]) is given by

$$\rho(\mathbf{r}) = \int s(\mathbf{k}(\mathbf{u}))e^{-i2\pi\mathbf{k}(\mathbf{u})\mathbf{r}} \left| \frac{\partial \mathbf{k}(\mathbf{u})}{\partial \mathbf{u}} \right| d^3u \tag{29}$$

where $\mathbf{k} = T(\mathbf{u})$ is a differentiable coordinate transformation from k-space to a uniform space $\mathbf{u}$, for example, polar coordinates for spirals. Due to this coordinate transformation, the absolute value of the determinant of the Jacobian matrix is required in Equation 29, so as to account for the nonuniform infinitesimal area element in the non-Cartesian k-space coordinate system. For most continuous trajectories, the Jacobian determinant can be calculated analytically, for example for spirals [77] (assuming radial symmetry and monotonicity) the so-called "density compensation" is given by

$$w(t) = |\mathbf{k}(t)| \left| \frac{d\mathbf{k}(t)}{dt} \right| \left| cos(\mathbf{k}(t), \frac{d\mathbf{k}(t)}{dt}) \right| \tag{30}$$

For discrete trajectories consisting of sampling points $\mathbf{k}_j$, an accurate appromixation is then according to [77] given by Equation 31.

$$w_j = \begin{cases} 0, & j = 1 \\ |\mathbf{k}_j| \cdot ||\mathbf{k}_j| - |\mathbf{k}_{j-1}||, & j > 1 \end{cases} \tag{31}$$

To reduce the computational cost of the reconstruction process, Equation 29 is usually approximated using a method called gridding [78, 79]. The non-Cartesian data s are first interpolated onto a Cartesian grid using a convolution operation with a compactly supported kernel $g(k_x, k_y)$, such that

$$s_c(m\Delta k_x, n\Delta k_y) = \sum_j s(k_{x,j}, k_{y,j})g(m\Delta k_x - k_{x,j}, n\Delta k_y - k_{y,j})w_j \tag{32}$$

where $s_c(m\Delta k_x, n\Delta k_y)$ is the interpolated data on a Cartesian grid with spacing Δk_x and Δk_x, m and n are integer values determining the coordinates and $k_{x,j}$ and $k_{y,j}$ are the discrete (non-Cartesian) k-space sampling points. Subsequently, a standard FFT can be applied to perform the transformation to image space.

2.5.2 Noise Amplification

Non-equidistant k-space sampling results in a certain amount of noise aplification due to uneven weighting of the data points in the reconstruction.

Figure 14: 1D nonuniform sampling. Decreasing the sampling density along the readout results in increased density weights in a gridding reconstruction, leading to noise amplification.

Assuming non-correlated k-space measurements, the variance of the discretised linear transformation can be calculated from Equation 29 in a straight-forward manner [80], yielding

$$\sigma^2_{\text{image}} = \frac{\sigma^2_{\text{k-space}}M}{\tau}\frac{\sum_j w_j^2}{(\sum_j w_j)^2} \tag{33}$$

where σ^2_{image} is the variance of a single image point, w_j is the discretised Jacobian determinant, M is the number of sampled points, $\sigma^2_{\text{k-space}}$ is the variance of a single k-space point and τ is the total sampling time. The SNR efficiency regarding noise amplification from the k-space sampling pattern (SNR gradient encoding efficiency) can then be defined as

$$\epsilon = \sqrt{\frac{(\sum_j w_j)^2}{M \sum_j w_j^2}} \tag{34}$$

The summation in the nominator corresponds to the entire k-space area covered, thus, the maximum SNR (without additional filtering) can be achieved via a Cartesian sampling scheme, because a fixed value of w_j minimises the denominator. For a detailed treatment of this matter, see [80].

2.6 Gadolinium-based MRI Contrast Agents

MRI contrast agents can shorten the relaxation times of nuclear spins. If administered before or during an MRI exam, this allows to increase the anatomical contrast and to obtain physiological information. Most commonly, gadolinium-based contrast agents are used as gadolinium(III) ions are strongly paramagnetic, having seven unpaired electrons in their 4f shells. Thermally driven motion of the gadolinium ions then generates oscillating magnetic fields, which provide efficient T_1 relaxation if the frequency of the fluctuations is near the Larmor frequency of the target spins. As free gadolinium ions are toxic, they must be coordinated by a strongly binding ligand. In commercially available contrast agents, eight of the nine coordination sites of the Gd(III) ion are occupied by the ligand, while one is available for short-term bonding with a water molecule, providing efficient relaxation via dipolar interaction, i.e. the so-called "inner-sphere" relaxation. Moreover, an "outer-sphere" relaxation is possible for water molecules diffusing in the outer coordination sphere of the complex. Although not as powerful as inner-sphere relaxation for a single molecule, a larger number of water molecules is reached along the surface of the complex. At clinical field strengths, both mechanisms are believed to be of roughly equal magnitude. The most commonly used gadolinium-based contrast agents are depicted in Figure 15. For a more detailed discussion of this topic, please see [81] and [82].
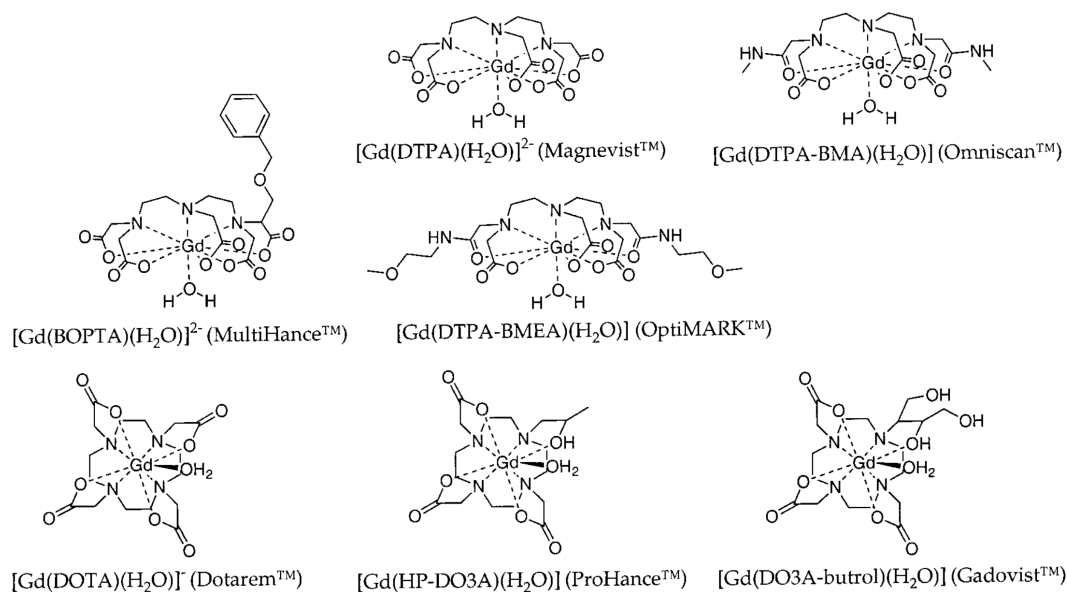
Figure 15: 2D chemical structures of commonly used gadolinium-based MRI contrast agents (Reprinted with permission from [82]. Copyright 1999 American Chemical Society.)

2.7 Dynamic Nuclear Polarisation

As thermal polarisation is not sufficient for conducting in vivo measurements with endogeneous biomarkers, hyperpolarisation methods must be employed to increase the polarisation. Examining the Boltzmann-statistics in Equation 7, it is evident that the spin

population depends not only on the static magnetic field, but also on the gyromagnetic ratio γ and the temperature. The polarisation will increase with higher γ and lower temperature. While ^{1}H or ^{13}C nuclei show only a low polarisation at 1 K and 3.35 T, electrons are highly polarised as a result of their higher gyromagnetic ratio (see Figure 16) which is 660 times larger than that for ^{1}H and 2600 times larger than that for ^{13}C. This property is exploited by a technique called dynamic nuclear polarisation [5] to increase the NMR signal by a factor of several 10.000. First, the isotopically labelled sample is homogeneously mixed with a free radical that provides a high concentration of unpaired electrons. Then, the sample is cooled down to $\approx$ 1 K and the electron polarisation is transferred to the target nucleus via continuous microwave irradiation close to the electron spin resonance frequency (approximately 94 GHz at 3.35 T). There are multiple effects driving this transfer, such as the solid-effect, thermal mixing or the cross-effect, which are too complex to present in this brief overview. For an extensive description of currently available hyperpolarisation methods, please see for example [83]. After a sufficient polarisation level has been reached, the sample is rapidly dissolved under pressure with a preheated solvent to obtain a hyperpolarised solution at room temperature. To obtain a physiological solution, a pH buffer and additional salt can be added to the dissolution agent. After the dissolution process, the hyperpolarised magnetisation decays towards the thermal equilibrium state as a result of spin-lattice relaxation and RF excitations. Currently, the technique is being translated to clinical applications and recently, the first trials in human patients were initiated [42].
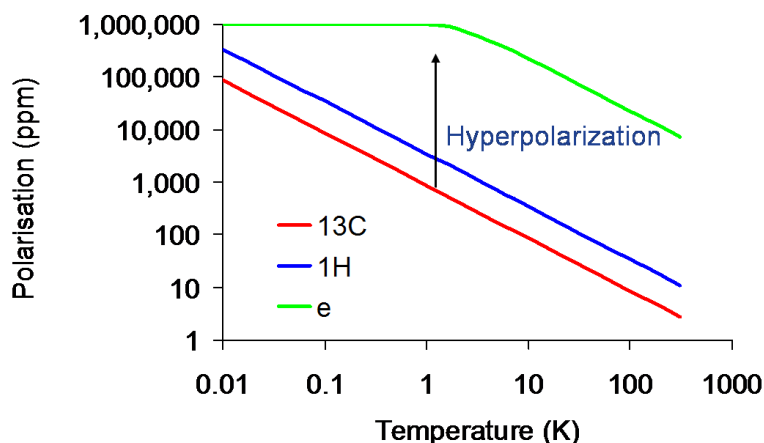
Figure 16: Polarisation of ^{1}H nuclei, ^{13}C nuclei and electrons at 3.35 T (from [84], with permission of the author).

2.8 ^{13}C Biomarkers for DNP Hyperpolarisation

The carbon isotope ^{13}C has some unique properties that render it especially suitable for hyperpolarised in vivo studies. Firstly, the low natural abundance of ^{13}C ($\approx$ 1.1% [44]) means that there is virtually no background signal in a living organism. Furthermore,

most endogenous molecules include carbon which allows interesting metabolic pathways to be studied. However, other nuclei such as ^{15}N are also currently being explored. The general requirements for a molecule to be used as a hyperpolarised biomarker are that the T_1 relaxation time of its hyperpolarised nucleus is sufficiently long for measurement and that sufficient polarisation levels can be reached, further, the uptake and/or the metabolism must be sufficiently fast to be observed before the signal has decayed. In general, the T_1 is longer for small molecules, as their motion is too fast for efficient spin-lattice relaxation. In addition, the target nucleus should not have any directly attached protons because the strong dipolar coupling considerably increases the T_1 relaxation.

2.8.1 [1-^{13}C]Pyruvate

One of the most widely used molecules for in vivo hyperpolarisation studies is [1-^{13}C]-pyruvate. This molecule exhibits high polarisation levels after dissolution (approximately 25 %) and its T_1 relaxation time is sufficiently long enough to measure its metabolisation ($\approx$ 20 s in vivo at 3 T). Pyruvate is an endogeneous molecule that can be injected in fairly high doses and is an important part of the energy metabolism of cells.

After it has been taken up by the cells, pyruvate can be converted enzymatically to lactate, which is catalysed by lactate dehydrogenase (LDH), and to alanine which is catalysed by alanine transaminase (ALT). These reactions occur in the cytosol. Furthermore, pyruvate can enter the mitochondria where decarboxylation to carbon dioxide, which is catalysed by pyruvate dehydrogenase (PDH), is possible. The generated carbon dioxide is in rapid exchange with bicarbonate via a reaction catalysed by carbonic anhydrase.

Typical time curves for hyperpolarised pyruvate and lactate in a rat tumour voxel are shown in Figure 18. After the injection, a pyruvate bolus can be observed, which is accompanied by the generation of lactate. The curves decay over time because of T_1 relaxation and RF excitation.
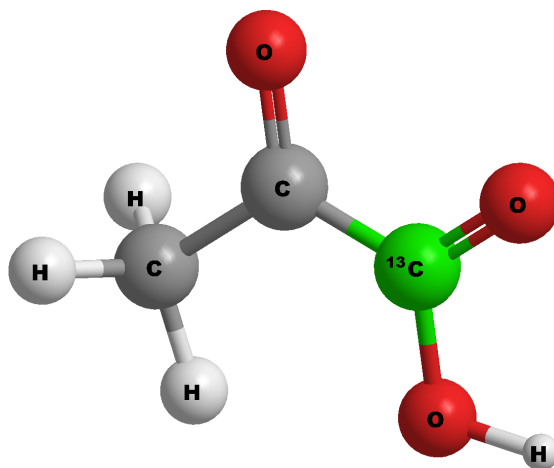
Figure 17: [1-^{13}C]Pyruvic acid structure in 3D
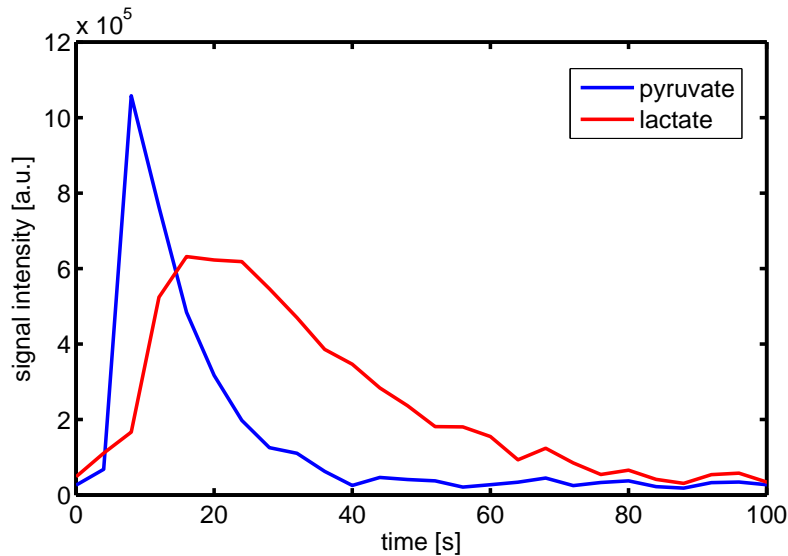
Figure 18: ^{13}C pyruvate metabolism from a rat tumour region of interest (ROI) (in vivo), after injection of 1ml of 80 mM hyperpolarised pyruvate solution, measured with an IDEAL Spiral CSI sequence [19]

Pyruvate Metabolism in Cancer Cells

Normal cells primarily generate energy in the form of adenosine triphosphate (ATP) in their mitochondria by transforming nutrients such as glucose in a process called oxidative phosphorylation. The metabolism of glucose produces pyruvate, which is then used in the tricarboxylic acid (TCA) cycle to generate ATP in an aerobic (oxygen-consuming) reaction. When insufficient oxygen is available, pyruvate is instead fermented to lactate in an anaerobic process in order to form ATP. Cancer cells, however, always have a high rate of lactate production, even in the presence of oxygen. This phenomenon of aerobic glycolysis in cancerous tissue is also known as the Warburg effect [85] [86]. Since its discovery, this effect has stimulated considerable research interest, and it is the reason why pyruvate is one of the most widely used compounds for hyperpolarised in vivo studies. Tumour metabolism [9, 87, 88] as well as response to treatment [7, 89, 90] have been investigated in a large number of studies using hyperpolarised pyruvate.

Cardiac Pyruvate Metabolism

Another promising application of hyperpolarised pyruvate is to assess cardiac metabolism. Several studies have reported the detection of hyperpolarised pyruvate metabolism in cardiac muscle cells, both in vitro [91] and in vivo [41, 92–95]. Following an ischemic event, significant changes in hyperpolarised pyruvate metabolism was found [41, 92]. In addition to the formation of lactate and alanine, which reflects the general metabolic activity of the cell, bicarbonate formation is of particular interest in this case. When pyruvate is converted to carbon dioxide by PDH, it quickly reaches an equilibrium state with bicarbonate because of the physiological pH buffering system. As a result, the bicarbonate formation reflects the mitochondrial activity of cells. Therefore, the viability

of myocardial cells can be assessed using hyperpolarised pyruvate.

2.8.2 [^{13}C]Urea

The urea molecule is the end product of nitrogen metabolism in mammals, and is usually excreted in the urine. Since it is metabolically inactive and can be injected in high concentrations because of its low toxicity, it is suitable for use as a hyperpolarised perfusion marker. Compared to proton perfusion measurements with gadolinium-based relaxation agents, it offers a virtually background-free signal, however, relaxation and cellular uptake must be considered. [^{13}C]Urea provides sufficient polarisation and T_1 times for in vivo application [96, 97]. Furthermore, ^{13}C-labelled urea can be copolarised with other ^{13}C biomarkers such as [1-^{13}C]pyruvate to yield information on metabolism and perfusion simultaneously. In order to avoid quadrupolar relaxation processes, which can rapidly kill the hyperpolarised signal in an environment with low magnetic field (for example, during transport to the NMR scanner), [^{13}C, ^{15}N$_2$]urea can be used [98].
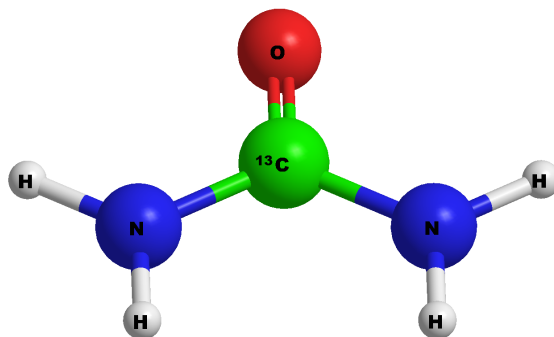
Figure 19: [^{13}C]Urea structure in 3D

2.9 ^{15}N Biomarkers for DNP Hyperpolarisation

Although most DNP studies focus on ^{13}C-labelled compounds, also other nuclei are currently explored. A very promising candidate for in vivo applications is ^{15}N, because nitrogen occurs in many endogenous molecules. Besides the low natural abundance of ^{15}N (≈ 0.37 %), the main advantage of this isotope is its low gyromagnetic ratio of only -4.316 $\frac{MHz}{T}$ [58] (about 40% of ^{13}C, about 10% of ^{1}H). This reduces the interaction with external magnetic fields compared to nuclei with higher γ and allows for very long T_1 relaxation times compared to ^{13}C-based molecules. However, the lower γ also results in decreased NMR sensitivity.

2.9.1 α-Trideuteromethyl[^{15}N]glutamine

α-Trideuteromethyl[^{15}N]glutamine [28] is a ^{15}N-labelled, permethylated, and perdeuterated glutamine molecule. By replacing the protons in the direct neighbourhood of the ^{15}N label with deuterated methyl groups, the dipolar contribution to the longitudinal relaxation can be reduced significantly, resulting in extraordinarily long T_1 relaxation

times (approximately 200 s at 14.1 T [28]). As a result of this modification, the molecule is no longer metabolised [99]. However, it can be used as a long-lived marker of perfusion and transport. For more information, please see Chapter 6 and Reference [28].
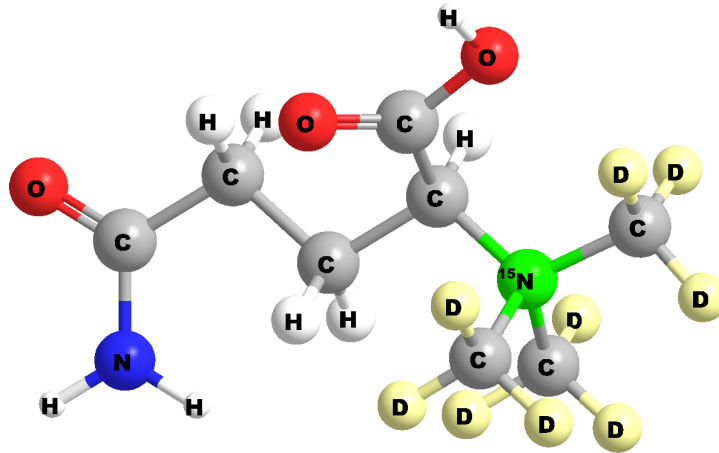
Figure 20: α-Trideuteromethyl[^{15}N]glutamine structure in 3D (compare [28]).

3 Comparison of Acquisition Schemes for Hyperpolarised ^{13}C Imaging

This chapter is an amended version of [100].

3.1 Introduction

While the DNP technique is currently being translated to clinical applications [42], the evaluation and optimisation of different imaging sequences still constitutes a highly active field of research [13, 101]. In the past few years, many different approaches have been reported, most having been adapted from ^{1}H MRSI sequences, such as free induction decay chemical shift imaging (FIDCSI) [7–12], echo-planar spectroscopic imaging (EPSI) [13–17], spiral chemical shift imaging (SPCSI) [22–27], strategies based on multi-echo chemical shift species separation (e.g. IDEAL spiral chemical shift imaging (ISPCSI) [18–21]), spin-echo [15, 102] and steady-state free precession (SSFP) [96, 97, 103, 104] methods. As a result of this variety, a complete and comprehensive overview is not practical. Instead, an in-depth comparison of exemplary sequence types is presented in order to derive general conclusions on hyperpolarised imaging strategies.

Currently, the sequences that are used most often rely on a simple pulse-and-acquire scheme in which a slice-selective pulse is combined with a specific gradient readout to encode the spectral and spatial dimensions. Such approaches can be split into two general types. The static acquisition schemes focus on encoding only one or a few images within the time window provided by the hyperpolarised agent, and therefore have low encoding efficiency requirements. There are also dynamic approaches, which aim at encoding the time curve of a hyperpolarised substrate and its metabolites in real-time in order to be able to quantify the enzymatic reaction. To do so, a high encoding efficiency is required to achieve a high temporal resolution.

The selection of sequences for the comparison was based on several criteria. First, the sequence needs to be well established and tested in the literature, showing certain potential for use in clinical studies and also allowing to use the most optimised choice of parameters. Furthermore, the sequence needs to be widely used, judging by the number of reported studies, in order to be of relevance to the majority of readers. Last, a great variety of acquisition speeds and gradient encoding patterns should be included, so that many possible applications are covered.

Four exemplary sequence types were chosen for the comparison: FIDCSI [7–12], EPSI [13–17], ISPCSI [18–21] and SPCSI [22–27]. An extensive theoretical treatment is provided, together with simulations, to characterise the behaviour of the sequences and illustrate their potential advantages and disadvantages. The goals of this work are to facilitate the selection of optimal imaging parameters for a specific purpose and to provide a basis for the identification of potential candidates for clinical applications.

3.2 Theory

3.2.1 Pulse Sequence Dependent Properties of Hyperpolarised Acquisitions

Signal-to-Noise Ratio

The SNR of a hyperpolarised acquisition is influenced by several sequence-related parameters. For static acquisitions, the starting time of the scan is crucial. To maximise metabolite SNR and minimise artefacts caused by rapid signal change, the expected range of the conversion rate constants can be used to calculate the optimal starting point (see Chapter 4). A real-time bolus-tracking approach can help to overcome problems with varying levels of perfusion [105]. Dynamic acquisitions can be started at the beginning of the injection if the bolus characteristics are of interest.

The SNR of hyperpolarised acquisitions does not depend solely on the total readout time, but the maximum obtainable SNR is dependent on the initial polarisation level and the time window of the acquisition (see Section 2.4.2). The optimal repetition time and flip angle in order to obtain the maximum SNR of the metabolite or to extract the conversion rate constant can be calculated by considering the expected ranges of the metabolic conversion and relaxation processes [105, 106].

When creating a gradient readout, certain design principles need to be obeyed in order to maximise SNR. Many trajectories need pre/rewinders to move to a certain point in k-space. Usually, those parts are discarded for reconstruction, which means that the SNR compared to a full readout is reduced. As the SNR is proportional to the square root of the readout time (see Section 2.4.1), the SNR loss is proportional to the square root of the fraction of the used parts to the full readout (decay processes can be neglected if the discarded parts are short and repeated frequently during readout). This parameter will be called gradient readout efficiency in the following.
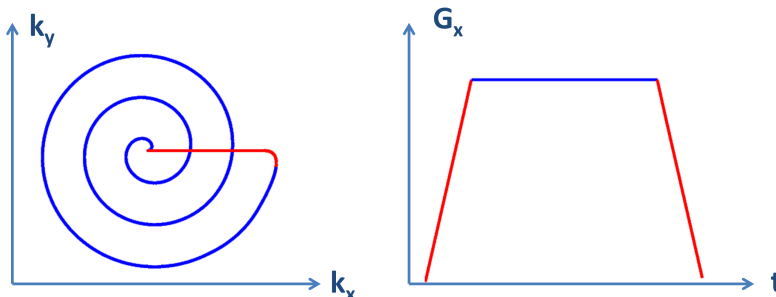
Figure 21: Illustration of gradient readout efficiency for spiral trajectory and trapezoidal gradient shape. Rewinder and ramps are usually discarded in the reconstruction, resulting in SNR penalty.

Another important factor when designing the spatial readout is the SNR gradient encoding efficiency, which is determined by the uniformity of the trajectory. A non-uniform k-space density leads to an SNR penalty as a result of noise amplification in the reconstruction process [80, 107] (see Section 2.5.2). For trapezoidal gradient shapes (as

used for EPSI), this applies to the ramp part of the gradient lobes, whereas, for spiral trajectories, gradient slew rate constraints can cause a non-uniform k-space sampling density at the beginning of the trajectory. The SNR gradient encoding efficiency can be defined mathematically as:

$$\epsilon = \sqrt{\frac{(\sum_j w_j)^2}{M \sum_j w_j^2}} \tag{35}$$

where w is the density compensation of the trajectory and M is the number of trajectory points.

Spectral Bandwidth
Acquisition schemes that encode the chemical shift information by resampling the same k-space point during the gradient read-out at a certain spectral bandwidth require sufficient magnetic field gradients. If the gradient system is strong enough, the waveform can be designed for a spectral bandwidth that includes all (excited) compounds. Often, this will not be the case and a smaller spectral bandwidth (longer sampling interval) is chosen, which means that spectral peaks outside of the spectral bandwidth will fold into the spectrum (see Section 2.2.2). In this case, it is important to choose a suitable aliasing pattern so that the peaks of interest can still be separated. As magnetic field inhomogeneities can cause considerable broadening of the spectral peaks, sufficient spacing is required between neighbouring frequencies, especially for in vivo experiments. For pyruvate and its metabolites at 3 T, often 581 Hz are chosen so that pyruvate, lactate and alanine can be resolved whereas the bicarbonate peak folds onto the pyruvate hydrate peak as shown in Figure 22. This is the reason why 581 Hz spectral bandwidth is chosen for EPSI and SPCSI in this comparison.
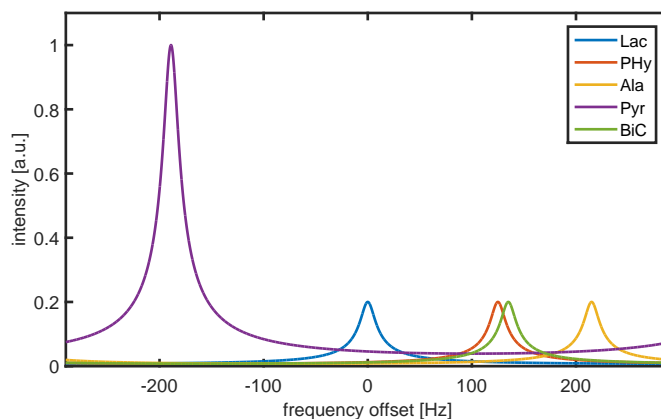
Figure 22: Spectral aliasing for pyruvate (Pyr), pyruvate hydrate (PHy), lactate (Lac), alanine (Ala) and bicarbonate (BiC) at a spectral bandwidth of 581 Hz and a magnetic field strength of 3 T.

Point Spread Function

As described in Section 2.4.3, the point spread function (PSF) of a k-space sampling scheme is mainly determined by the Fourier transform of its shape. For a rectangular sampling scheme (as used for EPSI), the PSF is sinc-shaped [72]. For a circular sampling pattern (FIDCSI, ISPCSI, SPCSI), the PSF is jinc-shaped [72]. For SPCSI and even more for ISPCSI, T_2^* decay will act as a natural apodisation and can cause significant broadening of the PSF (see [108] for a detailed theoretical treatment of this issue). Filtering can be used to improve the shape of the PSF, e.g. minimise sidelobes.

Furthermore, filtering is necessary to optimise the SNR in the presence of T_2^* decay during the long readouts; however, the SNR optimal filter depends on the properties of the measured sample. For FIDCSI, EPSI and SPCSI, the decay occurs mainly along the spectral dimension, whereas, for ISPCSI, it primarily affects the spatial k-space domain. As the T_2^* value and the signal distribution in k-space are not known exactly, assumptions must be made which affect the final SNR. In this work, a 15 Hz Gaussian filter (corresponding to $T_2^* = 20$ ms) was chosen for all acquisitions, which previous studies have shown to be a reasonable choice for the optimisation of SNR and minimisation of PSF broadening [57].

3.2.2 Sequences

FIDCSI

FIDCSI represents the gold standard for ^{1}H chemical shift imaging (CSI). It consists simply of free induction decay (FID) acquisitions with a preceding phase encoding gradient to scan k-space pointwise with multiple excitations. As a result of this inefficient encoding scheme, typically only one or a few images can be acquired before the hyperpolarised signal has decayed. A variable flip angle (VFA) scheme [71, 109] can be used to obtain equal signal intensities for each excitation in the presence of a decaying polarisation to avoid signal inconsistencies. For the same reason, the starting time needs to be chosen carefully in order to avoid the initial bolus phase. Usually, a Cartesian encoding scheme is used, so that reconstruction can be performed by taking fast Fourier transforms (FFTs) along the spectral and spatial k-space dimensions. A spatially resolved spectrum can be obtained at an arbitrary sampling rate and sampling time, which provides maximum flexibility for all kinds of chemical shift distributions. A circular sampling pattern (Figure 27) can be used to obtain isotropic resolution and to reduce the scan time.
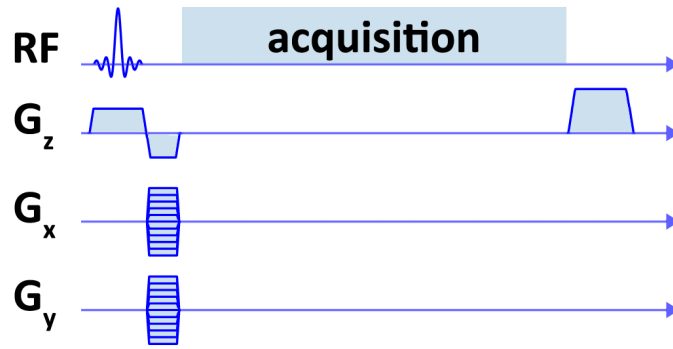
Figure 23: Pulse sequence diagram for FIDCSI, not to scale for illustration purposes (from [60]).

EPSI

EPSI samples a single line in k-space repeatedly after one radiofrequency (RF) excitation in order to acquire both spatial and spectral information simultaneously. Thus, it provides a significantly increased encoding efficiency relative to FIDCSI, so that biochemical pathways can be sampled dynamically with a time resolution of a few seconds. As the spectral bandwidth is determined by the time it takes to return to the same k-space point, in general, EPSI has a high gradient demand, and the spectral and spatial resolution are limited by the maximum available gradient amplitude and slew rate. This is even more critical for ^{13}C than for ^{1}H because of the lower gyromagnetic ratio. Usually, a flyback design (rewinder with maximum gradient slew rate/amplitude) is chosen for the trajectory (Figure 24), and only the plateau parts of the sampling lobe are used for reconstruction. This increases the gradient hardware requirements and lowers the SNR efficiency, but also reduces artefacts. If the ramp parts are included in a gridding reconstruction, the lost SNR efficiency can be partially recovered.
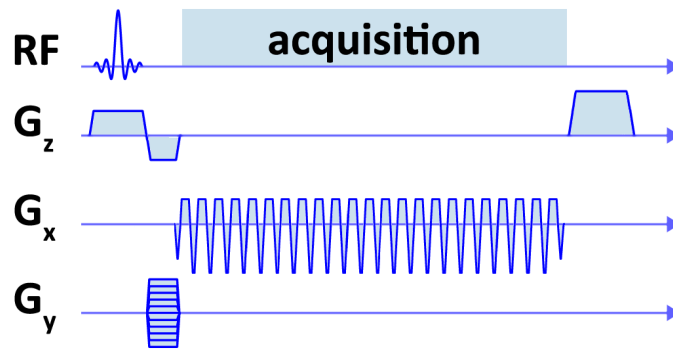
Figure 24: Pulse sequence diagram for flyback EPSI, not to scale for illustration purposes.

ISPCSI

ISPCSI uses a single-shot spiral trajectory to encode the two spatial dimensions after RF excitation. To cover the spectral domain, this trajectory is repeated in separate excitations with a specific increase in echo time tailored to the expected ^{13}C frequency shifts. The echo time shift ΔT_E must be chosen carefully in order to minimise noise amplifi-

cation [19, 110]. A least-squares algorithm (IDEAL) [110] is then used to separate the different metabolic species based on their chemical shift frequencies, which are required as prior knowledge. Usually, slice-selective FIDs are acquired alongside the images to obtain the frequency profile. IDEAL exploits the sparsity of the in vivo ^{13}C spectra, which typically do not have background signals. This ensures a high encoding efficiency as, for n metabolites, only n echoes are required. Moreover, the design constraints are low because the spatial and spectral domains are acquired independently. One of the drawbacks to this method is that no full spectrum is obtained, and the spiral trajectory is therefore vulnerable to off-resonance effects.
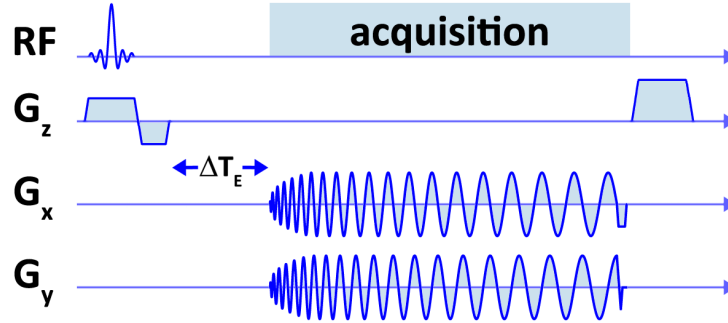
Figure 25: Pulse sequence diagram for ISPCSI, not to scale for illustration purposes (from [60]).

SPCSI
As in EPSI, spectral and spatial information are obtained simultaneously during readout in SPCSI by repeatedly scanning a spiral trajectory after RF excitation. The spectral width of this approach is thus determined by the duration of a single spiral including the rewinder. To increase the spectral width, additional excitations with a time-shifted trajectory can be acquired, or the k-space sampling can be split into multiple spiral interleaves. In principle, this approach has the highest sampling efficiency as two-dimensional spatial and spectral information can be obtained from a single excitation. However, this implies severe timing constraints for the trajectory design, resulting in a very high gradient demand. In addition, the non-Cartesian spiral trajectory is sensitive to gradient imperfections, and artefacts can occur if there are deviations along the spiral sampling train. If the spatial information is acquired in multiple spiral interleaves, signal inconsistencies can be another source of error.
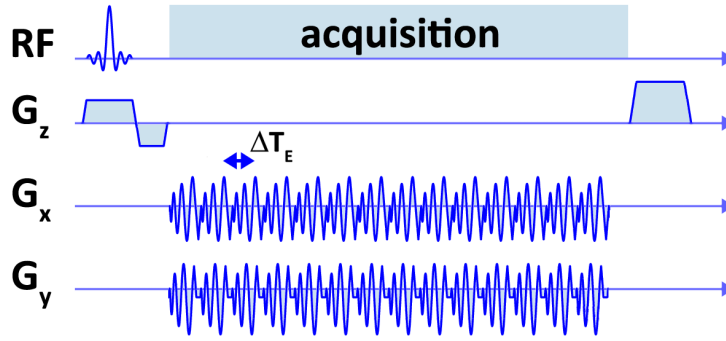
Figure 26: Pulse sequence diagram for SPCSI, not to scale for illustration purposes.

3.3 Methods

3.3.1 Sequence Design

All sequences were designed for a FOV of 8×8 cm^2, a maximum gradient amplitude of 40 mT/m and a maximum slew rate of 150 T/m/s. Two groups of sequences were created: the first consisted of FIDCSI, EPSI and SPCSI trajectories with a lower resolution of approximately 8×8 pixels, and the second of FIDCSI, EPSI and ISPCSI trajectories with a higher resolution of approximately 16×16 pixels.

FIDCSI
The FIDCSI sequence files were created by Dr. Ulrich Koellisch. Trapezoidal phase encoding gradients were created with the maximum slew rate and amplitude. k-space was sampled in centric order, starting from the inner points and going outwards; 256 points were sampled with a readout bandwidth of 5000 Hz, amounting to a total readout time of 51.2 ms and a spectral resolution of 19.5 Hz. The high-resolution sequence was created with a nominal resolution of 16×16 pixels consisting of 208 excitations, and the low-resolution sequence was created with a nominal resolution of 8×8 pixels consisting of 52 excitations. As there are no active gradients during encoding, the SNR gradient encoding efficiency was 100 %.

EPSI
For EPSI, a flyback approach was chosen because of its robustness to phase errors. A trapezoidal gradient shape using maximum gradient slew rate and amplitude was employed to rewind the phase after the actual readout lobe. The high-resolution trajectory had a nominal resolution of 16×16 pixels including ramps, and a plateau-to-ramp ratio of 43 %, resulting in an SNR readout efficiency of $\sqrt{0.43} = 66$ %. The low-resolution trajectory had a nominal resolution of 8×8 pixels including ramps, and a plateau-to-ramp ratio of 67 %, translating to an SNR readout efficiency of $\sqrt{0.67} = 82\%$. Both trajectories were designed with a spectral width of 581 Hz and consisted of 37 individual readout lobes, amounting to a total sampling time of about 64 ms. The y-axis phase encodes were created centre-out and corresponded to the nominal resolution of the x-axis

37

readout. The SNR gradient encoding efficiency was 94 % for the low-resolution trajectory and 92 % for the high-resolution trajectory; both were designed with a maximum gradient amplitude of 40 mT/m and a maximum gradient slew rate of 150 T/m/s.

ISPCSI

The ISPCSI waveform file was created by Dr. Rolf Schulte. The trajectory was created with uniform density and a nominal resolution of 32×32 pixels which, assuming a T_2^* decay of about 20 ms and a Gaussian filter of equal magnitude, translates to a real resolution of 16×16 pixels [108]. The spiral trajectory was designed using the variable density spiral generation script by Hargreaves [111]. The total readout time was 45 ms. For pyruvate and its metabolites, seven echoes with an echo time shift increase of 1.12 ms were acquired. This waiting time translates to an SNR readout efficiency of 92 % for an assumed T_2^* of 20 ms. The SNR efficiency regarding chemical shift separation with this echo time shift was calculated to have a mean value of 91 % for pyruvate, lactate and alanine with an assumed Gaussian line broadening as a result of B_0 inhomogeneity of 20 Hz. The SNR gradient encoding efficiency was 99 % with a maximum gradient amplitude of 22 mT/m and a maximum gradient slew rate of 73 T/m/s.

SPCSI

The SPCSI trajectory consisted of two spatial interleaves and one additional T_E shift, so that four excitations are necessary for one image (Fig. 1). The spiral trajectories were calculated with the variable density spiral generation script [111], and then a rewinder was calculated using trapezoidal gradient shapes. The individual interleaves were arranged into a train of 18 consecutive interleaves. A single SPCSI readout had a spectral width of 294 Hz and, with the echo time shift of 1.7 ms, a final spectral width of 581 Hz was obtained. The nominal spatial resolution was 11.4×11.4 pixels, translating to a real resolution of about 8×8 when assuming a T_2^* value of 20 ms [108]. The ratio of data collection to the rewinder was 76 %, resulting in an SNR readout efficiency of $\sqrt{0.76} = 87\%$. The SNR gradient encoding efficiency (excluding the rewinder) was 95 % with a maximum gradient amplitude of 40 mT/m and a maximum gradient slew rate of 150 T/m/s.

The spatial k-space trajectories of the designed pulse sequences are shown in Figure 27; the respective theoretical performance parameters can be found in Table 3.
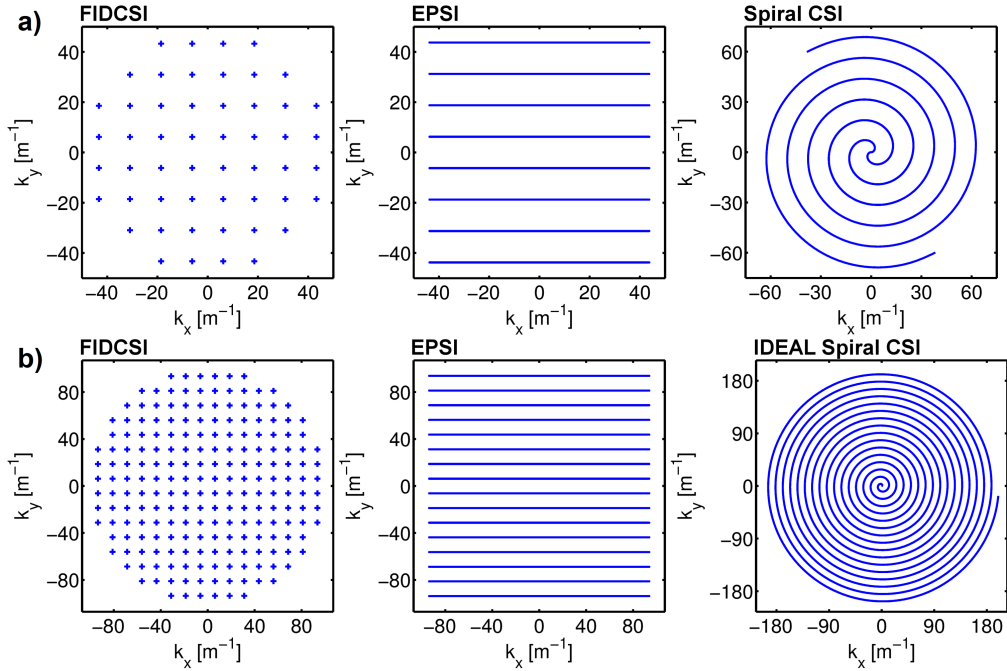
Figure 27: Two-dimensional spatial k-space trajectories of the investigated sequences for the lower (a) and higher (b) resolution.

sequence	number of excitations	total acquisition time [ms]	SNR gradient encoding efficiency [%]	SNR readout efficiency [%]	SNR chemical shift separation efficiency [%]
FIDCSI 8×8	52	2662	100	100	100
EPSI 8×8	8	512	100	82	100
EPSI full 8×8	8	512	94	100	100
SPCSI 8×8	4	245	95	87	100
FIDCSI 16×16	208	10650	100	100	100
EPSI 16×16	16	1024	100	66	100
EPSI full 16×16	16	1024	92	100	100
ISPCSI 16×16	7	315	99	92	91

Table 3: Theoretical performance parameters of the investigated sequences. "SNR gradient encoding efficiency" denotes the SNR efficiency regarding noise amplification from non-equidistant k-space sampling, "SNR readout efficiency" denotes the SNR efficiency regarding discarded data, "SNR chemical shift separation efficiency" denotes the SNR efficiency regarding the separation of signals originating from metabolites with different chemical shifts. "EPSI full" is the EPSI reconstruction including ramps and rewinders.

3.3.2 Simulations

An extensive simulation framework was created using MATLAB (MathWorks, Inc., Natick, MA, USA) to compare the performances of the four sequence types. A phantom consisting of multiple circular areas with lactate, pyruvate hydrate, alanine and pyruvate (0, -125, -215 and -392 Hz at 3 T, equal concentrations) was simulated using the forward signal encoding matrix with the respective parameters. Subsequently, Gaussian noise was added to the simulated signal. After reconstruction, a region of interest (ROI) in the lactate map was used in order to quantify the relative SNR. The phantom was smoothed using a Gaussian filter to mitigate PSF effects. Moreover, the spatial PSFs were simulated for all acquisition schemes by sampling a constant k-space signal (corresponding to a delta function in the image domain) for the same metabolites. For all simulations, T_2^* was set to 20 ms.

Off-resonance effects were simulated by changing the signal frequency (offset 10 and 30 Hz). Eddy current-induced gradient errors were simulated by weighting the positive and negative gradient lobes differently, introducing an error in the zero-order gradient moment (1 % discrepancy between the positive and negative gradient parts, with the PSF located at a distance from the centre equal to 50 % of the FOV along x and y). Movement was simulated by changing the position of the point source between the excitations (using a shift equal to 10 % of the FOV along the x and y axes during a full image encoding). For quantification, the PSF was integrated over the FOV and normalised to its maximum. The ratios between the corrupted and non-corrupted PSF values were used to determine the extent of the artefacts in the image domain. To determine the error in the spectral domain, the ratio of lactate to pyruvate was formed at the maximum of the PSF for both corrupted and non-corrupted PSF. These simulations were carried out for a thermal magnetisation to derive general conclusions.

In addition, a two-site model ([7], see also chapter 4) was used to illustrate the effects of enzymatic conversion and decaying magnetisation on SNR and PSF. To simulate pyruvate to lactate conversion, typical parameters of a hyperpolarised pyruvate measurement in tumour tissue were chosen: Apparent conversion rate constant from pyruvate to lactate $k_{Pyr \to Lac} = 0.1$ s^{-1}; longitudinal relaxation time $T_1 = 20$ s; inflow rate 0.2 s^{-1} ; duration of inflow 5 s. For FIDCSI, a variable flip angle scheme (VFA) [71, 109] for equal signal amplitudes of a decaying hyperpolarised magnetisation (estimated $T_1 = 20$ s) was used together with a repetition time of 100 ms to acquire one image. The start of the FIDCSI acquisition was set at the end of the pyruvate inflow. For EPSI, ISPCSI and SPCSI, a constant flip angle was used so that 10 % of the magnetisation are spent for encoding a single image within 4 s. These dynamic acquisition schemes were started at the beginning of the pyruvate inflow and repeated until signal depletion.

3.3.3 Reconstruction

FIDCSI

A 15 Hz Gaussian filter was applied along the readout dimension before the data were sorted into a zero-filled three-dimensional matrix. The FFT was applied along all three

dimensions.

EPSI

Data were sorted into a zero-filled three-dimensional matrix, and a 15 Hz Gaussian filter was applied along the spectral dimension. The FFT was computed along the spectral dimension, and the phase along the readout dimension was corrected to compensate for the spatial shift for each frequency. Subsequently, the FFT was applied along the spatial dimensions. For comparison, the full trajectory was reconstructed using the non-uniform fast Fourier transform (NUFFT) code by Fessler [112], where the gradient waveform itself was used for density compensation.

ISPCSI

A 15 Hz Gaussian filter was applied along the readout dimension. Image reconstruction was performed using least squares fitting to separate the individual metabolites [110]. A phase correction for the chemical shift evolution was applied for each metabolite. The NUFFT algorithm was used to reconstruct the spiral data on a Cartesian grid [112]. Density compensation was obtained according to [77].

SPCSI

Data were sorted into a two-dimensional matrix and a 15 Hz Gaussian filter was applied following the FFT along the spectral dimension. The phase along the readout dimension was corrected to compensate for the chemical shift for each frequency. Subsequently, Cartesian images were reconstructed using NUFFT [112] along the spatial readout dimension. Density compensation was obtained according to [77].

3.3.4 Software

MATLAB (MathWorks, Inc.) was used to implement the waveform design, simulations and reconstructions. Related code can be found at http://nmr-wiki.imetum.tum.de/13C/. All software was run on a standard notebook with 16 GB of RAM and an Intel Core i5-4200M processor.

3.4 Results

The relative SNR of the simulated test phantom is given in Table 4. In addition to the absolute values, the SNR was normalised to the FWHM of the PSF along both spatial dimensions. For the 16×16 acquisitions, FIDCSI scored the highest SNR, followed by ISPCSI and EPSI. Among the lower resolution acquisitions, FIDCSI also performed the best, followed by EPSI and SPCSI, where SPCSI has a significantly lower SNR because of the higher resolution.

The uncorrupted spatial PSFs are depicted in Figure 28 and their FWHM values are provided in Table 4. For FIDCSI and EPSI, the PSFs show notable truncation artefacts, which could be diminished by additional filtering at the cost of resolution.

Artefacts due to motion and gradient error can be observed in Figure 29 and in Figure 30 and the corresponding artefact ratio is given in Table 5. The non-Cartesian spiral sequences show a strong sensitivity to both motion artefacts as well as to gradient errors. In the presence of off-resonance effects, the PSF of ISPCSI is considerably blurred, resulting in a 9 % lower resolution for 10 Hz and a 125 % lower resolution for 30 Hz off-resonance (Table 5, Figure 31).

When including enzymatic conversion and decay, the simulations show a different impact on the sequences (see Table 6). For FIDCSI, a variable flip angle scheme is used which targets equal magnetisation for each excitation. As this considers only decay and not enzymatic conversion, there is an overweight of the outer k-space points for the metabolite signal, resulting in lower SNR and narrower PSF compared with a constant magnetisation. For dynamic acquisitions with constant flip angle, the (relative) SNR and PSF will vary slightly in each time frame because the signal will increase or decrease in the successive excitations of the same image frame. This effect was observed to be strongest for EPSI as the spatial encoding is split up into many phase encodes, whereas it seems to have a minor effect on the spiral sequences. For the average SNR and PSF, these fluctuations will cancel out.

sequence	SNR	SNR normalised to voxel size	PSF FWHM along x [mm]
FIDCSI 8 × 8	1.00	1.00	13.84
EPSI 8 × 8	0.80	0.77	14.37
EPSI full 8 × 8	0.88	0.89	13.78
SPCSI 8 × 8	0.46	0.99	9.41
FIDCSI 16 × 16	0.25	0.98	6.91
EPSI 16 × 16	0.17	0.67	7.59
EPSI full 16×16	0.19	0.92	6.37
ISPCSI 16 × 16	0.20	1.20	5.58

Table 4: Simulated signal-to-noise ratio (SNR) and point spread function (PSF) full width at half maximum (FWHM) of the investigated sequences.

sequence	artefact ratio (motion)	quantification error lactate/pyruvate (motion)	artefact ratio (gradient error)	quantification error lactate/pyruvate (gradient error)
FIDCSI 8×8	1.05	1.00	1.00	1.00
EPSI 8×8	1.11	1.01	1.00	1.01
EPSI full 8×8	1.11	1.02	1.00	1.01
SPCSI 8×8	1.50	1.03	1.22	0.97
FIDCSI 16×16	1.21	1.00	1.00	1.00
EPSI 16×16	1.30	0.99	1.01	1.01
EPSI full 16×16	1.36	0.97	1.01	1.01
ISPCSI 16×16	3.15	1.12	1.68	1.00

Table 5: Simulated point spread function (PSF) artefact ratio for motion (where the shift is 10 % of the field of view (FOV) distance along the x and y directions within one image encoding) and gradient error (1 % deviation between positive and negative gradient lobes). The artefact ratio is defined as the ratio of the integral of the corrupted PSF and the non-corrupted PSF, each normalised to its maximum. Quantification error lactate/pyruvate is taken from the ratio of the maximum of the PSF from corrupted and non-corrupted PSF.

sequence	average $\frac{SNR_{hyp}}{SNR_{therm}}$	$\frac{SNR_{hyp}}{SNR_{therm}}$ steepest rise/decline	average $\frac{FWHM(PSF_{hyp})}{FWHM(PSF_{therm})}$	$\frac{FWHM(PSF_{hyp})}{FWHM(PSF_{therm})}$ steepest rise/decline
FIDCSI 8×8	0.77	not applicable	0.93	not applicable
EPSI 8×8	0.99	0.62/1.05	1.00	0.85/1.03
EPSI full 8×8	0.98	0.64/1.02	1.00	0.85/1.03
SPCSI 8×8	1.01	0.94/1.00	1.00	1.00/1.00
FIDCSI 16×16	0.42	not applicable	0.92	not applicable
EPSI 16×16	1.00	0.56/1.12	1.00	0.87/1.03
EPSI full 16×16	1.02	0.58/1.09	1.00	0.87/1.03
ISPCSI 16×16	0.99	0.93/0.99	1.00	1.01/1.00

Table 6: Influence of inflow, enzymatic conversion and decaying magnetisation on point spread function and signal-to-noise ratio. Hyperpolarised simulation (labelled 'hyp') compared with thermal simulation (labelled 'therm'). Assumed values for the two-site model: $k_{Pyr \rightarrow Lac} = 0.1$ s^{-1}, $T_1 = 20$ s, inflow rate 0.2 s^{-1}, duration of inflow 5 s. Values shown are for lactate; PSF is taken along y (phase encoding direction for EPSI).
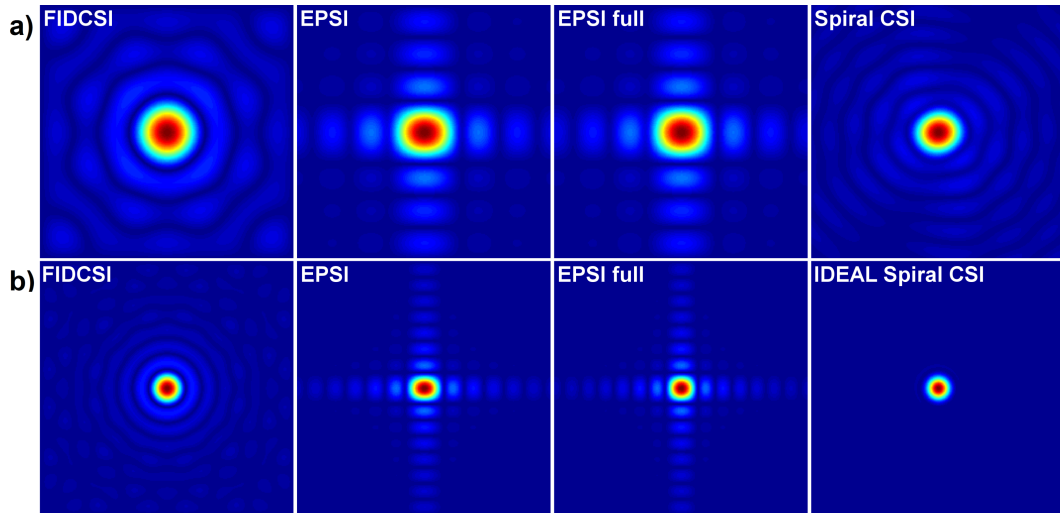
Figure 28: Two-dimensional spatial point spread functions of the investigated sequences for the lower (a) and higher (b) resolution.
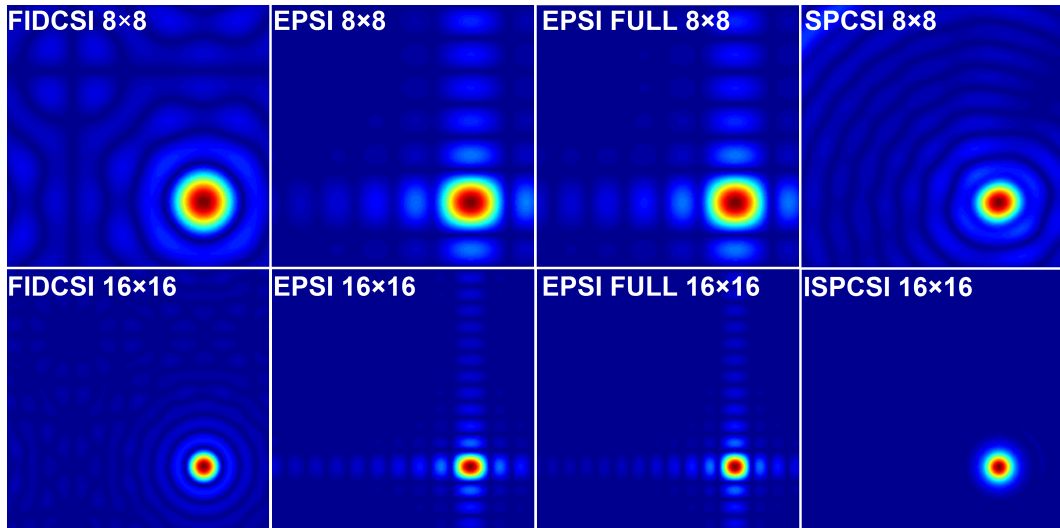
Figure 29: Two-dimensional spatial point spread functions of the investigated sequences for the lower (a) and higher (b) resolution under the influence of gradient errors. The spiral trajectories (ISPCSI and SPCSI) show the highest artefact ratio.
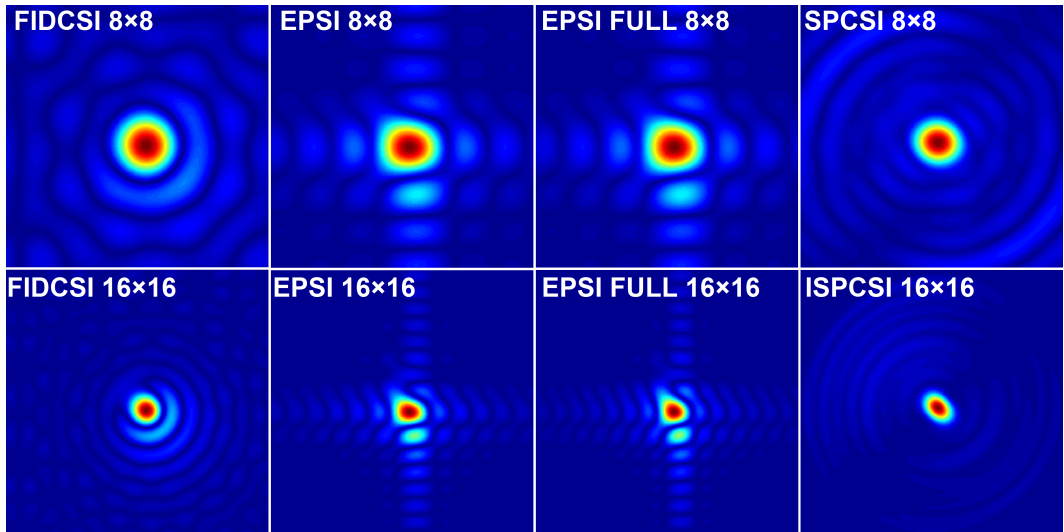
Figure 30: Two-dimensional spatial point spread functions of the investigated sequences for the lower (a) and higher (b) resolution under the influence of motion. Again, the spiral trajectories (ISPCSI and SPCSI) show the highest artefact ratio.
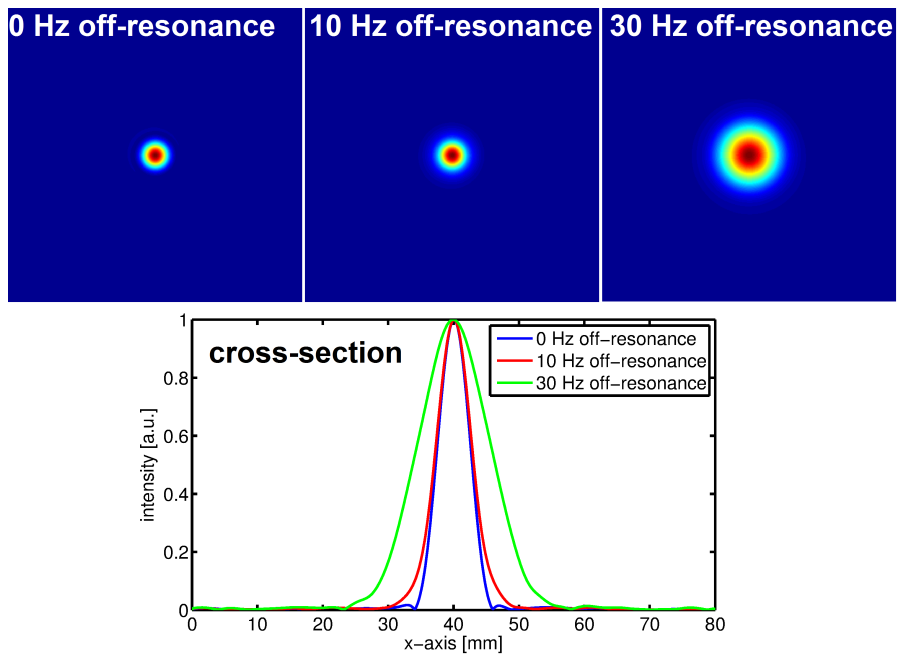
Figure 31: Simulated IDEAL Spiral CSI PSF in the presence of off-resonance. A strong blurring is observed, corresponding to decreased spatial resolution.

off-resonance [Hz]	relative PSF FWHM along x
0	1.00
10	1.09
30	2.25

Table 7: Simulated point spread function (PSF) for IDEAL spiral chemical shift imaging (ISPCSI) with off-resonance effects. Full width at half maximum (FWHM) is given relative to the case without off-resonance.

3.5 Discussion and Conclusions

This work focuses on the characterisation and comparison of different acquisition strategies for hyperpolarised ^{13}C metabolic imaging.

Compared with its competitors, FIDCSI has a low encoding efficiency. This prevents dynamic or multi-slice imaging, which would be required in certain scenarios. Furthermore, the long acquisition times can cause artefacts due to signal change. A variable flip angle scheme [71] can be used to counteract the in vivo signal dynamics, however, only pyruvate shows approximately an exponential decay whereas the metabolite curves depend on the enzymatic conversion and are not known a priori. Therefore, it is not possible to obtain equal signal amplitudes for each excitation when using a common soft-pulse. Spectral-spatial excitation pulses can be used to apply individual variable flip angle schemes for different compounds [113]. Still, the main advantages of FIDCSI are its robustness and benign artefact behaviour. As there is no active gradient encoding during readout, it is stable against gradient errors, and has a lower vulnerability to motion and flow. Moreover, because a full spectrum is acquired, it is inherently stable against off-resonance effects.

For dynamic acquisitions, no general recommendation for a certain strategy can be given; rather, the correct approach depends on the desired application. EPSI showed a solid performance for both 16×16 and 8×8 acquisitions, with a better SNR efficiency for the lower resolution because of lower gradient demands. As a full spectrum is obtained, it is stable against off-resonance effects, and the Cartesian sampling scheme reduces errors caused by motion and gradient imperfections. Its rectangular sampling pattern results in an anisotropic PSF, which could be modified using filters at the cost of resolution. However, it showed a stronger susceptibility to signal change caused by enzymatic conversion and decay.

ISPCSI and SPCSI can theoretically achieve slightly higher SNR values as shown by the simulations. The major advantage of these techniques is their high encoding efficiencies, permitting multi-slice or 3D acquisitions. However, non-Cartesian trajectories are more susceptible to both off-resonance effects and gradient imperfections. To reduce off-resonance artefacts, B_0 field maps could be incorporated in the reconstruction, or shimming approaches for the hyperpolarised scans could be established.

46

An in vivo comparison of the described sequences was performed and published along with the simulations in NMR in Biomedicine [100]. The evaluation of the in vivo data was conducted by Dr. Ulrich Koellisch. Hyperpolarised [1-^{13}C]pyruvate metabolism was studied in rats bearing a subcutaenous Mat BIII tumour; an exemplary dataset is shown in Figure 32. A high similarity between the hyperpolarised images acquired with different methods was found, and they correspond well to the anatomical proton images. IDEAL Spiral CSI showed a lower SNR compared to EPSI full 16 × 16 than predicted by the simulations in the tumour and kidney ROIs, and a significant blurring can be noticed in Figure 32 compared to the other techniques. This is probably caused by off-resonance; the corresponding B_0 map shows frequency shifts of approximately 20-30 Hz for ^{13}C in the tumour region. The SNR of the SPCSI acquisitions relative to EPSI full 16 × 16 was in good agreement with the simulated value. In the FIDCSI lactate image, some Gibbs-ringing can be noticed probably due to improper weighting of the k-space points caused by the variable flip angle scheme, as discussed above. For more information about the in vivo study, please see [100].
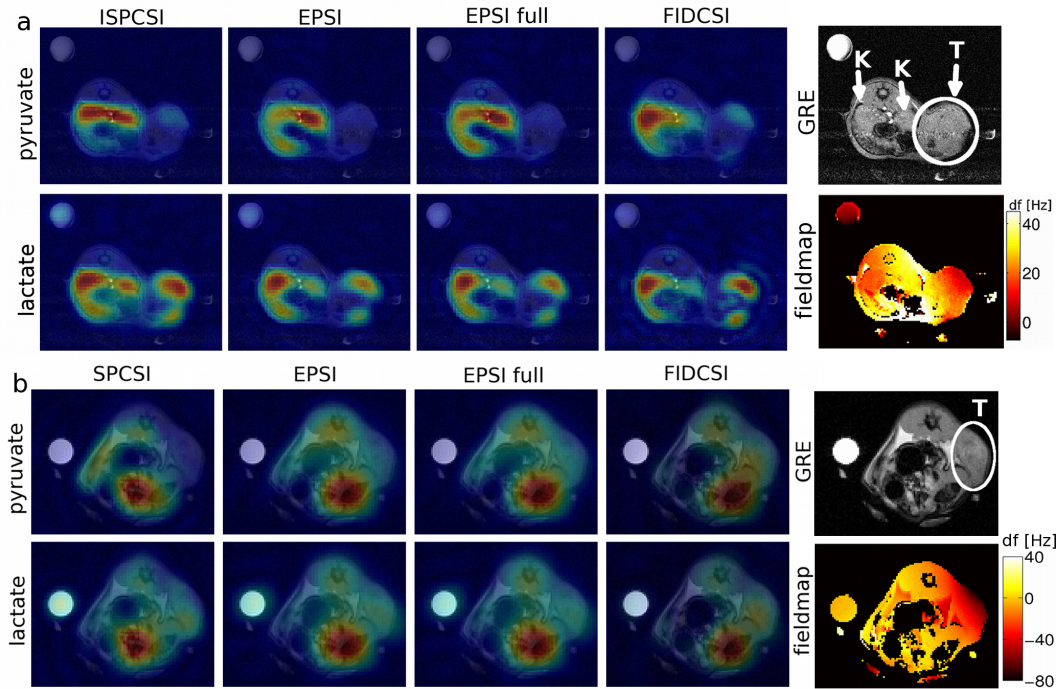
Figure 32: Images of hyperpolarised pyruvate and lactate in the tumour slice, acquired with the described sequences. a) acquisitions with the higher resolution (sum over 15 time steps) b) acquisitions with the lower resolution (sum over 18 time steps). The tumour (T) and kidneys (K) are marked in the anatomical proton image. The off-resonance for ^{13}C in Hertz is shown in the proton B_0 field maps on the right. Figure created by Dr. Ulrich Koellisch, as published in [100].

With regard to clinical applications, the SNR will very probably be the major limiting factor for most applications. The substrate concentration in tissue must be lower for

reasons of patient safety. Furthermore, the quality assurance process leads to a longer duration between dissolution and injection, resulting in a lower polarisation level of the injected solution. In addition, perfusion is slower in humans than in rats or mice. Therefore, the achievable spatial resolution will be severely limited by sensitivity, as can be observed in the first published studies [42]. With regard to sequence design, this will also result in lower gradient demands. Under these conditions, EPSI and SPCSI are the appropriate choices for the reasons mentioned above. For applications in which an entire organ needs to be scanned, multi-slice or phase-encoded three-dimensional imaging will be desirable. Therefore, efficient encoding techniques, such as SPCSI and ISPCSI, are favourable.

In conclusion, the comparison did not yield major weaknesses for any of the compared acquisition strategies, given that they are used with appropriate parameters. The simulations demonstrated that roughly comparable SNR (relative to the voxel size) can be achieved with all of the examined sequences. The choice therefore depends on secondary parameters, such as encoding efficiency and artefact behaviour. If acquisition time is not critical, EPSI is a robust choice for many applications. If multiple slices are to be acquired, or a high time resolution is needed, ISPCSI or SPCSI should be considered. FIDCSI is only an option for static acquisition where no time resolution is required. This chapter can only present a limited number of possible aspects relevant for hyperpolarised ^{13}C sequence design; however, the source code is provided (see Software section), and the reader is invited to study other details of interest.

4 Bolus Tracking for Improved Metabolic Imaging of Hyperpolarised Compounds

This chapter is an amended version of [105].

4.1 Introduction

When performing in vivo hyperpolarised magnetic resonance imaging, the timing of the acquisition is crucial for the quality and consistency of the obtained data [13]. After injection, the arrival of a hyperpolarised bolus in the target tissue can be observed along with the build-up of downstream metabolites. Currently, there are two major approaches for imaging hyperpolarised metabolism: The imaging acquisition can be dynamic, which means that the full time curves of the substrate (e.g. pyruvate) and metabolite signal are resolved by repeating multiple fast image acquisitions until the signal is depleted [16, 19, 24]. From the dynamic data, apparent conversion rate constants for the metabolic reactions can be fitted [7]. Alternatively, there is the static approach, which means acquiring one or a few images after a certain delay time when sufficient metabolite signal has been formed [15, 42, 92]. A metabolite-to-substrate ratio is then commonly used to evaluate metabolic activity.

However, both methods have intrinsic disadvantages. During the bolus arrival, the substrate signal is mainly determined by perfusion and does therefore not provide reliable information for kinetic modeling [114]. Moreover, exciting the spin system in this early state, when the substrate is mainly located within the blood pool, depletes a certain amount of polarisation which is subsequently not available for conversion any more, hence decreasing the metabolite signal. Furthermore, for segmented kt-space readouts such as EPSI [13–17] or IDEAL spiral CSI [18–21], the rapid signal change during the bolus arrival induces strong artefacts in the images. For refocused sequences such as spin echo [15, 102], it is important to start the acquisition after the hyperpolarised substrate has reached the target site because the imperfect refocusing of the moving molecules in the blood pool will quickly destroy the hyperpolarised signal. The quantitative results of single time point imaging depend on the state of the metabolic reaction, which is influenced by perfusion and other biological processes such as cellular uptake, and therefore commonly not known a priori. The bolus arrival time varies with heart rate, cardiac output, age, and vascular diseases which makes an accurate prediction difficult, especially for human application [42]. Moreover, in the case of a manual injection, operator dependent variations can occur.

In conclusion, this means that the dynamic approach is using the available hyperpolarised magnetisation inefficiently, whereas the static approach might produce inconsistent, unreliable or corrupted data due to timing variations (see Figure 34). Particularly for clinical application, many imaging methods established in preclinical trials may not be feasible due to lower SNR and longer perfusion times [42]. With regard to these challenges, knowing the current state of the injection and the metabolic conversion could allow to individually tailor the acquisition in real-time for optimal efficiency. To obtain the required data, excitations with a small flip angle ($<5°$) and a time resolution >1 s are sufficient

for most applications which means that only a negligible amount of magnetisation is lost due to monitoring. Therefore, it is advantageous to track the arrival of the hyperpolarised substrate and control the pulse sequence dynamically during a hyperpolarised in vivo experiment. A similar technique is already established for Gadolinium-enhanced MR angiography, where the bolus arrival of a Gadolinium-based contrast agent is tracked in real-time to start the actual image acquisition [115]. This technique has significantly improved the quality and reliability of MR angiographic images [116, 117].

In this work, dynamic real-time bolus tracking of the hyperpolarised ^{13}C signal was used to control the image acquisition in healthy rats after injection of hyperpolarised [1-^{13}C]pyruvate. A fully automated bolus tracking sequence is presented. It is demonstrated that optimised timing adapted to the bolus arrival and metabolic conversion results in increased metabolite SNR and reduced artefacts. Furthermore, a co-polarised injection of pyruvate and urea was applied. It is shown that spectrally selective tracking on urea allows obtaining high SNR bolus tracking information along with perfusion maps with high temporal resolution while at the same time not spending any pyruvate signal for tracking.

4.2 Theory

4.2.1 Hyperpolarised Signal Kinetics

The conversion of a hyperpolarised substrate to a metabolite can be described by a simple 2-site exchange model [7]. Neglecting back-conversion and assuming stable rate constants over time, the corresponding differential equations are given by:

$$\frac{dM_z(t)}{dt} = +k_{S \to M}S_z(t) - R_{eff,M}M_z(t) \tag{36}$$

$$\frac{dS_z(t)}{dt} = -R_{eff,S}S_z(t) + r_{in}(t) \tag{37}$$

where M_z is the longitudinal magnetisation of the metabolite, S_z is the longitudinal magnetisation of the substrate, $k_{S \to M}$ is the apparent conversion rate from the substrate to the metabolite, $R_{eff,M}$ and $R_{eff,S}$ are the effective relaxation rates of the metabolite and the substrate, respectively and r_{in} is the net inflow rate of the substrate. Assuming a rectangular input function with maximum value r_{in} which starts at t_{arr} and stops at t_{end}, the solution is then given by piecewise defined multiexponential functions [118]:

$$S_z(t) = \begin{cases} \frac{r_{in}}{R_{eff,S}}(1 - e^{-R_{eff,S}(t-t_{arr})}) & t_{arr} \le t < t_{end} \\[2ex] S_z(t_{end})e^{-R_{eff,S}(t-t_{end})} & t \ge t_{end} \end{cases} \tag{38}$$

$$M_z(t) = \begin{cases} \frac{k_{S \to M} r_{in}}{R_{eff,S} - R_{eff,M}} \left(\frac{1 - e^{-R_{eff,M}(t - t_{arr})}}{R_{eff,M}} - \frac{1 - e^{-R_{eff,S}(t - t_{arr})}}{R_{eff,S}} \right) & t_{arr} \leq t < t_{end} \\[2ex] \frac{S_z(t_{end}) k_{S \to M}}{R_{eff,S} - R_{eff,M}} \left(e^{-R_{eff,M}(t - t_{end})} - e^{-R_{eff,S}(t - t_{end})} \right) & \\ + M_z(t_{end}) e^{-R_{eff,M}(t - t_{end})} & t \geq t_{end} \end{cases} \tag{39}$$

Using these equations, the apparent rate constants can be obtained from either the differential form by direct matrix inversion or from fitting the data to the integral form. Another method for extracting kinetic information is to calculate the ratio of the areas under the time curve, which is equal to the ratio of $k_{S \to M}$ to $R_{eff,M}$ [119, 120]:

$$\frac{\int M_z(t) dt}{\int S_z(t) dt} = \frac{k_{S \to M}}{R_{eff,M}} \tag{40}$$

By using simple analysis, it can be derived from Equation 39 that the signal maximum of the metabolite is given by:

$$t_{max} = t_{end} + \frac{1}{R_{eff,S} - R_{eff,M}} ln \left(\frac{1 - e^{-R_{eff,S}(t_{end} - t_{arr})}}{1 - e^{-R_{eff,M}(t_{end} - t_{arr})}} \right) \tag{41}$$

Moreover, it can be directly derived from Equation 36 that, at the signal maximum of the metabolite, the following is valid:

$$\frac{M_z(t_{max})}{S_z(t_{max})} = \frac{k_{S \to M}}{R_{eff,M}} \tag{42}$$

This means if it is possible to measure at the maximum of the metabolite signal curve, the same kinetic information can be extracted from a single measurement without requiring the full signal curve. Moreover, the ratio of metabolite to substrate increases monotonically with time. Therefore, the ratio in the neighborhood of t_{max} provides a valid parameter which uniquely identifies the metabolic activity if the time point of measurement relative to t_{end} is known (see Figure 33).
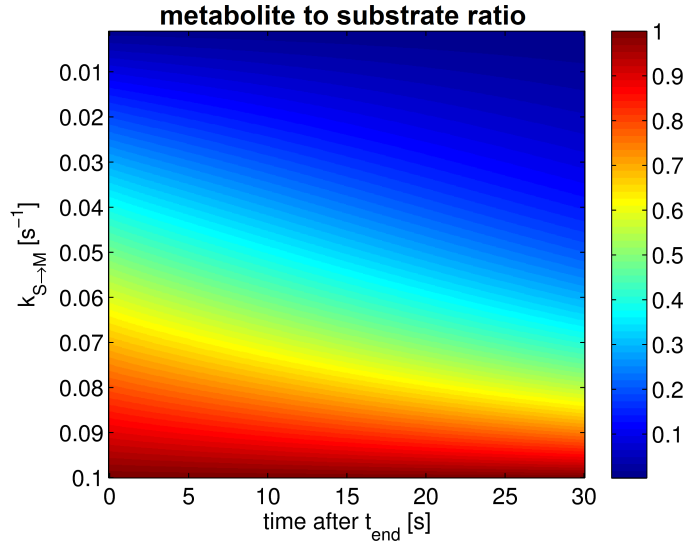
Figure 33: Metabolite to substrate ratio for varying values of $k_{S \to M}$ and varying acquisition times (separately normalised to highest value along k-axis, $T_1 = 25$ s). The ratio is a valid parameter to assess metabolic activity if the time point of the measurement relative to the end of the bolus t_{end} is known.

However, for single time point imaging, the state of the substrate/metabolite system is usually not well defined since the measurement is commonly started at a fixed time after injection. Depending on the transit time of the substrate from the injection site to the target site and the shape of the input function at the target site, the metabolite to substrate ratio can vary substantially which makes a quantitative evaluation of metabolic activity difficult. The time dependence of the lactate to pyruvate ratio ($M_z(t)/S_z(t)$) from a dataset of a tumour rat is shown in Figure 34 to illustrate the impact of this problem. A detailed quantitative analysis of metabolite to substrate ratios can be found in [114]. Even for dynamic imaging, the influence of perfusion is severe: As Li et al. demonstrated [114], on the left half of the curve until t_{end}, the kinetics are mainly determined by perfusion and the assumption of stable rate constants is not valid for the 2-site model without knowing the input function. Therefore, during this time interval, the acquired data is not reliable for kinetic modeling and it is more SNR efficient to start sampling after the bolus maximum. The same applies for saturation-recovery approaches, where the time steps until the bolus maximum are usually discarded because the initial inflow of substrate interferes with the kinetic modeling [57].
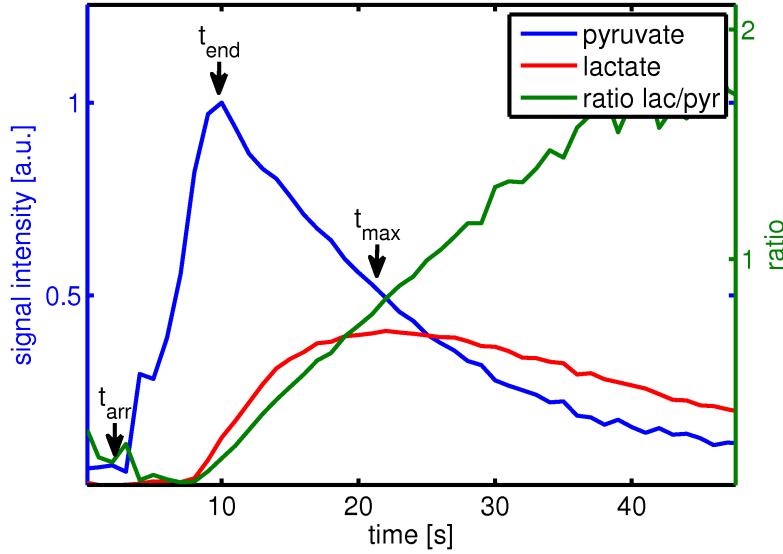
Figure 34: Dynamic curves and ratio of lactate and pyruvate obtained from FID acquisition (surface coil, 10° flip angle, $T_R = 1$ s) in tumour rat (subcutaneous MAT BIII) after injection of 80 mM hyperpolarised pyruvate solution (2.5 ml/kg bodyweight). The ratio varies substantially with time, therefore it is crucial to know the time point of the measurement relative to the bolus curve. Experimental data provided by Dr. Rolf Schulte.

For a 5° tracking sequence with a time resolution of 1 s, a worst case calculation shows that less than 5 % of the total pyruvate magnetisation is lost during a 15 s tracking period. For preclinical studies, even smaller flip angles should be possible. Regarding the SNR, it would be optimal to start at the metabolite maximum for a single time point acquisition. To get closer to it, either the range of expected rate constants can be estimated to calculate a rough estimate from Equation 41. Alternatively, the tracking data could be used to fit $R_{eff,S}$ of pyruvate or the beginning lactate curve. For a dynamic acquisition, the optimal starting point was simulated in Figure 35. With the given parameters, up to 20 % of total metabolite signal can be lost when starting too early.
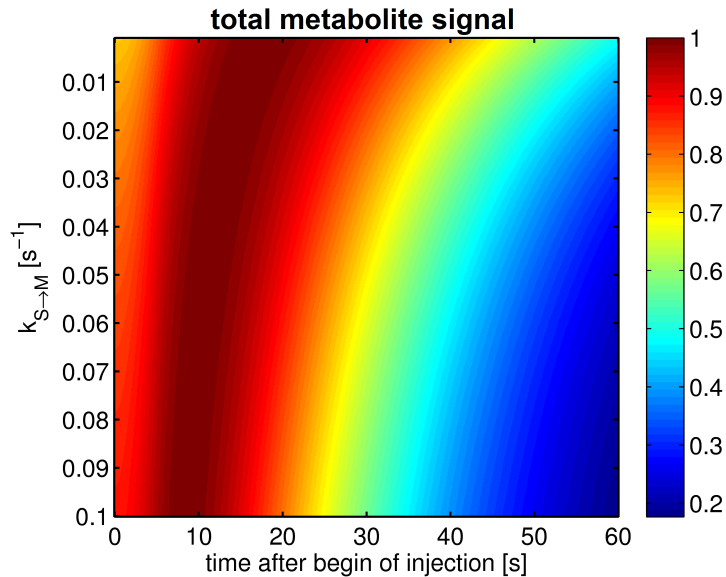
Figure 35: Total metabolite signal acquired with IDEAL spiral CSI depending on starting time (flip angle 10°, repetition time 250 ms, $T_1 = 25$ s, 5 s inflow with 0.2 s^{-1}, normalised to individual maximum along time axis). Up to 20 % of total metabolite signal can be lost when starting the acquisition too early.

4.3 Materials and Methods

4.3.1 Tracking Algorithm and Sequence Implementation

A simple and robust algorithm for the detection of the bolus maximum was implemented based on the smartprep algorithm [115]. The current signal is defined as the sum over the first points of the acquired FID signal. From a small number of calibration scans, the noise level is determined and a threshold is computed as $\nu_{thr} = n_{thr}\sigma$ where ρ is the standard deviation and n_{thr} is a scaling factor. After calibration, the hyperpolarised substrate is injected. If one of the subsequent signals is exceeding this threshold, the algorithm enters the actual detection phase. The algorithm checks for a fixed number n_{inc} of successive signal increases. If this condition is met, the algorithm enters the final phase of bolus detection. If in the following the signal is higher than the last signal, this will be set as the current signal maximum. If it is lower than the current maximum by a certain percentage μ_{dec}, the algorithm reports a successful bolus detection. A flowchart of the bolus tracking algorithm is depicted in Figure 36.

The bolus tracking was implemented on a 3T GE HDx system (GE Healthcare, Milwaukee, WI). The pulse sequence sends the acquired data in real-time via Ethernet to a separate reconstruction computer (2.4 GHz dualcore, 32 GB RAM) which runs the tracking algorithm described above (code written in C) and reports the current stage of the bolus arrival back to the pulse sequence. In principle, any single-shot acquisition scheme could be used for tracking with a low flip angle such as slice selective FIDs or gradient-encoded sequences to generate spatially localised tracking data. No hardware

changes were required to implement the described protocol.
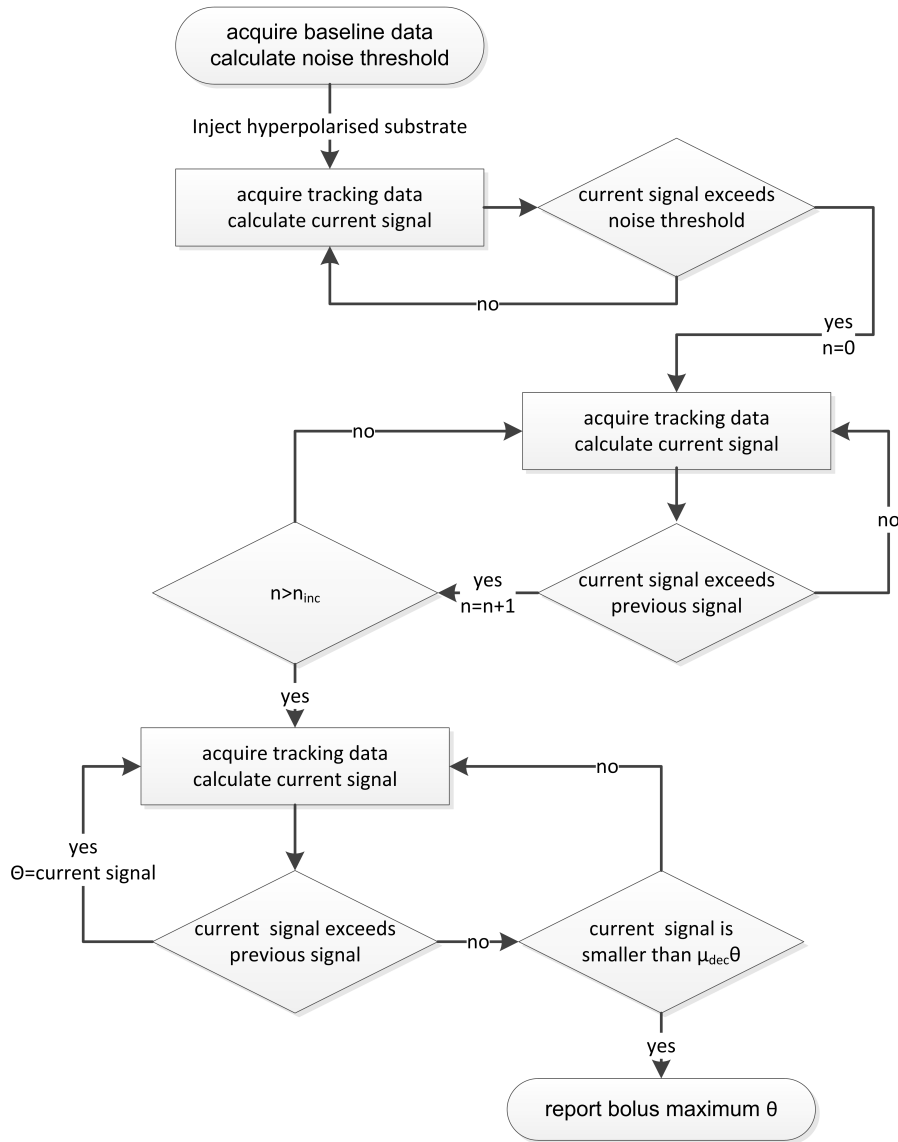
Figure 36: Flowchart of the bolus tracking algorithm. The data is evaluated in real-time on a separate reconstruction computer which detects the bolus maximum and reports it to the running pulse-sequence.

4.3.2 Experimental Setup

The bolus tracking algorithm described above was validated on existing datasets of slice selective spectral acquisitions (kidney slice) of healthy rats after injection of 80 mM hyperpolarised pyruvate solution [121]. After that, in vivo experiments on healthy rats were conducted. A dual-tuned ^{13}C-^{1}H birdcage volume-coil (diameter 8 cm) was used

for data acquisition [122]. A HyperSense DNP polariser (Oxford Instruments, Abingdon, UK) was used to polarise a sample containing [1-^{13}C]pyruvic acid mixed with 15 mM Trityl OX063 radical and 1 mM Dotarem. For the copolarised injections, [1-^{13}C]pyruvic acid and [^{13}C, ^{15}N$_2$]urea were hyperpolarised in frozen layers. After polarising for 1 h, the samples were dissolved by rapidly injecting a preheated buffer solution (80 mM Trizma buffer, 80 mM NaOH, and 0.1 g/L Na-EDTA). Finally, an 80 mM pyruvate and 80 mM pyruvate/100 mM urea solution was obtained, respectively with physiological pH, osmolarity, and temperature. The liquid-state polarisation was ≈ 25 %. After dissolution, 2.5 ml/(kg bodyweight) of this solution was injected into the tail vein of healthy male Lewis rats (average weight ≈ 350 g, injection time ca 5 s). The animals were anaesthetised with 1-3 % Isoflurane inhalation gas anaesthesia and checked for ECG, breathing, oxygen saturation and temperature. They were kept warm on a water-driven heating pad. In total, 9 healthy male Lewis rats (Charles River, Sulzfeld, Germany) were measured. The animal study was approved by the local governmental committee for animal protection and welfare (Tierschutzbehörde, Regierung von Oberbayern).

A central 10 mm kidney slice was selected to test the proposed method. The tracking sequence was started shortly before beginning the dissolution process. For the pyruvate experiments, a slice selective excitation with 5°, a repetition time of 1 s and plain FID readout (512 points, readout bandwidth 5 kHz) was used for tracking. For the pyruvate-urea co-polarisation, a spectral-spatial excitation pulse (15 lobes, each 1.12 ms long, total duration 17.5 ms [57]) was used for tracking, exciting only urea with a flip angle of 18°. A single-shot spiral readout (2812 points, 2.5 × 2.5 mm^2 nominal resolution, readout bandwidth 62.5 kHz) was used to encode urea perfusion maps with a time resolution of 1 s. After the bolus maximum was detected, an IDEAL spiral CSI sequence [19] (repetition time 250 ms, flip angle 10°, echo time shift 1.12 ms) was used with 7 echoes and an additional FID so that a full image block was acquired every 2 s using a sinc-shaped soft-pulse (duration 1.8 ms). Between bolus detection and imaging, a 4 s waiting period was included after detection of t_{max} to approach the metabolite SNR maximum (see Figure 34).

A second hyperpolarised pyruvate injection was acquired without tracking for comparison, started at the beginning of the injection. Six animals were tested with pyruvate tracking for the first injection, three of them were measured with slice selective spectra with 5° for the second injection to compare the bolus curves and the other three animals with the same IDEAL spiral CSI settings as mentioned above for the second injection. Another three animals were administered pyruvate-urea co-polarised injections and spectrally selective tracking on urea was used for the first injection, for the second injection they were again prescribed the same IDEAL spiral CSI sequence started at the beginning of the injection.

Image reconstruction was performed using a combination of least-squares fitting to separate the individual metabolites [110] and a gridding algorithm to interpolate the spiral data onto a Cartesian grid using the NUFFT code by Jeffrey Fessler [112]. A T_2^*-matched Gaussian filter was applied along the readout dimension with a line broadening of 15 Hz [57]. Kinetic modeling was performed on the conventional acquisitions using a frequency-domain fitting approach for the two-site exchange model [119].

4.4 Results and Discussion

The optimal bolus tracking parameters (n_{thr}, n_{inc}, μ_{dec}) for the in vivo experiments were extracted from existing measurements [121]. The noise threshold n_{thr} must be chosen so that it considerably exceeds signal variations due to noise but is lower than the expected hyperpolarised tracking signal. After an incoming hyperpolarised bolus was recognised, checking for a certain number n_{inc} of signal increases avoids the initial low SNR region of the substrate bolus. It needs to be chosen so that the tracking time during this section is shorter than the inflow time. After this, a signal decrease of μ_{dec} is used to detect the maximum. A reasonable μ_{dec} is big enough to ignore spikes induced by low SNR or motion and at the same time small enough to detect the bolus maximum before the metabolite maximum. Usually, the time interval between bolus maximum and metabolite maximum is on the scale of at least a few seconds even for rapid conversion in tumour tissue, which allows a robust detection of the bolus maximum before reaching the metabolite signal plateau. From the existing datasets, adequate parameters were found to be: $n_{thr} = 6$, $n_{inc} = 4$, $\mu_{dec} = 0.07$. The algorithm found the correct bolus maximum in 100 % of acquisitions (8 rats with 2 injections each).

Likewise, a bolus maximum was successfully detected in all in vivo bolus-tracking measurements. The comparison of the pyruvate time curves of the slice selective spectra and the bolus tracking data verifies that the correct maximum was indeed found (see Figure 37). Judging from the SNR of the pyruvate tracking data, even smaller flip angles should be possible without losing robustness. Although the magnetisation used for tracking is negligible, a smaller flip angle could then be used in combination with a shorter repetition time to increase the time resolution of the tracking process.
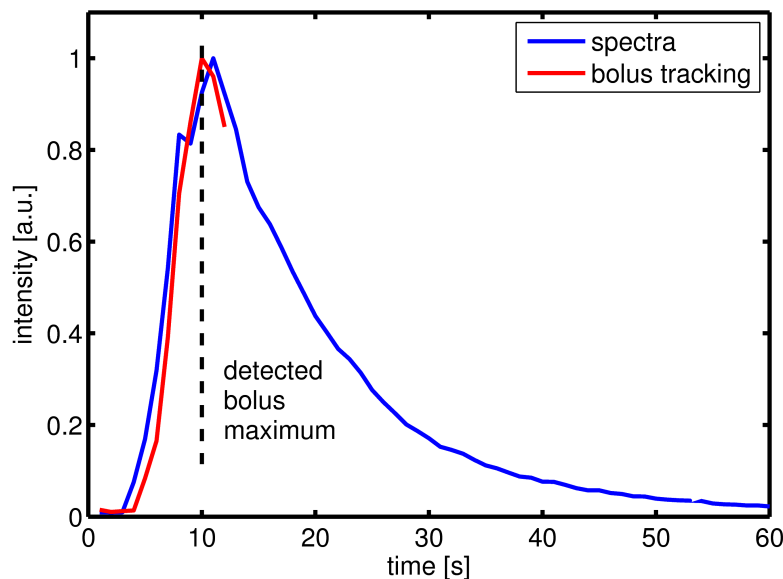
Figure 37: Comparison of pyruvate time curves obtained from two subsequent injections in the same rat (10 mm kidney slice): bolus tracking data and data from slice selective spectra (peak integration).

In the image time series of the conventional acquisition, strong artefacts resulting from rapid signal change and broad spectral point spread function can be observed, whereas the bolus-tracked acquisition is artefact-free (see Figure 38). This behavior is well known from earlier studies with IDEAL spiral CSI [21] where the corrupted images were discarded, which means that magnetisation was depleted to no purpose. The ratio of lactate to pyruvate gives a smooth estimate of metabolic activity, even for one time step (Figure 39), whereas the kinetic modeling map is noise dominated although it used the whole time curve as input. This behavior was also studied in [119]. The urea-tracked data shows the spatial localisation of the bolus which arrives first in the vena carva and then distributes to both kidneys (Figure 40). This is especially beneficial for perfusion measurements because the incoming bolus curve can be sampled at a high temporal rate. The slowly changing metabolite signals after the bolus can be sampled with higher repetition times for dynamic imaging, or with shorter repetition times for single time point imaging. Especially for tumours which can have a high degree of variability regarding vascularisation and perfusion, this additional information could help to better classify the metabolic imaging results.

Datasets with sufficient lactate SNR in both acquisitions were selected for analysis of metabolic activity (4 datasets). An evaluation of a kidney ROI lactate to pyruvate ratio from the first image of the bolus tracked acquisition was compared to the corresponding time point of the reference acquisition. The ratio of corresponding datasets differed to an average extent of 31 %, which is a reasonable agreement within the given conditions (low lactate SNR, 2 s time resolution for reference acquisition, biological variations).
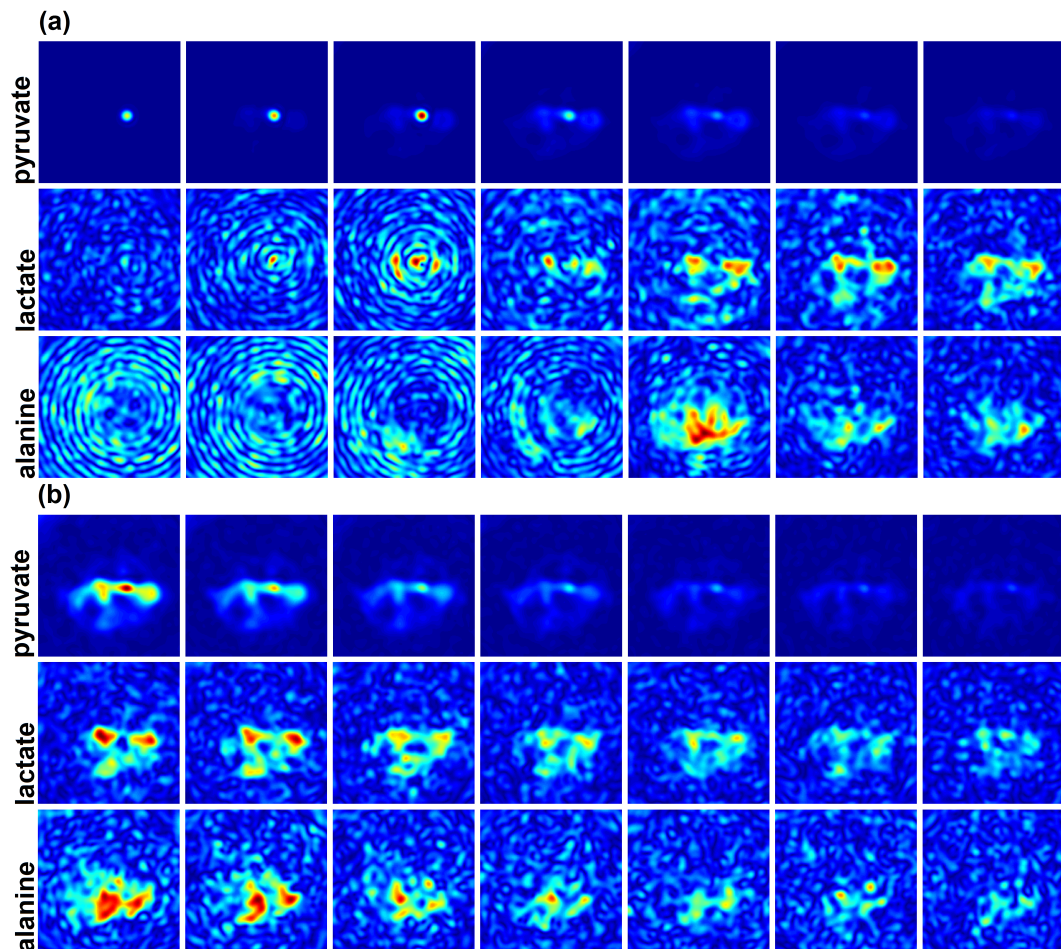
Figure 38: Comparison of acquisition started at begin of injection (a) and bolus-tracked injection started at 15 s after begin of injection (b), 8 time steps, 2 s between each image, 10 mm kidney slice after injection of 80 mM hyperpolarised pyruvate solution. Artefacts arising from rapid signal change and broad spectral point-spread-function (PSF) can be avoided with the bolus tracking approach.
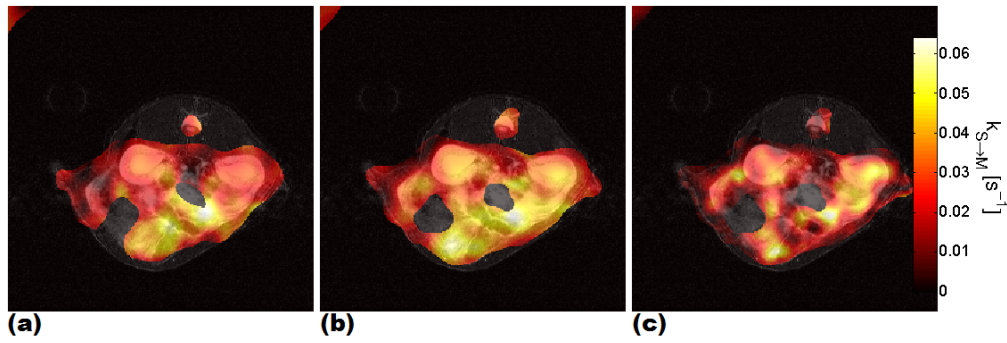
Figure 39: Comparison of single time point metabolite to substrate ratio (a), full time course metabolite to substrate ratio (b) and frequency domain kinetic modeling (c). Mask is based on pyruvate signal level to exclude low-signal regions.
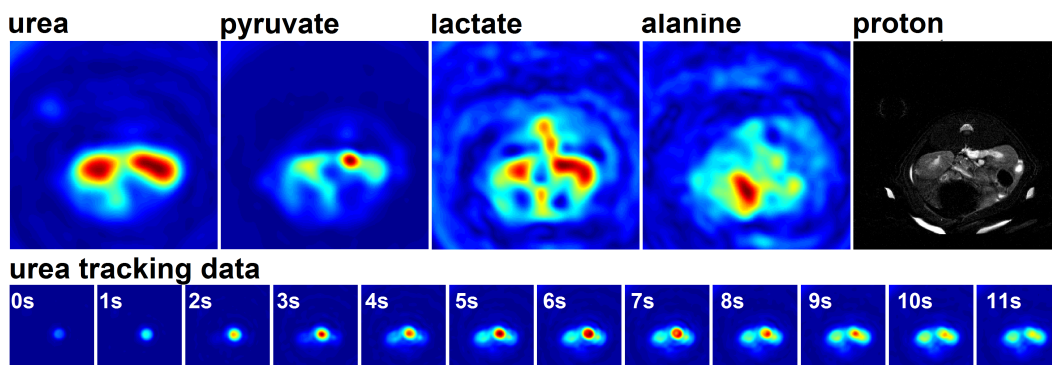
Figure 40: Dataset with hyperpolarised [^{13}C]urea tracking, 10 mm kidney slice after injection of co-polarised [^{13}C]urea/[1-^{13}C]pyruvate solution (upper row: sum over first 8 time steps).

The decision whether to directly track on pyruvate using a small flip angle excitation or on a copolarised secondary substrate such as urea mainly depends on the application. When the organ of interest constitutes the main part of the excited volume, such as for kidneys demonstrated here, there is usually no need for a secondary substrate except when the perfusion is very low and SNR becomes a problem. Within the given time resolution (1 s for urea tracking data, 2 s for pyruvate reference images from second injection), the bolus arrival within a kidney ROI was in accordance with the total signal taken from the first points of the FID. If there are other major sources of signal within the excited volume, urea tracking is preferable because due to the higher SNR, a spatially localised perfusion map can be acquired which provides specific information about the bolus arrival in the voxels of interest.

The presented sequence will remove the influence of varying transit times of the hyperpolarised substrate from injection site to target site. To also remove the influence of differently shaped input functions, a saturation pulse could be used selectively on the metabolites before starting the imaging acquisition. Future improvements could involve

for example dynamic real-time control of sequence parameters such as repetition time and flip angle. A real-time control panel could allow the operator to supervise the arriving bolus and intervene if necessary. If the tissue of interest needs to be spatially constrained, urea could be used in combination with a real-time reconstruction; or spatially selective excitation pulses could be used to select only the target volume. The tracking method could be improved to get a better estimate of the metabolite maximum by tracking on the metabolite or by including more sophisticated fitting methods. The possibilities of real-time signal processing are limited by the computing power necessary to reconstruct the data between two subsequent measurements, but even on current desktop hardware, simple FFT reconstructions are possible within a few 100 ms. Since the spatial resolution for hyperpolarised acquisitions is SNR limited and thus usually much lower than for proton acquisitions, real-time processing is much more feasible for this application.

4.5 Conclusions

A bolus tracking algorithm for hyperpolarised substrates was developed and verified in multiple datasets. Based on the algorithm, a fully automated bolus tracking sequence for hyperpolarised compounds was implemented and successfully applied to in vivo examinations with hyperpolarised pyruvate. Furthermore, the tracking sequence was modified to employ spectral-spatial excitation pulses. In combination with a copolarised pyruvate-urea injection, it was demonstrated that tracking can be selectively performed on urea without depleting the pyruvate magnetisation, while at the same time localised perfusion information can be obtained. Compared to existing imaging modalities, the proposed method reduces artefacts, allows for a more efficient use of the hyperpolarised magnetisation and ensures a higher reproducibility and consistency of the data. The monitoring of the bolus curve might also be useful to improve the efficiency of hyperpolarised perfusion mapping techniques. Particularly with regard to clinical application, the bolus tracking technique may constitute an important step towards a routine assessment protocol that removes operator dependencies and ensures reproducible results.

5 Non-Cartesian Parallel Imaging for Hyperpolarised ^{13}C Cardiac Studies in Pigs

5.1 Introduction

Hyperpolarised pyruvate metabolism has been studied in cardiac muscle cells in vitro [91, 123] and in vivo [41, 92–95, 124–128]. Following an ischemic event, significant changes in hyperpolarised metabolite concentrations were found. Metabolic imaging of the heart following injection of hyperpolarised pyruvate could therefore allow new methods for diagnosis and characterisation of heart disease.

The hyperpolarised pyruvate solution has a short lifetime ($T_1 \approx 60$ s in vitro) and each radiofrequency (RF) excitation will irreversibly decrease the hyperpolarised magnetisation. To accelerate the in vivo acquisitions, parallel imaging [64, 67, 129, 130], a method that uses complementary information provided by multiple receiver coils with spatially varying sensitivity profiles, could be used. By reducing the total acquisition time, it is theoretically possible to achieve a higher SNR for static imaging approaches as a result of decreased signal decay. However, parallel imaging cannot be used to improve the SNR of dynamic imaging of the metabolite time courses, because here the total acquisition time is fixed. In this case, parallel imaging could only help to overcome encoding limitations by speeding up the acquisition of a single image frame.

Hyperpolarised cardiac imaging would probably benefit most from faster sampling strategies because more images can be recorded in the short time window given by the cardiac triggering. A number of undersampling strategies have already been established for cardiac proton MRI based on parallel imaging, compressed sensing and spatiotemporal correlations [131–134].

However, hyperpolarised parallel imaging is challenging because of the SNR-limited spatial resolution and the rapidly decaying signal. Advantages of parallel imaging for hyperpolarised applications have been demonstrated for Cartesian sampling schemes [135–137]; the benefit for more efficient non-Cartesian sampling schemes in combination with IDEAL-based [110] metabolite separation for hyperpolarised imaging has yet to be explored.

In this work, the possibilities and challenges of hyperpolarised parallel imaging for non-Cartesian sampling schemes are discussed. A spiral parallel imaging sequence for metabolic imaging of hyperpolarised compounds is presented and applied to cardiac imaging in pigs after intravenous administration of hyperpolarised [1-^{13}C]pyruvate. It is investigated whether parallel imaging offers significant advantages compared to fully sampled acquisitions in this context.

5.2 Theory

In general, there are two main aspects constraining sequence design for hyperpolarised acquisitions: signal-to-noise ratio (SNR) and encoding efficiency. Unlike for traditional MRI, the total available signal is fixed by the initial polarisation level, and the acquisition scheme needs to efficiently spend it while at the same time meeting the encoding require-

ments for a given application. For dynamic imaging, the metabolic conversion needs to be followed over a defined time window with a certain temporal resolution, thereby fixing the total achievable SNR. On the other hand, when only a single image is acquired, a faster acquisition can improve SNR due to reduced T_1 decay. A high encoding efficiency is therefore desirable in both cases, and parallel imaging can be one option to improve this factor.

Conventional parallel imaging with thermally polarised samples will result in a decrease of SNR due to the reduced number of acquisitions and increased noise caused by ill-conditioning of the undersampled reconstruction problem. For hyperpolarised acquisitions, the longitudinal magnetisation decreases due to relaxation and RF excitations, therefore the total achievable signal is fixed which is a potential advantage for parallel imaging. The total SNR (sum of all excitations) can be described by (compare Section 2.4.2)

$$\text{SNR}_{sum} \propto \frac{P_0}{g\sqrt{N}} \sum_{n=1}^{N} (\prod_{j=1}^{n-1} e^{\frac{-T_R}{T_1}} \cos(\theta_j))\sin(\theta_n) \tag{43}$$

where P_0 is the initial hyperpolarisation, N is the number of excitations, T_R is the repetition time, T_1 is the longitudinal relaxation time of the hyperpolarised compound, g is the geometry factor and θ_j is the flip angle for the jth excitation. A general theoretical treatment of SNR for hyperpolarised parallel imaging is described in [138].

Thus, with a reasonably low g-factor, the total SNR is not lowered as with thermal polarisation, but a higher SNR could be achieved by reducing the total acquisition time. For hyperpolarised cardiac imaging, the T_R is determined by the cardiac trigger, allowing only a small time window for acquisition. In regard of this restriction, a potential speedup could help to overcome encoding limitations.

However, it is important to be aware that not all CSI sequences can benefit equally from parallel imaging. First parallel magnetic resonance imaging (PMRI) measurements with hyperpolarised pyruvate have already been published [135–137], yet, they rely on slow Cartesian k-space sampling schemes. For a standard phase-encoded FIDCSI sequence, it is straight-forward to skip phase encodes and achieve a high nominal reduction of excitations, but phase encoding is inefficient compared to non-Cartesian trajectories such as spirals and parallel imaging can only be used to slightly compensate for this inherent disadvantage. If prior knowledge is used to encode the spectral domain with a minimal number of time points, like in IDEAL, it is not feasible to further undersample the spectral domain because the reconstruction would not separate any more, and a meaningful reconstruction would probably not be possible at all. If IDEAL is combined with single-shot spatial encoding, like for example in IDEAL spiral CSI [19], the speed up could only be traded for a higher resolution, which is not practicable in this low SNR regime. Our conclusion is therefore that a sequence which encodes spatial and spectral information simultaneously along the readout and acquires the spatial domain with several interleaves is most favorable for parallel imaging by simply skipping some of the spatial interleaves. For hyperpolarised cardiac imaging and other applications, a flexible coil array is often used for improved SNR. For hyperpolarised ^{13}C experiments, this prevents the measurement of coil sensitivities with a phantom, since the orientation of the coil elements will be

64

different for the in vivo scan. Therefore, autocalibrated parallel imaging methods have to be employed in this case. Due to SNR limitations, typically only low resolution images of hyperpolarised imaging agents and its metabolites can be acquired. As conventional autocalibrated parallel imaging techniques require a fully sampled calibration region, the encoding efficiency of those approaches is significantly reduced because the calibration region constitutes a large part of the totally acquired k-space. Advanced strategies using dynamic calibration such as TGRAPPA [133] or self-consistent reconstruction algorithms without calibration [139] do not require the additional acquisition of a calibration region. This potentially yields a much higher net reduction factor and in combination with non-Cartesian trajectories provides an increased speedup.

For dynamic acquisitions such as metabolic imaging of hyperpolarised imaging agents, a time-interleaved k-space acquisition scheme enables a fully sampled calibration scan from adjacent time steps. Using conventional autocalibrated algorithms such as SPIRiT [65], each frame of the undersampled data can then be reconstructed separately, so no additional measurements are required. Furthermore, changes in relative coil sensitivities can be tracked dynamically during the acquisition. For non-Cartesian spiral imaging, a simple temporally interleaved k-space sampling scheme can be achieved by just rotating the spiral in subsequent excitations so that n rotations form a fully sampled acquisition.

5.3 Methods

5.3.1 Sequence Design

An undersampled spiral chemical shift imaging sequence (SPCSI, see Chapter 3) [24, 140] was implemented to include both the spatial and the spectral domain within a single-shot acquisition. After a slice-selective excitation pulse, an undersampled spiral trajectory is played out multiple times (see Figure 41a) followed by a rewinding gradient. The spectral width of this approach is determined by the time it takes to return to the same k-space point again. To increase the sampling density in the spatial and the spectral domain, multiple spiral interleaves can be played out in separate excitations, as well as time-shifted copies (see Figure 41b).

The designed trajectory has a field of view (FOV) of 150 mm, a nominal resolution of about $10 \times 10 \ mm^2$ and an interleave length of 2.4 ms (spectral width 417 Hz). Four $90°$ rotations are required for a fully sampled dataset in the spatial k-space domain. The undersampling was set to 3.0 in the k-space center and rises quadratically to 4.2 at the outer end of the spiral. One spiral readout train consists of 25 repetitions with a total readout time of 65 ms. To avoid aliasing in the spectral domain, an additional echo time shift ($\Delta T_E = 1.2$ ms) was implemented which results in a total of 9 excitations (4 rotations $\times$ 2 echo shifts + 1 FID). Relevant spectral aliasing patterns of [1-^{13}C]pyruvate and metabolites for the given approach are shown in Figure 42. To exploit the sparsity of the hyperpolarised ^{13}C signal (few, well separated frequencies, no background signal), a least-squares based metabolite separation approach can be used in the reconstruction [110]. To separate n species, a minimum of n echoes is necessary for separation, which allows for efficient sampling strategies. If the echo time increase is properly chosen,

noise amplification is negligible. The spiral trajectories were designed with the variable density spiral generation script by Brian Hargreaves [111].
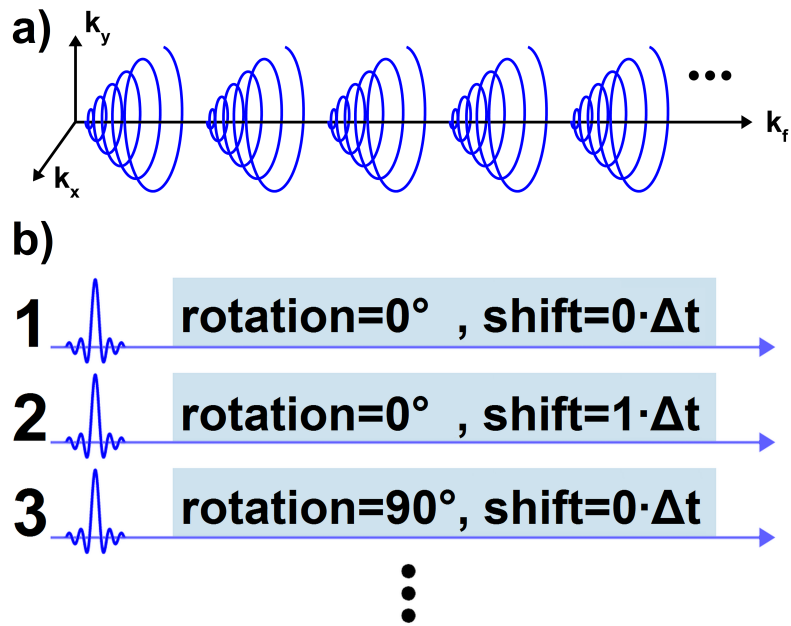
Figure 41: Sequence schemes. a) Scheme of spiral chemical shift imaging sequence b) Sequence scheme for undersampled spiral CSI. Fully sampled CSI data is obtained using rotations of the gradient as well as temporal shifts.
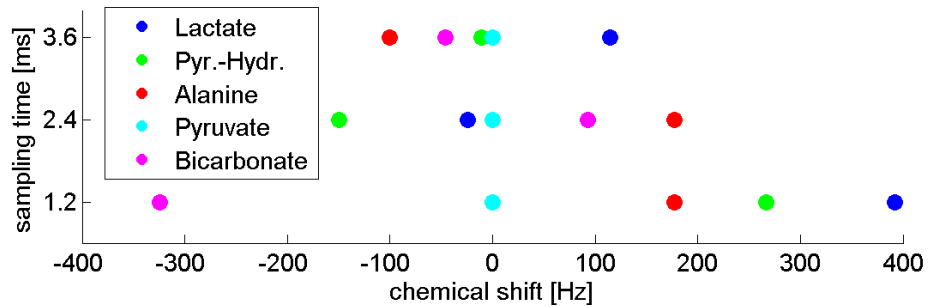
Figure 42: Spectral aliasing patterns of [1-^{13}C]pyruvate and metabolites for different echo time shifts between spiral interleaves. Using this information, the spectral bandwidth of the CSI sequence can be adapted so that the desired peaks are sufficiently separated.

5.3.2 Experimental

The animal experiments were conducted at the Fondazione CNR Regione Toscana in Pisa, Italy.

MRI Scanner Setup

Measurements were performed on a 3 T GE Excite HDx clinical scanner (GE Healthcare, USA) with a maximum gradient amplitude of 40 mT/m and maximum slew rate of 150 T/m/s. An ^{1}H body coil and a ^{13}C quadrature birdcage coil (Rapid Biomedical, Germany) was used for excitation. To receive the ^{13}C signal, a 16 channel flexible cardiac array coil (Rapid Biomedical, Germany) built for hyperpolarised ^{13}C cardiac acquisitions was used. The individual coil elements form a 4×4 array (element size 8×5 cm^2 (xz)) and neighbouring elements are decoupled by overlap (total array size of 26×19 cm^2). Mean S12 of neighbouring elements was measured - 17 dB, the ratio of loaded to unloaded Q was 98 / 135 = 0.73. This translates to an approximated SNR efficiency of 52 %.

Polarisation

A polarisation and dissolution method for large amounts of [1-^{13}C]pyruvic acid with a HyperSense DNP polariser (Oxford Instruments, UK) was used as described in [20, 141]. The obtained hyperpolarised solution contained 230 mM sodium [1-^{13}C]pyruvate, 109 mM Tris buffer, 0.12 mM EDTA and 16 nM Gd3+-complex. The solution had an average temperature of about 37 °C and a buffered pH of 7.6 ± 0.2. The sample was polarised for about 1 h, resulting in a liquid state polarisation level of approximately 16 %.

Animal Handling

The animal handling protocol was taken from previous studies [95]. Six healthy male farm pigs (average body weight ≈ 25 kg) were sedated prior to the experiments with a mixture of tiletamine hydrochloride, zolazepam hydrochloride (Zoletil 100, 8 mg/kg, i.v.) and atropine sulfate (0.1 mg/kg, i.v.). An ear-vein catheter in both ears was used for infusion of the pyruvate solution as well as for drugs. A continuous infusion of Propofol (2 mg/kg/h, i.v.) was used to anaesthetise the animals during the experiments. The animals were fasted overnight to increase the netmyocardial uptake of hyperpolarised [1-^{13}C]pyruvate [142] from the blood stream. A glucose infusion was applied to stimulate PDH activity and keep a constant glucose plasma level [143]. After dissolution, 20 mL of the hyperpolarised [1-^{13}C]pyruvate solution was injected manually into the right ear vein over a period of approximately 10 s. This protocol was approved by the Italian Ministry of Health and was in accordance with Italian law (DL.116, 27 January 1992), which conforms to the Guide for the Care and Use of Laboratory Animals published by the US National Institutes of Health (NIH publication no. 85-23, revised 1996).

67

Figure 43: Setup with sedated pig inside the 16-channel ^{13}C receive coil array and the birdcage ^{13}C excitation coil. Image provided by Dr. Rolf Schulte.

Acquisition Parameters

The heart was imaged in short axis view with 4 oblique slices, each with a slice thickness of 12 mm (see Figure 44). Cardiac triggering was used to acquire one excitation for each slice per heartbeat, resulting in an approximate repetition time (T_R) of 1 s. The described sequence consisting of 9 excitations was used to acquire one fully sampled image with a variable flip angle scheme [71] (approximated T_1 of 25 s). As the acquisition requires only few excitations and is very short ($<$10s), the main purpose of the variable flip angle scheme is to compensate for the loss of magnetisation due to RF excitation in order to obtain consistent k-space intensities. Additional whole-slice free induction decay (FID) acquisitions without gradient were appended, and for some animals, a preceding excitation was used to acquire a low-resolution single shot spiral CSI dataset for control purposes. The time delay from the start of the dissolution to the start of the bolus injection was around 18 $\pm$ 2 s to obtain sufficient metabolite signal.

Figure 44: Slice planning for hyperpolarised ^{13}C acquisition. The heart was imaged in short axis view with 4 oblique slices (slice thickness 12 mm). Screenshot provided by Dr. Francesca Frijia.

Reconstruction

The data was reconstructed using different sets of excitations to form various degrees of spatial undersampling. Before reconstruction, a Gauss-filter with 15 Hz line broadening was applied to the acquired signal to improve SNR. The different spiral interleaves were scaled to the same k-space signal intensity using the first few points of the readout. The slice-selective FID acquisition was used to check for anomalies as well as to determine the frequencies of the metabolites. For image reconstruction, a least-squares fitting approach was applied [110] to separate the individual metabolite signals. Subsequently, for the parallel imaging reconstruction, SPIRiT code by Lustig et al. [65] was used. Calibration was obtained from the fully sampled k-space data from all spiral interleaves; a SPIRiT kernel size of 3 × 3 was used. The reconstruction of the fully sampled images was performed using the NUFFT code by Jeffrey Fessler [112]. The SNR of the fully sampled images was determined from a region of interest from the slice with the maximum signal, respectively.

5.4 Results

In Figure 45, the fully sampled ^{13}C images of pyruvate and its metabolites are overlayed with anatomical proton images. The metabolite maps in Figure 45 show sufficient SNR, the myocardium can be clearly identified and the structure corresponds well to the anatomical reference. The fully sampled images can therefore be considered ground truth to judge the parallel imaging reconstructions shown in Figure 46. The gridded undersampled images show strong aliasing artefacts especially for an acceleration factor of 4 (Figure 46), whereas the SPIRiT reconstructed images are virtually aliasing-artefact free. However, it is difficult to judge the quality of the parallel imaging reconstruction as the SNR is low and the reconstructions use different acquisitions. For the fully sampled images, the mean lactate SNR for all animals was 18.3 ± 9.9, the mean pyruvate SNR 54.8 ± 18.7. For pyruvate, small signal streaks are present outside of the heart in some datasets (both fully sampled and undersampled), which may result from breathing, flow or signal sources outside the FOV. These are more pronounced in the parallel imaging reconstructions, probably because they average out in the fully sampled image which uses 8 excitations. For few acquisitions, a visible distortion was noticed, possibly caused by imperfect triggering. The homogeneity of the metabolite maps varies across datasets, most likely due to coil sensitivity profiles and T_2^* differences. The number of SPIRiT iterations required to remove the aliasing artefacts varied between 30 and 80, and increased for higher acceleration factors and higher SNR.
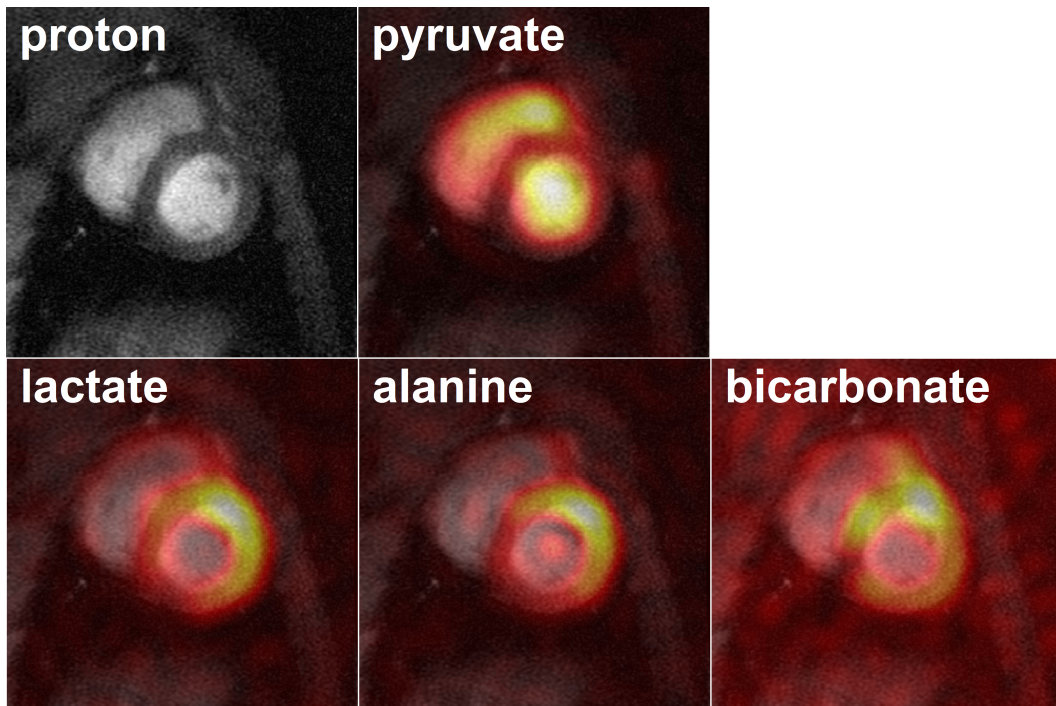
Figure 45: Fully sampled NUFFT reconstruction, overlayed with anatomical proton images for pyruvate, lactate, alanine and bicarbonate.
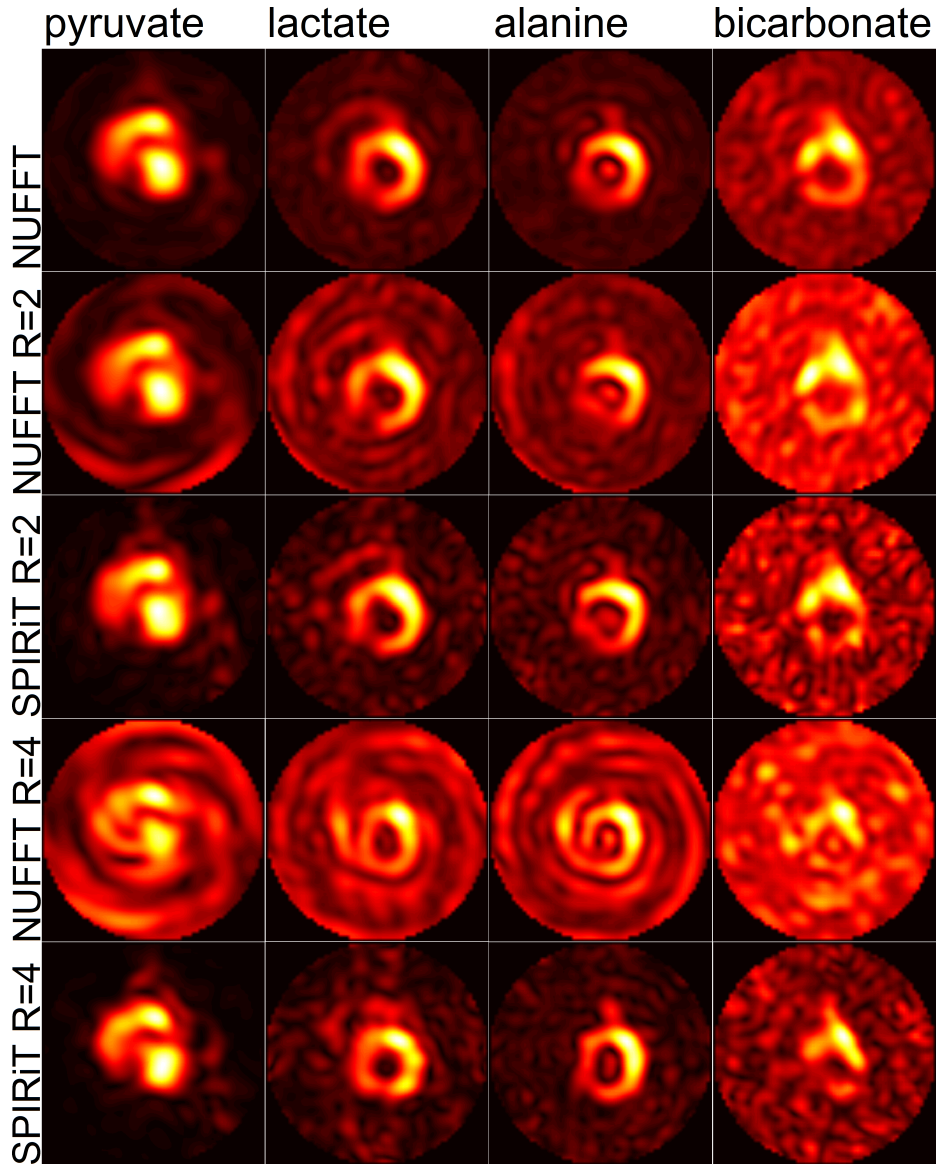
Figure 46: In vivo dataset with different reconstructions for pyruvate and metabolites. Fully sampled NUFFT reconstruction (NUFFT), 2-fold accelerated NUFFT reconstruction (NUFFT R=2), 2-fold accelerated SPIRiT reconstruction (SPIRiT R=2), 4-fold accelerated NUFFT reconstruction (NUFFT R=4), 4-fold accelerated SPIRiT reconstruction (SPIRiT R=4)

5.5 Discussion

At the time of writing, the question of when parallel imaging is beneficial for hyperpolarised acquisitions is still open. Unlike for traditional MRI, the total available signal for hyperpolarised acquisitions is fixed by the initial polarisation level, and the acquisition scheme needs to spend it as efficiently as possible. At the same time, it needs to meet

the encoding requirements for a given application, which could be eased by using parallel imaging. While this technique might be advantageous for inefficient Cartesian sampling schemes with a high encoding demand, it was demonstrated in this work that when using an encoding-efficient IDEAL-based non-Cartesian chemical shift imaging sequence, the benefits of parallel imaging are relatively limited.

As can be seen from Figure 47, depending on the g-factor, the possible SNR gain as a result of speeding up the acquisition with the given sequence is < 20 % in the best case with an assumed ideal g-factor of 1.0. Since a flexible coil array was used, the coil sensitivities are not known for the in vivo case and therefore, the g-factor could not be measured experimentally in this study. An average g-factor in the range of about 1.2 was reported for 4-fold acceleration with a similar parallel imaging pulse-sequence applied to proton spectroscopy using an eight-channel head-coil array [140].
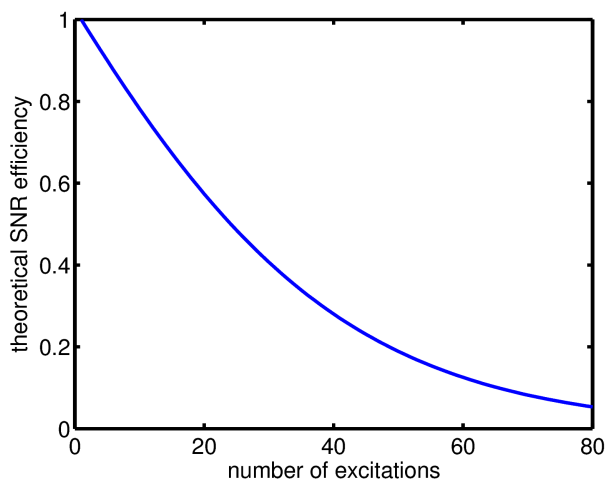
Figure 47: Theoretical hyperpolarised SNR efficiency for optimal variable flip angle scheme. The SNR was calculated for a fixed decaying magnetisation under the influence of RF excitation and T_1 relaxation ($T_R = 1$s, $T_1 = 20$s.). The optimal variable flip angle scheme for maximising the SNR was used for each data point, respectively.

Even in the context of cardiac imaging, where the cardiac triggering dictates a short time window, roughly 4 excitations per trigger are possible which allows obtaining multislice 2D images of the heart within a few seconds using the proposed sequence. As for the case of 3D acquisitions, the required number of excitations will increase by a factor equal to the desired number of phase encodes in z-direction, so that a 3D dataset with isotropic resolution could be acquired with $15 \times 8 = 120$ excitations in under 30 s. In this scenario, a speedup of factor 2 and 4 would only result in an SNR gain of factor 1.6 and 2.0, respectively, without considering the g-factor. For non-triggered acquisitions, this improvement would further deteriorate when using shorter repetition times.

Compared to the fully sampled images, no spiral undersampling artefacts were observed in the parallel imaging reconstructions; however, the SNR of the metabolite maps was very low. As there is practically no signal from surrounding tissue although the images

were acquired in short axis view, using a small FOV turned out to be favorable to further reduce the encoding requirements and ease the constraints for the design of the spiral trajectory.

Possible candidates for Cartesian parallel imaging are for example phase-encoded chemical shift imaging (FIDCSI) [7, 8], but for the 15×15 pixels resolution, $15 \times 15 = 225$ excitations are necessary for a single slice which is too long given the short life-time of the hyperpolarised compounds and the repetition time dictated by the cardiac trigger. Line based sampling, e.g. echo-planar spectroscopic imaging (EPSI) [13, 16] on the other hand can only be accelerated along one dimension so the 2D sensitivity profile of the coil array is not exploited to its full potential, resulting in lower acceleration factors. Therefore, non-Cartesian trajectories are the most feasible solution in the given setting. The proposed acquisition scheme can on the one hand be used without modifications to increase the time resolution of a hyperpolarised acquisition. For this approach, a dynamically calibrated reconstruction can be used as done in this work, by taking the coil sensitivity information from the fully sampled datasets with lower time resolution. This is similar to approaches such as TGRAPPA [133]. On the other hand, for speeding up the acquisition of a single image, a fully sampled low resolution acquisition could be included to obtain the calibration data. The porcine setup is similar to a clinical setting with human patients and the sequence operates well within the clinical safety limits. Therefore, these results allow conclusions about the performance in human studies and the acquisition scheme could be applied to clinical applications without fundamental changes.

5.6 Conclusions

In conclusion, the benefit of parallel imaging for hyperpolarised measurements is restricted to certain applications that are encoding limited. Since using parallel imaging will inevitably result in decreased SNR for dynamic acquisitions as a result of noise amplification in the reconstruction process, and hyperpolarised imaging acquisitions are usually SNR limited, it has to be carefully considered for each application whether the speedup is crucial. The in vivo experiments in pigs confirmed that the proposed spiral CSI sequence produces metabolic images which are at least comparable to the standard that can be found in the literature, while at the same time being much more encoding-efficient than Cartesian sampling schemes. For the majority of applications, a sophisticated choice of the sequence can therefore prevent the necessity of employing techniques such as parallel imaging and the associated loss of SNR.

6 α-Trideuteromethyl[^{15}N]glutamine: A Long-Lived Hyperpolarised Perfusion Marker

This chapter is an amended version of [144].

6.1 Introduction

Hyperpolarised agents have shown a great potential for a wide variety of biomedical applications. In particular, ^{13}C-labelled compounds, such as [1-^{13}C]pyruvate, have been widely examined because of the low natural abundance of ^{13}C, benign polarisation characteristics and involvement in key metabolic processes [6]. However, the in vivo lifetime of a hyperpolarised ^{13}C signal is typically below 1 min at clinical field strengths, which is mainly influenced by dipolar/paramagnetic interactions and chemical shift anisotropy contributions [145]. Therefore, only very rapid metabolic pathways can currently be measured with ^{13}C-based hyperpolarised biomarkers.

Several ^{13}C-labelled compounds have been proposed for measuring perfusion and transport [96, 97, 146–149], and [^{13}C]urea is the most promising candidate because it is an endogenous, metabolically inactive molecule. However, the T_1 relaxation times of these compounds are short as compared to the time scale of many physiological processes, such as renal filtering and excretion. Although first results regarding renal function have been demonstrated with [^{13}C]urea [148, 150], comprehensive evaluation is hindered by the rapid signal decay.

Assessment of renal function is vital for many diseases such as renal insufficiency, renovascular disease and metabolic disorders. Furthermore, renal function tests are required after renal transplantation, and abdominal trauma. Many non-invasive tests of renal function have been developed [151–154], however, they all have serious drawbacks such as ionising radiation, lack of precision or nephrotoxicity.

Recently, first in vitro tests of a new molecule for hyperpolarisation, α-trideuteromethyl-[^{15}N]glutamine have been published [28]. This molecule exhibits a particularly long T_1 time on the ^{15}N label because of deuteration, symmetrical structure and low gyromagnetic ratio. As a result of the added methyl-groups, it is metabolically inactive, which was confirmed by in vitro tests using glutaminase [99].

This chapter presents the first in vivo study with hyperpolarised α-trideuteromethyl-[^{15}N]glutamine. Using a single-shot spiral imaging sequence, hyperpolarised α-trideutero-methyl[^{15}N]glutamine was measured in a kidney slice of healthy rats. Moreover, the molecule was directly compared to hyperpolarised ^{13}C-labelled urea in the same animal. The findings suggest that α-trideuteromethyl[^{15}N]glutamine is a promising candidate for monitoring renal function.

6.2 Methods

6.2.1 NMR Scanner Setup

To measure the hyperpolarised ^{15}N signal, a clinical 3 T HDx system (GE Healthcare, Milwaukee, WI) was modified with a custom-built TR switch (RAPID Biomedical, Rim-

par, Germany) to receive and send at the ^{15}N frequency. Furthermore, a small animal ^{15}N butterfly transmit-and-receive coil with a diameter of 7 cm (Figure 48a) was used. An AMT 3T80 power amplifier (AMT, Omsk, Russia) with a range of 10-130 MHz was employed for RF excitation on the ^{15}N frequency (12.95 MHz at 3T). To obtain proton images for anatomical reference, the ^{15}N coil was placed in a ^{1}H head-coil. The complete setup is shown in Figure 48b. As the MRI scanner did not offer a setting for ^{15}N nuclei, the ^{15}N hardware was installed as a deuterium coil and imaging parameters were adapted taking into account the difference in gyromagnetic ratio.

Figure 48: a) Butterfly ^{15}N transmit-and-receive coil (7 cm diameter) b) in vivo ^{15}N hardware setup: 1) ^{15}N butterfly coil 2) ^{15}N TR switch by Rapid Biomedical (Rimpar, Germany) 3) proton head-coil (GE Healthcare) 4) rat bed.

6.2.2 Hyperpolarisation

Synthesis and hyperpolarisation of α-trideuteromethyl[^{15}N]glutamine was conducted by Dr. Enrico Chiavazza. The compound was synthesised as described previously [28]. A 2D structure of the glutamine derivative is depicted in Figure 49. The hyperpolarisation sample contained approximately 3 M α-trideuteromethyl[^{15}N]glutamine, 28 mM Ox063 radical (GE Healthcare) and 2.5 mM gadoteric acid (Guerbet, Villepinte, France) dissolved in ethylene glycol. A small amount of [1-^{13}C]pyruvate was added to the sample for measurement of polarisation build-up, as well as a small amount of D_2O to improve the glass forming properties. [^{13}C, ^{15}N$_2$]Urea was dissolved in glycerol and mixed with Ox063 radical ($\approx$ 28 mM) and gadoteric acid ($\approx$ 1.5 mM). The ^{15}N-labelled urea was used to avoid scalar coupling relaxation of the ^{13}C polarisation during transport outside of the magnetic field [98].
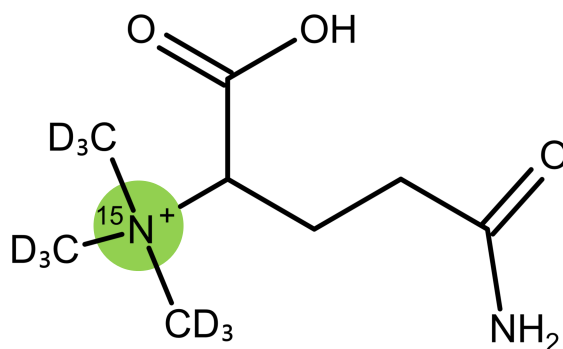
Figure 49: 2D structure of α-trideuteromethyl[15N]glutamine as described previously [28].

The mixtures were polarised in a HyperSense DNP polariser (Oxford Instruments, Abingdon, UK). After polarising for approximately 1-3 h, the frozen sample was dissolved by injecting hot D_2O solution containing 60 mM phosphate-buffered saline (PBS) and 0.1 g/L Na-EDTA. For the glutamine buffer, NaOH was added to compensate for the acidity. A hyperpolarised solution with physiological pH, osmolarity, and temperature was obtained. The urea concentration was approximately 150 mM, and the concentration of the glutamine derivative was approximately 100 mM.

6.2.3 Animal Experiments

Experiments were performed in four healthy male Lewis rats (Charles River, Sulzfeld, Germany). The animals were anaesthetised by 1-3 % isoflurane gas inhalation. Electrocardiogram, breathing, oxygen saturation and temperature were checked, and the animals were kept warm on a water-driven heating pad.
1 ml of hyperpolarised [13C, 15N$_2$]urea or α-trideuteromethyl[15N]glutamine solution was injected into the tail vein. One animal was injected with the hyperpolarised glutamine compound only; in three animals, two injections were performed in the same animal with hyperpolarised urea and hyperpolarised α-trideuteromethyl[15N]glutamine during the same session. For the urea acquisition, the animal was relocated into a dual-tuned 13C-1H birdcage volume coil (diameter 8 cm) [122] on the same bed.
The animal study was approved by the local governmental committee for animal protection and welfare (Tierschutzbehörde, Regierung von Oberbayern).

6.2.4 Mass Spectrometry

Mass spectrometry was conducted by Dr. Enrico Chiavazza. In two animals, blood and urine samples were taken after the injection as well as kidney samples after sacrificing the animal. The concentration of α-trideuteromethyl[15N]glutamine in the samples was determined using liquid chromatography-mass spectrometry (LCMS) with internal standard betaine (trimethyl glycine 118 m/z), and 20 μM limit of detection (LoD) (analyte 199 m/z).

6.2.5 Pulse Sequence Parameters

For frequency and flip angle calibration, a syringe filled with potassium nitrate-^{15}N was used for glutamine measurements and a syringe filled with [^{13}C]urea for urea measurements. The magnetic resonance measurement was started at the beginning of the injection. Imaging was performed in a kidney slice (about 2 cm thick) by using a soft-pulse and a single-shot spiral read-out (field of view 8 cm, nominal resolution 32 × 32 pixels). The flip angle was set to 10° and the first 16 excitations were acquired at an interval of 1 s to capture the bolus characteristics, after this a repetition time of 5 s was used. Every 15 excitations, a non-localised free induction decay (FID) acquisition was taken for control purposes. Proton gradient echo images (GRE) with identical FOV and orientation were acquired after the hyperpolarised injection to provide anatomical overlay.

6.2.6 Reconstruction

A 15 Hz Gaussian filter was applied along the readout dimension to improve the signal-to-noise ratio (SNR). A phase correction for the chemical shift evolution was applied using the frequency obtained from the FID acquisitions. Finally, a NUFFT algorithm was used to reconstruct the spiral data on a Cartesian grid [112]. Density compensation was obtained according to [77]. Proton GRE images were used for anatomical overlay. Regions of interest (ROIs) were drawn manually around both kidneys and the vena cava to obtain mean signal time curves from these areas. A monoexponential fit was used to determine the effective T_1 on the decaying slope of the signal time curves. One α-trideuteromethyl[^{15}N]glutamine injection was excluded from the fit as the slope may have been influenced by movement due to blood extraction during the measurement.

6.3 Results

No metabolites were detected for both tracers; a minor side product was visible in some ^{15}N spectra. The image overlay of the [^{13}C, [15]N$_2$]urea and α-trideuteromethyl-[^{15}N]glutamine data showed that both compounds were taken up by the kidneys (Figure 50). While the urea signal also appeared in other tissue parts, the signal of the glutamine compound was restricted primarily to the kidneys. Glutamine decay was sufficiently slow enough to obtain a quantifiable signal even after 5 min, whereas the hyperpolarised urea signal had disappeared after approximately 90 s (Figure 51). In the image time series, it can be observed that the signal first arrived in the vena cava and then spread out to the kidneys. From the imaging data, time curves from a region of interest within the kidneys were extracted (Figure 52). The effective decay time obtained from the decaying slope of the signal time curves (corrected for RF excitation) were determined to be 18 ± 1 s for urea and 146 ± 8 s for the glutamine compound. The SNR units shown in Figure 52 were determined using noise regions outside the rat body. Mass spectrometry analysis of tissue, blood and urine samples taken at different time intervals revealed a quick filtration and excretion within the time scale of the measurement (Table 8).
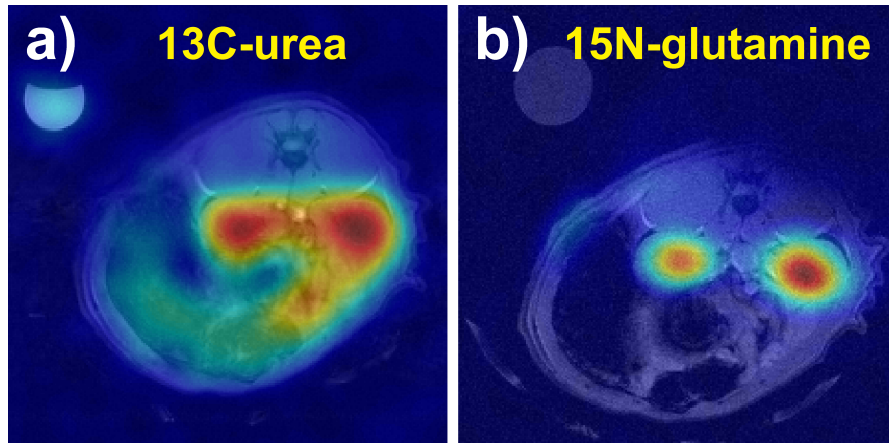
Figure 50: Sum over images after signal peak, overlaid with anatomical proton images.
a) $[^{13}C, {}^{15}N_2]$urea, b) α-trideuteromethyl$[^{15}N]$glutamine.
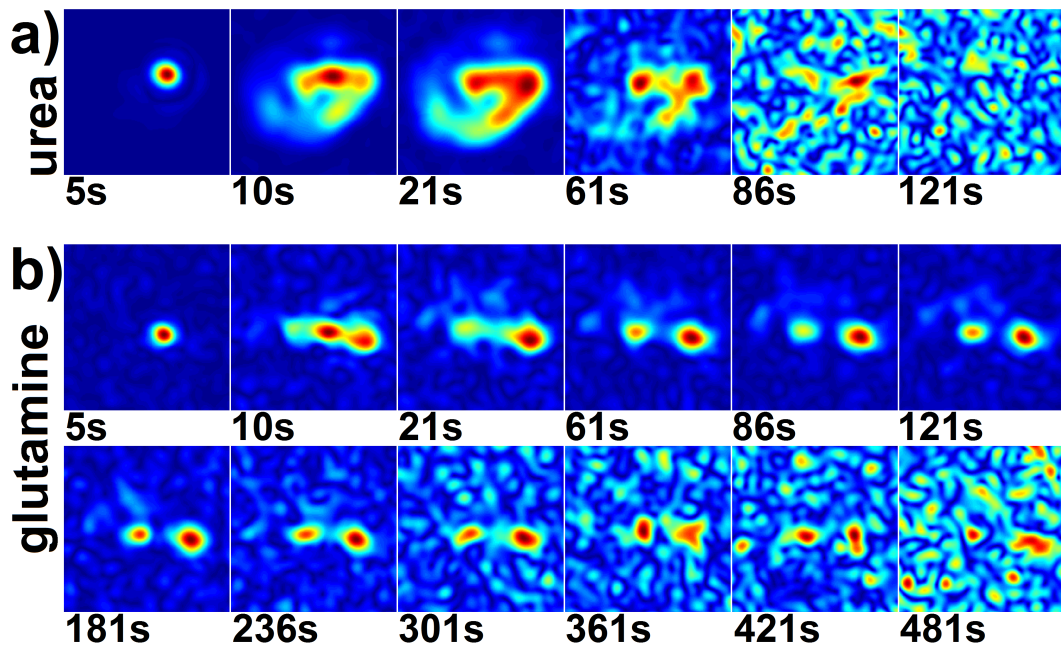
Figure 51: Single images at different time points, both were acquired with a 10° flip angle and a single shot spiral read-out (FOV 8 cm, nominal resolution 32 × 32 pixels).
a) $[^{13}C, {}^{15}N_2]$urea, b) α-trideuteromethyl$[^{15}N]$glutamine. Each image was scaled separately to its signal maximum to provide optimal visibility.

(a) $[^{13}C, {}^{15}N_2]$urea   (b) α-trideuteromethyl$[^{15}N]$glutamine
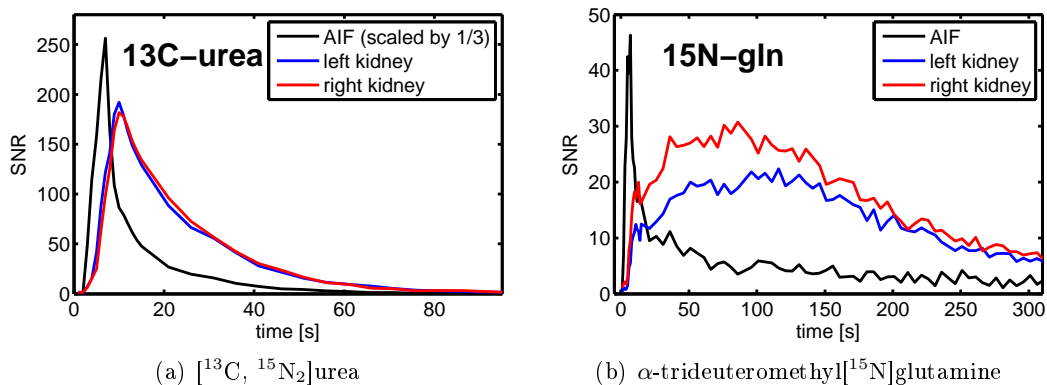
Figure 52: Signal time courses in SNR units from kidney and blood vessel ROIs, non-corrected for flip angle or T_1 decay.

Time after injection [minutes]	α-trideuteromethyl-$[^{15}N]$glutamine [mM]
Blood	
1	1.7 ± 0.2
2	0.8 ± 0.1
3	0.4 ± 0.05
7	0.3 ± 0.05
30	0.2 ± 0.02
130	$< \text{LoD}$
Urine	
30	7.5 ± 0.2
130	24 ± 1
Kidney	
30	0.3 ± 0.02
130	0.07 ± 0.02

Table 8: Concentration of α-trideuteromethyl$[^{15}N]$glutamine measured in blood, tissue and urine samples using liquid chromatography-mass spectrometry (LCMS), internal standard betaine (trimethyl glycine 118 m/z), limit of detection (LoD) 20 μM (analyte 199 m/z). Data provided by Dr. Enrico Chiavazza.

6.4 Discussion and Conclusions

The relaxation and polarisation properties of α-trideuteromethyl[^{15}N]glutamine have been extensively studied in [28]. Approximately 10 % liquid state polarisation and an extrapolated in vitro T_1 at 3 T of approximately 330 s were reported (see [28] for details). The significantly higher T_1 relaxation time for hyperpolarised α-trideuteromethyl-[^{15}N]glutamine compared to hyperpolarised [^{13}C, ^{15}N$_2$]urea (85 ± 7s in vitro at 3 T [98]) can be attributed to multiple factors. Given the low gyromagnetic ratio of ^{15}N nuclei ($\approx$ -4.316 $\frac{MHz}{T}$, corresponding to ≈ 40 % of the gyromagnetic ratio of ^{13}C and ≈ 10 % of the gyromagnetic ratio of ^{1}H), the interaction with external magnetic fields is reduced compared to nuclei with higher gamma such as ^{13}C. Moreover, the symmetrical environment of the ^{15}N label reduces the chemical shift anisotropy contribution. Another important factor is the deuterated methyl group, which minimises dipolar interactions that would occur with nearby protons. This study emphasises the potential of very long-lived hyperpolarised biomarkers based on ^{15}N. For example, long T_1 relaxation times have been previously demonstrated using ^{15}N-choline, making it an interesting biomarker for cancer diagnosis [155].

However, ^{15}N-labelled hyperpolarised compounds also introduce several new challenges. The SNR of a hyperpolarised scan is proportional to a value between γ and $\gamma^{(\frac{7}{4})}$, depending on the noise regime of the acquisition (e.g. compare [70]). For ^{15}N-labelled molecules, this means that the SNR will be reduced by a factor between 2.5 (sample noise dominance) and 4.9 (coil/electronics noise dominance) compared to ^{13}C-labelled molecules. For the butterfly coil used in this study, a value of $\frac{Q_{unloaded}}{Q_{loaded}} = \frac{194}{180} = 1.08$ was determined for the ratio of the quality factors for the unloaded and loaded coil. This indicates that coil noise dominated in the given setup. To decrease SNR loss, improved coil designs can be used. For example, cryo-coils can provide a significant SNR increase at low frequencies [156]. Moreover, for systematic polarisation tests, it may be beneficial to modify the polariser to be able to detect ^{15}N signals.

In regard to sequence design, the low γ also means that higher magnetic field gradient strengths are required for spatial encoding. However, as no chemical shift information must be encoded for the hyperpolarised glutamine compound, gradient demand is not a severe constraint in this case when using an encoding-efficient spiral trajectory. As an advantage, absolute off-resonance caused by B_0 inhomogeneity will be equally reduced, allowing for non-Cartesian encoding with few blurring artefacts, as demonstrated in this work. To distinguish the structural properties of the kidney, a steady-state free precession (SSFP) sequence may provide improved SNR efficiency, allowing to encode a higher resolution [150]. In addition, a real-time bolus tracking approach could be used to acquire data at optimal time points [105].

As the investigated glutamine derivative is structurally different from endogenous glutamine, additional studies of the biological properties of this compound are required. Previous toxicity tests found no adverse effects at concentrations much higher than those used in this study [28]. Given the toxicity of ethylene glycol, it would be beneficial to establish a protocol with a more benign glassing agent such as glycerol.

Comparing images of [^{13}C, ^{15}N$_2$]urea and α-trideuteromethyl[^{15}N]glutamine, the glu-

tamine compound exhibited increased localisation of the signal in the kidneys with a lower background signal compared to that of urea. This is probably due to the fact that while urea is taken up by different tissue types, there is no cell transporter for the modified glutamine molecule and therefore it is essentially only rapidly filtered and excreted. This was also confirmed by the mass spectrometry analysis. The slow decay of the hyperpolarised glutamine compound enabled a quantifiable signal to be obtained in the kidneys even after several minutes. Compared to existing hyperpolarised agents, these results may enable a whole new range of applications. At 146 s, the effective T_1 in the kidneys was approximately 8-fold higher than that for urea. For these reasons, hyperpolarised α-trideuteromethyl[^{15}N]glutamine is an ideal tracer for studying renal diseases and may potentially allow the determination of filtration rates and tubular properties, as well as the characterisation of the collecting system using hyperpolarised agents. A simple kidney clamp model can be employed for the first tests in a pathologic setting.

In daily clinical routine, blood tests [151, 152] based on properties such as creatinine clearance are used to assess renal function. However, while they are inexpensive and relatively easy to carry out, blood tests do not provide spatial localisation, and may provide insufficient results in cases of unilateral kidney diseases. Single-photon emission computed tomography-based methods [157] however, provide spatial localisation, but expose the patient to ionising radiation, and radiotracers are difficult to produce and handle. X-ray computed tomography (CT) examinations also involve ionising radiation, and the iodinated contrast agents exhibit a high nephrotoxicity [158]. Gadolinium-based contrast agents [153, 159] show a non-linear relationship between tracer concentration and signal, and can induce nephrotoxic effects in patients with renal insufficiency [160]. The presented hyperpolarised agent is non-radioactive, easy to produce and offers a direct proportionality of signal to concentration. Moreover, it can be administered in a copolarised injection together with a metabolically active biomarker such as [1-^{13}C]pyruvate or [1,4-^{13}C$_2$]fumarate as a necrosis marker to obtain complementary information from the tissue.

In conclusion, first in vivo results with a ^{15}N-labelled hyperpolarised perfusion marker are presented. In rat kidneys, effective T_1 times were approximately 8-fold higher than those of hyperpolarised ^{13}C-labelled urea. Hyperpolarised α-trideuteromethyl[^{15}N]glutamine is a highly promising candidate for renal studies because of its long signal life time, strong localisation, and rapid excretion.

7 Probing Lactate Secretion in Tumours with Hyperpolarised Nuclear Magnetic Resonance

This chapter is an amended version of [161].

7.1 Introduction

In contrast to normal cells, the majority of cancer cells exhibit a high rate of glycolysis and predominantly produce energy by fermenting the generated pyruvate to lactate even in the presence of oxygen (please see Section 2.8.1). This phenomenon, also called the Warburg effect, is the foundation for FDG PET examinations routinely used in clinical practice for diagnosis and treatment response monitoring in cancer patients.

To maintain energy production and prevent toxicity, the generated lactate needs to be rapidly transported out of the cell. Pyruvate and lactate cannot cross the cell membrane by free diffusion due to their electric charge but their transport is catalysed by proton-linked monocarboxylate transporters (MCTs) [162]. These transporter proteins are driven solely by the concentration gradients of the target molecule and surrounding protons, thereby also contributing to regulation of intra- and extracellular pH.

Excessive lactate production and secretion are linked to many crucial steps in the progress of cancer: High levels of lactate in tumours are related to increased metastases and cancer cell resistance to radiotherapy [163–165] as well as to significantly lower overall survival rates of patients [166–168]. Studies indicate that exogeneous lactate stimulates tumour angiogenesis, growth and metastasation [169–173]. Moreover, high extracellular lactate concentrations were found to reduce the immune response to cancer cells by compromising the metabolism of immune cells [174–176]. There is also a symbiotic relationship between cancer cells which release lactate as a waste product and other cancer cells which use it to fuel their energy production. Overall, MCTs play an essential role in cancer metabolism and development [177–179]. Therefore, a deeper understanding of MCT activity in tumours is highly desired and is currently the subject of intense research.

As MCTs occupy a key position in the energy production of cancer cells, they also represent a promising target for new cancer therapies [180]. For example, α-cyano-4-hydroxycinnamic acid, a drug that inhibits lactate transport in mammalian cells, was shown to reduce growth and induce necrosis in cancer cells by restricting lactate efflux, thus impairing glycolytic energy production [181–184].

DNP offers the unique possibility to study pyruvate to lactate metabolism in vivo in a noninvasive way. However, the measured lactate signal not only reflects enzymatic conversion but is also affected by various other parameters such as perfusion, cell membrane transport, intra- and extracellular pool sizes and polarisation decay. Various approaches have been introduced to disentangle this complex interplay of biological processes such as direct quantification of inflow and outflow in bioreactors [185, 186], using saturation and inversion transfer methods to quantify the label exchange between substrate and metabolite pools [187], injecting hyperpolarised alanine to determine intracellular pyruvate and lactate levels [188], using commercial relaxation agents that partially destroy extracellular magnetisation to measure altered conversion rates [189], and exploiting different

T_2 relaxation [190, 191] or using diffusion gradients [192–196] to distinguish different microenvironments. However, these methods suffer from serious drawbacks involving challenges for in vivo applicability, lack of sensitivity, or ambiguity of results. Currently, a method for measuring cell transporter activity in vivo is not available.

Here, a Gd(III)DO3A complex [197] is used that binds to pyruvate and its metabolites to efficiently destroy extracellular magnetisation after hyperpolarised lactate has been formed. Both slice-selective spectroscopic and imaging data were acquired in rats with a subcutaneous mammary carcinoma. In combination with a newly developed pulse sequence that saturates pyruvate magnetisation, considerably increased lactate signal relaxation was measured in the presence of GdDO3A which indicated high rates of lactate efflux from the tumour cells. To our knowledge, this study is the first to demonstrate a non-invasive measurement of cell membrane transporter activity in vivo by using hyperpolarised ^{13}C pyruvate in combination with a tailored relaxation agent.

7.2 Theory

7.2.1 GdDO3A

The idea of quenching the extracellular biomarker hyperpolarisation has been reported earlier [189, 198]; however, commercially available relaxation agents can only provide limited relaxation since they rely solely on outer-sphere interaction with the hyperpolarised molecule. Using a coordinatively unsaturated Gd(III)DO3A complex (gadolinium-1,4,7,10-tetraazacyclododecane-1,4,7-triacetic acid, see Figure 53 and [197]), theoretically, a higher efficiency in destroying the hyperpolarisation of pyruvate and its metabolites can be achieved.
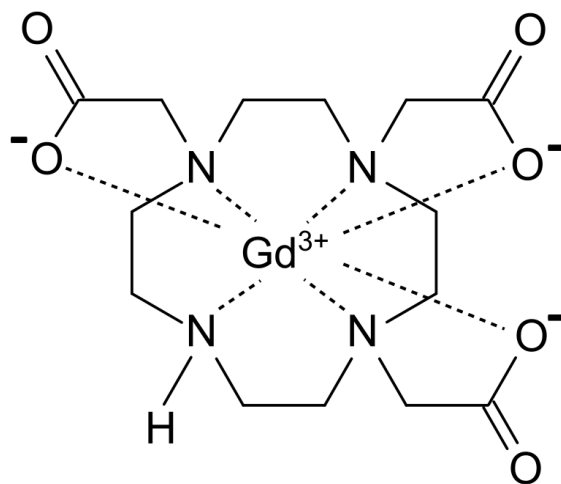
Figure 53: Structural formula of GdDO3A (gadolinium-1,4,7,10-tetraazacyclododecane-1,4,7-triacetic acid, compare [197]). Adapted from [199].

The heptadentate ligand offers two vacancies in the inner coordination sphere of the Gd(III) ions that can be occupied by donor atoms from a variety of anionic substrates

such as pyruvate or its metabolites. For several α-hydroxy-carboxylates such as lactate, the formation of a stable ternary adduct has been observed [197] as shown in Figure 54. More information about this Gadolinium-chelate and its properties can be found in [197].
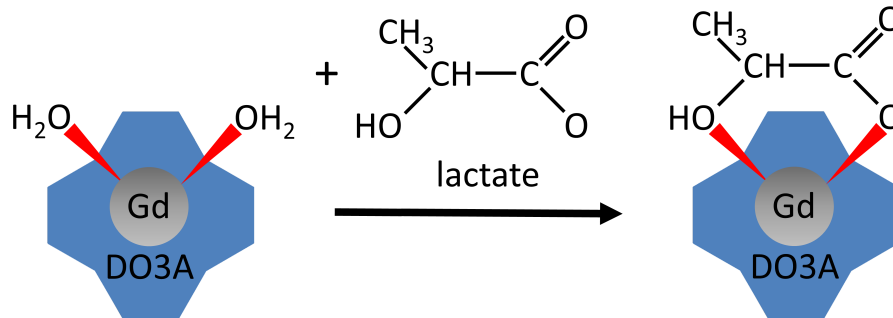
Figure 54: Formation of a reversible ternary adduct between GdDO3A and lactate (see [197]).

Therefore, it is expected that GdDO3A will provide increased relaxation compared to coordinatively saturated complexes such as Gd(HP-DO3A) or Gd(DTPA) for these compounds. Due to the size of the complex, it will remain outside of the cell and can therefore be used to specifically quench extracellular magnetisation.

7.2.2 In Vivo Pyruvate Signal Kinetics

After injection, the hyperpolarised pyruvate arrives at the tumour site where it is taken up by the cancer cells via MCTs. Inside the cell, pyruvate is metabolised mainly to lactate by lactate dehydrogenase (LDH) and to alanine by alanine transaminase (ALT). The lactate generated is then exported to the extracellular space again by MCTs. To deduce the transporter activity, pyruvate signal kinetics need to be described by a multicompartment model considering intra- and extracellular signal portions. Assuming constant conversion and transporter rates, and neglecting back reaction and back transport, this will result in an intricate set of coupled differential equations:

$$\frac{d}{dt}P_{ext} = -R_{1,ext}P_{ext} - k_{P,ext\to int}P_{ext} + r_{if} \tag{44}$$

$$\frac{d}{dt}P_{int} = -R_{1,int}P_{int} + k_{P,ext\to int}P_{ext} - k_{P\to L}P_{int} - k_{P\to A}P_{int} \tag{45}$$

$$\frac{d}{dt}L_{ext} = -R_{1,ext}L_{ext} + k_{L,int\to ext}L_{int} \tag{46}$$

$$\frac{d}{dt}L_{int} = -R_{1,int}L_{int} + k_{P\to L}P_{int} - k_{L,int\to ext}L_{int} \tag{47}$$

where P and L are the longitudinal pyruvate and lactate magnetisations, $k_{P\to L}$ and $k_{P\to A}$ are the apparent conversion rates for pyruvate-to-lactate and pyruvate-to-alanine conversion, $k_{P,ext\to int}$ and $k_{L,int\to ext}$ are the apparent rates for cell membrane transport of pyruvate into and of lactate out of the cell, r_{if} is the net pyruvate inflow rate, R_1 is the

spin-lattice relaxation rate and the indices *ext* and *int* denote the extra- and intracellular compartments, respectively.

A standard FID signal does not contain any information on compartmentalisation and is the total of intra- and extracellular components. To crush the extracellular magnetisation, GdDO3A can be injected when lactate has formed and the results of this measurement can be compared to those of an acquisition without the relaxation agent. However, the ongoing inflow, uptake and conversion of pyruvate results in an additional lactate signal modulation since pyruvate will also be crushed when GdDO3A is present. Furthermore, the lactate signal in the measurement with GdDO3A can still be modulated due to the conversion of intracellular pyruvate and label exchange from alanine over pyruvate to lactate. To remove these effects, a frequency selective saturation pulse on pyruvate can be used to quench the pyruvate magnetisation in both measurements, leaving only the magnetisation of the metabolites. Then, the lactate magnetisation can be described by two simplified coupled differential equations for extra- and intracellular magnetisation:

$$\frac{d}{dt}L_{ext} = -R_{1,ext}L_{ext} + k_{L,int \to ext}L_{int} \tag{48}$$

$$\frac{d}{dt}L_{int} = -R_{1,int}L_{int} - k_{L,int \to ext}L_{int} \tag{49}$$

where, for the measurement with GdDO3A, $R_{1,ext}$ is time-dependent due to the inflowing contrast agent.

When a high extracellular concentration of GdDO3A is assumed, the magnetisation of the lactate transported to the extracellular compartment will be crushed almost immediately and only the intracellular compartment remains

$$\frac{d}{dt}L_{int} = -R_{1,int}L_{int} - k_{L,int \to ext}L_{int} \tag{50}$$

The apparent membrane transporter rate can then be calculated straight forward as the difference in the measured decay rates between the acquisition with and without added GdDO3A:

$$k_{L,int \to ext} = R_{L,eff,Gd} - R_{L,eff} \tag{51}$$

where $R_{L,eff,Gd}$ denotes the effective relaxation rate of lactate with added GdDO3A and $R_{L,eff}$ the effective relaxation rate of lactate without GdDO3A. The behaviour of alanine magnetisation is analogous to that of lactate magnetisation. Please see also Figure 55 for a graphical illustration.
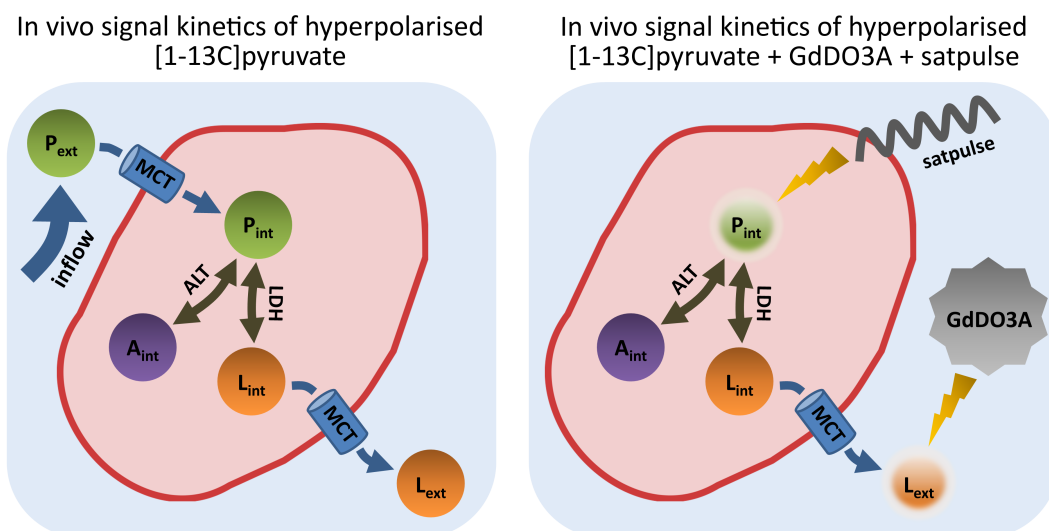
Figure 55: In vivo signal kinetics of hyperpolarised [1-^{13}C]pyruvate in a cancer cell. Left: Standard NMR acquisition, intra- and extracellular compartments cannot be separated, right: saturation pulse destroys pyruvate magnetisation and only metabolite magnetisations are left. If transported out of the cell, the metabolite magnetisation will be quenched by GdDO3A. Therefore, the MCT transporter activity manifests as additional decay in the presence of GdDO3A.

7.3 Materials and Methods

7.3.1 GdDO3A Relaxation Properties

GdDO3A relaxation properties were measured by Dr. Francesca Reineri. The longitudinal relaxation times of the ^{13}C label of [1-^{13}C]pyruvate, [1-^{13}C]lactate and [1-^{13}C]alanine were quantified in serum (FBS) with varying concentrations of GdDO3A. Assuming a 1 ml injection of 80 mM pyruvate is diluted in 15 ml of rat blood, the concentration of pyruvate was chosen to be 5 mM, while 0.5 mM was used for lactate and alanine. The results were compared to those of measurements with commercially available Gd(HP-DO3A) (trade name: ProHance). These experiments were performed at 14 T (Bruker Avance 600 MHz spectrometer), using the inversion recovery pulse sequence.

7.3.2 Hyperpolarisation

A sample consisting of [1-^{13}C]pyruvic acid mixed with 15 mM trityl OX063 radical and 1 mM Dotarem was polarised in a HyperSense DNP polariser (Oxford Instruments, Abingdon, UK). After polarising for 1 h, the frozen sample was dissolved by injecting a hot buffer solution containing 80 mM Trizma buffer, 80 mM NaOH, and 0.1 g/L Na-EDTA. The final solution contained 80 mM pyruvate at physiological pH, osmolarity, and temperature. The liquid-state polarisation was approximately 25 %.

7.3.3 Scanner Setup

In vivo experiments were performed on a clinical 3T HDx scanner (GE Healthcare, Milwaukee, WI) with maximum gradient amplitude of 40 mT/m and maximum slew rate of 150 T/m/s. For the acquisition, a dual-tuned ^{13}C-^{1}H birdcage volume coil (diameter: 8 cm) was used [122].

7.3.4 Animal Handling

The proposed protocol was tested in 8 male Fischer F344 rats (Charles River) with a subcutaneous Mat BIII tumour in the neck region. Tumours were grown for about 10 days and reached a size of $\approx$ 1.5 cm. The animals were anaesthetised during the measurements with 1-3 % isoflurane gas inhalation. ECG, breathing, oxygen saturation and temperature were checked, and the animals were kept warm on a water-driven heating bed. Then, 1 ml of dissolved 80 mM hyperpolarised pyruvate solution was injected into the tail vein. The animal study was approved by the local governmental committee for animal protection and welfare (Tierschutzbehörde, Regierung von Oberbayern).

7.3.5 Immunohistochemistry

Immunohistochemical assays were conducted by Dr. Katja Steiger. Subcutaneous Mat BIII tumours from 5 separately implanted rats were harvested and fixed in 4 % neutral-buffered formalin. After embedding the tumours in paraffin, 2 μm consecutive slices were cut. Immunohistochemical assays were conducted to determine MCT1 and MCT4 expression using MCT1 (Merck-Millipore, catalogue number AB1286-I) and MCT4 (Santa Cruz Biotechnologies, catalogue number sc-50329) antibodies and secondary goat anti-chicken (MCT1, medac diagnostics 16-24-06) or goat anti-rabbit (MCT4, medac diagnostics, catalogue number 71-00-30) antibodies. The secondary antibodies were retrieved in a heat-mediated process for 20 minutes in citrate buffer (pH 6). A streptavidine-peroxidase antibody detection system (medac diagnostics, catalogue number 71-00-38) visualized by Dab (medac diagnostics, catalogue number BS04) was used.

7.3.6 Pulse Sequence Design

A 2D spectral-spatial RF pulse [53, 57] was used to selectively excite pyruvate or its metabolites. The pulse consisted of 18 lobes with total pulse length of 22.4 ms and used flyback-gradients to increase robustness against gradient errors.
For spatial encoding, a single-shot spiral gradient readout (FOV 8 cm; resolution 24 $\times$ 24 pixels; maximum gradient amplitude 13 mT/m; maximum gradient slew rate 46 T/m/s) was created using the variable density spiral generation script by Brian Hargreaves [111]. A spectroscopic acquisition sequence was implemented using the spectral-spatial RF pulse. First, the pulse was executed on the pyruvate frequency without slice selection using a flip angle of 90° and a subsequent spoiler gradient. Then, lactate and alanine signal was acquired slice-selectively with a flip angle of 6° in subsequent excitations with a repetition time of 100 ms so that a full set of metabolite signals with preceding pyruvate

saturation was obtained every 300 ms. The readout time was 51.2 ms with a readout bandwidth of 5 kHz and a total of 256 points.

For imaging, the repetition time was increased to 200 ms and the pulse sequence was modified to include three excitations using the pyruvate saturation pulse without slice selection followed by slice-selective excitations with 20° on the lactate and alanine frequency. The single-shot spiral readout gradient was used for spatial encoding. A full set of metabolite images with preceding pyruvate saturation could be obtained every second. The readout time was 65.5 ms with a readout bandwidth of 62.5 kHz and a total of 4096 points. For a schematic drawing of the individual pulse sequences, please see Figure 56.
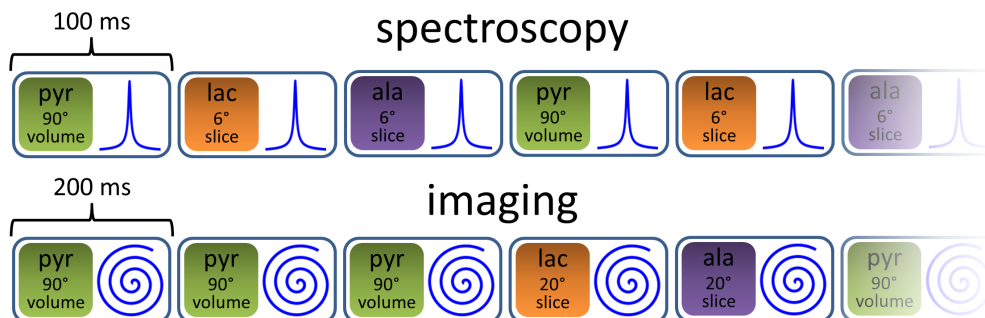
Figure 56: Acquisition schemes for the presented substrate saturation sequence. Top row: FID readout without gradient; bottom row: imaging acquisition with single-shot spiral gradient readout.

7.3.7 Measurement Protocol

For each animal, two separate injections were performed 1 h apart: the first without and the second with administration of 0.5 ml of a GdDO3A solution 16 s after the pyruvate injection at the supposed plateau of the lactate signal. The relative amount of GdDO3A compared to pyruvate was chosen to be 1:5 for 7 rats and 1:1 for one rat to test concentration effects. After 20 s, the pulse sequence described above was started. Spectroscopic data were acquired for 4 rats and imaging data for another 4 rats in a 14-18 mm slice including the tumour. In the time between the two injections, fast-recovery fast spin-echo (FRFSE) ^{1}H images with slice thickness of 3 mm were acquired in the centre of the ^{13}C tumour slice to provide anatomical reference.

7.3.8 Reconstruction

A 15 Hz Gaussian filter was applied along the readout dimension to both spectroscopy and imaging data. Fast Fourier transform (FFT) was applied to the spectroscopy data to reconstruct spectra. Spiral imaging data were phase corrected along the readout for the resonance frequency of the specific metabolite. Subsequently, a non-uniform fast Fourier transform (NUFFT) [112] was used to reconstruct spiral data onto a Cartesian grid.

Since in vivo acquisitions of hyperpolarised biomarkers typically suffer from low SNR compared to standard proton acquisitions, it is important to avoid the Rician bias [69]

from absolute value images or spectra when fitting the decay rates. Thus, the spectra were phase corrected and the peak value of the real valued spectrum was used for further evaluation. In this special case, the images feature the same structures with decreasing SNR; thus the mean phase from the first few images with sufficient SNR (where the noise is nearly Gaussian distributed) was taken to correct the whole image series. For the lactate imaging acquisitions, regions of interest (ROIs) were drawn manually to calculate the mean tumour signal. As alanine is not specific to the tumour tissue, ROIs were generated by taking each image voxel with a signal > 70 % of the maximum signal within the first image.

A monoexponential fit was applied to the decay curves of the metabolites starting 3 s after beginning the acquisition when pyruvate was completely saturated and the signal dynamics had reached equilibrium. Apparent cell transporter activity rates were calculated according to Equation 51. Furthermore, spatially resolved maps of the apparent lactate MCT transporter rate were obtained by applying the fit on each voxel with a signal > 30 % of the maximum signal within the first image.

7.4 Results

7.4.1 GdDO3A Relaxation Properties

The T_1 values measured in vitro are reported in Table 9. Compared to the coordinatively saturated Gd(HP-DO3A) complex (trade name: ProHance), GdDO3A could achieve an approximately 10-fold reduction of T_1 relaxation times for lactate in serum.

	Pyr [5 mM]	Lac [0.5 mM]	Ala [0.5 mM]
Gd-HP-DO3A [1 mM]		500 ± 50 ms	
GdDO3A [1 mM]	90 ± 10 ms	43 ± 5 ms	35 ± 5 ms
GdDO3A [0.1 mM]	800 ± 50 ms	400 ± 50ms	330 ± 30 ms

Table 9: T_1 measured at 14 T in serum for pyruvate (Pyr), lactate (Lac) and alanine (Ala) in the presence of Gd-HP-DO3A and GdDO3a. Data provided by Dr. Francesca Reineri.

7.4.2 In Vivo Hyperpolarisation Experiments

The fitted apparent efflux rates of lactate ($k_{L,int \to ext}$) and alanine ($k_{A,int \to ext}$) can be found in Table 10.

The mean value of $k_{L,int \to ext}$ from the spectroscopy acquisitions (rat 1-3) was 0.20 $\pm$ 0.05 s^{-1}, the mean value from the imaging acquisitions (rat 5-8) 0.18 $\pm$ 0.03 s^{-1}. For alanine, no significant difference in decay rates was found within the noise level (spectroscopy rat 1-3: 0.01 $\pm$ 0.01 s^{-1}, imaging rat 5-8: 0.02 $\pm$ 0.02 s^{-1}). Rat 4 with a pyruvate to Gd ratio of 1:1 shows a slightly elevated export rate for lactate (0.31 s^{-1}) whereas the alanine signal is unchanged again. To verify the effectiveness

rat	acquisition	conc. ratio Gd:Pyr	$k_{L,int \to ext}$ $[s^{-1}]$	$k_{A,int \to ext}$ $[s^{-1}]$
1	spectr.	1:5	0.16 ± 0.01	0.02 ± 0.01
2	spectr.	1:5	0.19 ± 0.04	0.00 ± 0.01
3	spectr.	1:5	0.25 ± 0.04	0.01 ± 0.01
4	spectr.	1:1	0.31 ± 0.07	0.02 ± 0.01
5	imaging	1:5	0.15 ± 0.04	0.02 ± 0.02
6	imaging	1:5	0.18 ± 0.01	0.02 ± 0.02
7	imaging	1:5	0.16 ± 0.05	0.03 ± 0.02
8	imaging	1:5	0.22 ± 0.03	-0.01 ± 0.03

Table 10: Results from in vivo experiments in Fischer F344 rats bearing a subcutaneous Mat BIII tumour in the neck region. Given are the mode of acquisition (spectroscopy or imaging), the concentration ratio of GdDO3A to pyruvate and the apparent transporter activity rates (lactate: $k_{L,int \to ext}$, alanine: $k_{A,int \to ext}$). Errors are propagated 95 % confident intervals.

of the pyruvate saturation pulse, the pyruvate spectroscopy signal was analysed for the first injection without relaxation agent. The remaining pyruvate magnetisation in the entire rat body was found to be 4 % ± 5 % at the beginning of the decay rate fit. The overlays of the ^{13}C metabolite maps with the anatomical proton images confirmed that most of the lactate signal in the slice stemmed from the tumour, whereas alanine was distributed mostly in the surrounding tissue (data not shown). The SNR of the lactate images was sufficient to derive spatially resolved maps of $k_{L,int \to ext}$ which showed homogeneous apparent transporter activity within the tumour area. Exemplary datasets for spectroscopy and imaging are presented in Figures 57 and 58, respectively.
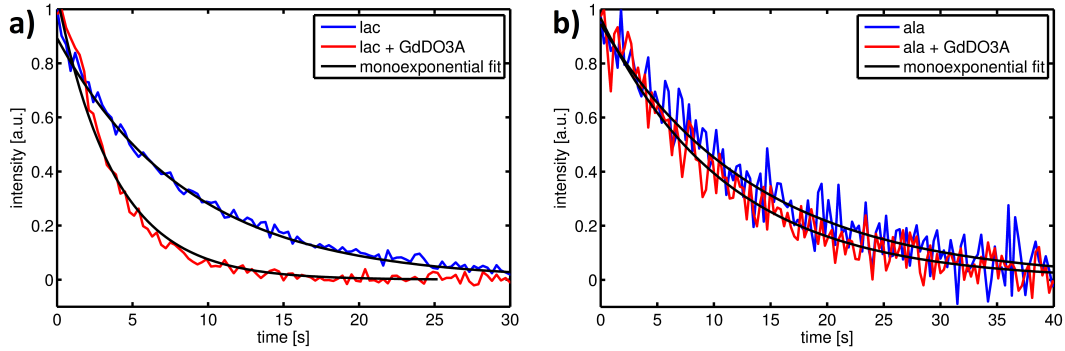
Figure 57: Representative dataset from rat 1 for spectroscopic acquisition. The plot shows metabolite decay without (blue) and with administration of GdDO3A (red) as well as the corresponding monoexponential fits (black) for lactate (a) and alanine (b). A significant difference in decay can be observed for lactate, indicating rapid lactate efflux.
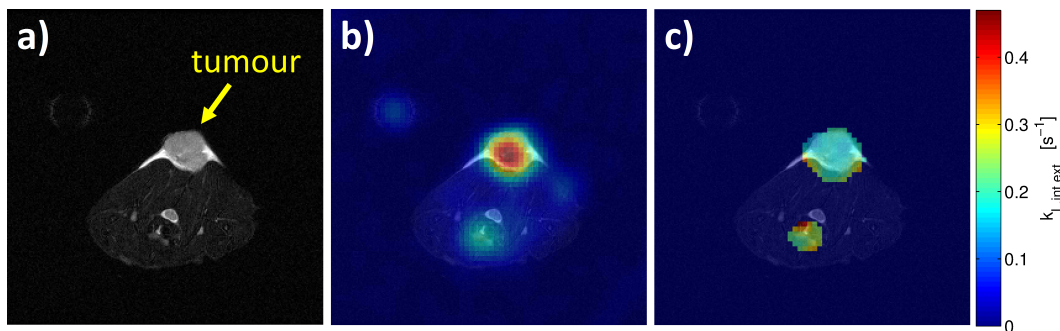
Figure 58: Representative dataset from rat 6 for imaging acquisition. a) FRFSE proton image for anatomical reference b) Lactate signal (sum of first three images) overlaid with a proton image c) Apparent MCT transporter map overlayed with a proton image (signal masked for > 30 % of the maximum).

7.4.3 Immunohistochemistry

Subcutaneous Mat BIII tumours exhibit a strong membranous MCT1 and a moderate membraneous MCT4 expression. An exemplary slice is shown in Figure 59.

(a) MCT1

(b) MCT4
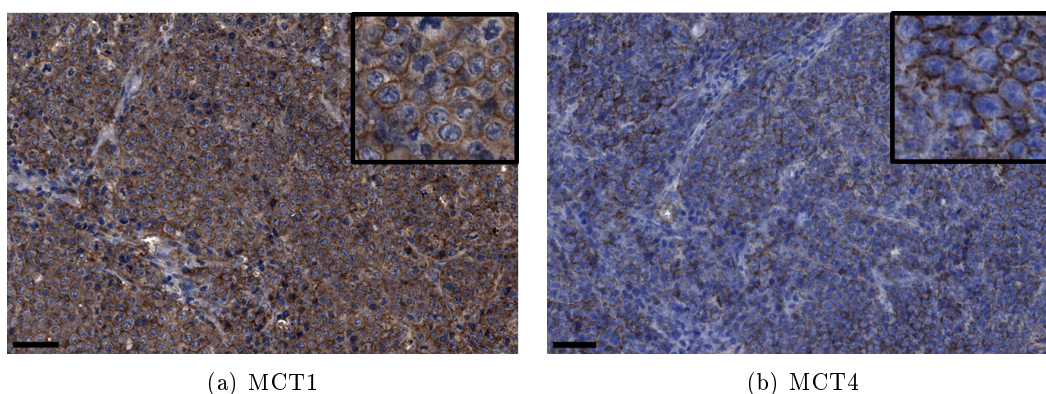
Figure 59: Immunohistochemistry to detect MCT1 and MCT4 expression in a slice from subcutaneous Mat BIII tumour. Bars: 50 μm. Figure provided by Dr. Katja Steiger.

7.5 Discussion and Conclusions

The relaxation rate measurements carried out in vitro (in plasma) revealed that the Gd-DO3A complex allows extremely fast relaxation of the magnetisation of pyruvate, lactate and alanine. For lactate, GdDO3A achieved to reduce the T_1 relaxation time by approximately a factor of 10 as compared to a coordinatively saturated Gd(HP-DO3A) complex (ProHance), even when the concentration of both the paramagnetic complex and the metabolite is lower than 1 mM. Furthermore, in a separate proton DCE study (see Figure 60), the GdDO3A concentration was found to rise quickly in the tumour within the time scale of a hyperpolarised ^{13}C acquisition. It is therefore a

92

promising candidate to create contrast between intra- and extracellular magnetisation for hyperpolarised pyruvate experiments.
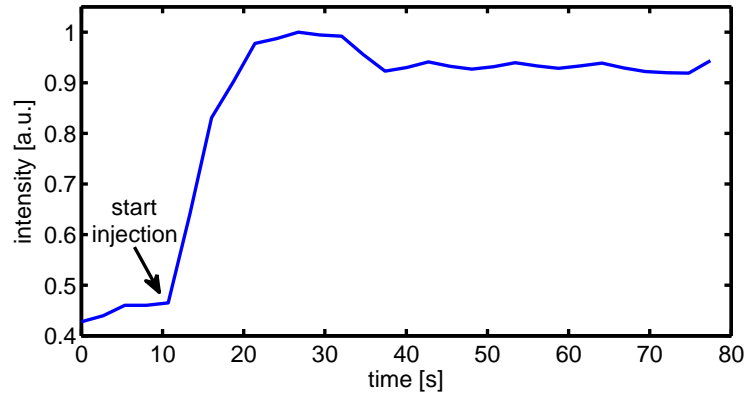
Figure 60: Signal intensity in a tumour region of interest during incoming bolus of GdDO3A. A time resolved imaging of contrast kinetics (TRICKS) sequence was used to acquire T_1-weighted proton images every 2.67 s (resolution 128 × 128 pixels, FOV 8 cm).

In vivo data from a preliminary study with GdDO3A conducted in healthy rats are shown in Figure 61. Significant alteration of signal kinetics can be observed for both lactate and alanine, which could be due to efflux from the cells or loss of hyperpolarised flux from pyruvate. Using standard NMR methods, this dilemma cannot be resolved as there are too many unknowns to fit the curves to the required 6 compartment model. Even if more information was available, the fit would most likely be error-prone due to the typically low SNR regime of hyperpolarised acquisitions. The proposed method elegantly reduces the problem to simply fitting the decay rates by completely eliminating the influence of pyruvate conversion.
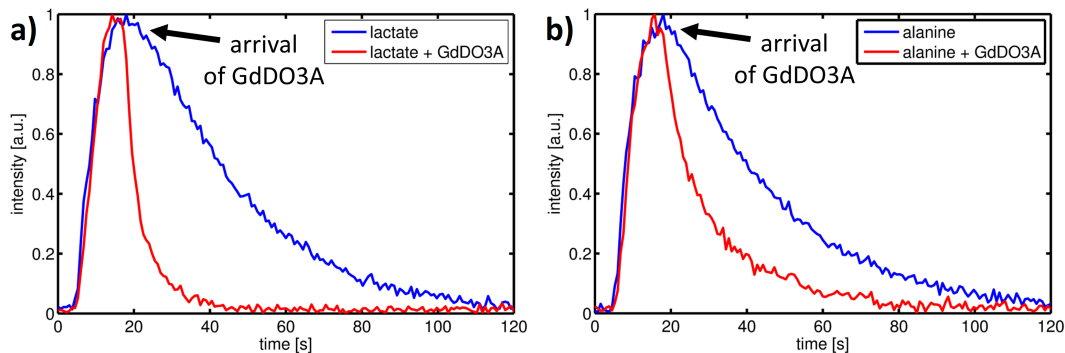
Figure 61: Representative dataset from a preliminary study without saturation pulse: Spectro-
scopic acquisitions of a kidney slice from a healthy rat after injection of hyperpolarised
[1-^{13}C]pyruvate. The plot shows the metabolic time curves without (blue) and with
administration of GdDO3A (red) for lactate (a) and alanine (b). A significant dif-
ference can be observed for both metabolites, which could be due to efflux or loss
of hyperpolarised flux from pyruvate. The proposed method with saturation pulse
allows resolution of this issue.

A significant difference of lactate decay was found in the presence of GdDO3A, which
indicates considerable lactate efflux in the tumour tissue. This is also consistent with
the immunohistochemical analysis, which shows a strong membranous MCT1 expression
and a moderate membranous MCT4 expression. These are two of the most important
transporters responsible for lactate transport. While MCT4 is the transporter believed
to be mainly responsible for the export of glycolysis-derived lactate occurring in hypoxic
tumours [200, 201], there is evidence that under certain circumstances, also MCT1 can
become a major pathway for lactate efflux [172].
For alanine, no significant difference in decay rates could be found, suggesting that alanine
excretion occurs on a much slower time scale. This is consistent with our assumptions,
since alanine is an amino acid and not transported by MCTs but by a range of other
transporter systems that require the co-transport of other amino acids [202]. As a non-
essential amino-acid, alanine mostly serves as an exchange substrate for the uptake of
essential amino acids in mammalian cells. Therefore, its efflux rate was expected to be at
least one order of magnitude lower than the values found for lactate [203]. These results
confirm the sensitivity of the method for detecting lactate transport out of the cell.
As there is no gold standard to compare the results to, the limitations of the described
technique must be thoroughly evaluated in further studies. In principle, the same chal-
lenges arise as for the apparent conversion rate constants describing the metabolic con-
version. As a result of relaxation, the hyperpolarised in vivo signal cannot be directly
related to absolute molecule concentrations. Also, the measurements may be complicated
by underlying biological processes such as perfusion, label exchange and other influences.
One important factor is the perfusion and accumulation of the GdDO3A agent; results
may be biased by insufficient concentration or slow inflow into the target tissue. This
is indicated by rat 4, which received a higher concentration of the GdDO3A compound,
resulting in elevated values of the decay. If quantitative proton T_1 maps and ^{13}C data

can be acquired in the same scan, as demonstrated in [189], the obtained concentration of GdDO3A may be used to improve accuracy and provide more information on the dynamics during the GdDO3A bolus. To increase the relaxation weighting, a higher concentration of GdDO3A should be used in future examinations if possible. Moreover, a real-time bolus tracking approach could be adapted to automatically detect the optimal time point for starting the acquisition at the peak of the lactate curve [105].

Furthermore, the influence of the intra- and extracellular pool sizes needs to be investigated. If there is a large extracellular pool, most of the signal may stem from the decay of this pool. Also, it is currently not possible to distinguish between net transport and label exchange between the intra- and extracellular pool. Regarding this issue, the pulse sequence could be modified to acquire spin echoes. This may allow better investigation of the extra- and intracellular compartment sizes of the metabolite signal due to varying T_2 relaxation time with and without GdDO3A administration. Another interesting approach could be to incorporate the GdDO3A complex into a liposome structure to target only intravascular hyperpolarisation. This may provide valuable complementary information on the distribution of metabolites between vascular, interstitial, and intracellular spaces.

For these reasons, tumour models with a different rate of lactate export have to be studied in order to determine whether the contrast provided by the proposed method is sufficient to distinguish between different tumour types or disease states.

As described in the introduction, MCT expression has a strong impact on tumour metabolism and development. Recently, it was shown by Keshari et al. [186] in vitro that hyperpolarised lactate efflux can be used to non-invasively assess the aggressiveness of different renal cell carcinoma phenotypes. The presented method might therefore allow for in vivo characterisation of tumour biology to choose appropriate treatment.

In conclusion, a method to measure cell membrane transporter activity in vivo using hyperpolarised biomarkers is presented. Significantly increased decay rates were found for lactate in rats with mammary carcinoma in the presence of GdDO3A, indicating rapid transport out of the cell. In addition to slice-selective spectra, spatially resolved maps of apparent membrane transporter activity could be obtained. This technique could allow for better understanding of tumour metabolism and progression; and could enable treatment response measurements for MCT-targeted cancer therapies. Moreover, the developed method may provide vital insights into the signal kinetics of hyperpolarised [1-^{13}C]pyruvate examinations.

8 Future Prospects of Magnetic Resonance Imaging with Hyperpolarised Biomarkers

At the time of writing, the hyperpolarised ^{13}C technology is entering a crucial phase. A large number of preclinical studies have been published, indicating the considerable potential of hyperpolarised biomarkers to study a wide variety of disease states. However, these animal studies have also revealed several technical and biological challenges.

Currently, this technology is being translated into clinical applications, and the first human trials with pyruvate have already begun [42]. On the technical side, the most prominent concern is the low signal-to-noise ratio; the signal in human patients is considerably lower than that in rats or mice as a result of dose limitations, pre-injection quality assurance processes, and slower perfusion. Therefore, the achievable spatial and temporal resolutions are severely limited by sensitivity. Compared to conventional proton magnetic resonance imaging (MRI), the physical constraints for hyperpolarised acquisitions are considerably stricter. The short-lived, non-renewable signal and the upper limits of the polarisation level do not offer many possibilities for signal gain.

Regarding biological factors, the signal is influenced by a wide variety of parameters, including perfusion, cellular uptake, enzymatic conversion, and label exchange, which cannot be separated by standard chemical shift imaging (CSI) protocols. It is therefore neccessary to determine whether the currently obtained data is of sufficient diagnostic value, or more complex acquisition schemes are required to resolve these ambiguities. Moreover, the in vivo lifetime of ^{13}C-based hyperpolarised biomarkers is too short for a large number of physiological processes. Therefore, new ways to increase relaxation times and preserve hyperpolarised magnetisation must be explored.

Compared to its closest competitor, positron emission tomography (PET) [29], dynamic nuclear polarisation (DNP) [5] offers the unique possibility to distinguish between different molecular configurations and, therefore, to study metabolic pathways, whereas PET can measure perfusion and accumulation only. Furthermore, DNP does not involve ionising radiation. On the other hand, ^{13}C biomarkers must be used in very high, unphysiological concentrations whereas PET can already detect much smaller quantities. Also, PET allows absolute quantification of tracer concentration in tissue, whereas the signal obtained from ^{13}C measurements is more or less arbitrary as a result of signal decay. ^{13}C biomarkers are short-lived, but they can be used to detect rapid metabolic processes in real-time. PET requires a longer period of acquisition but therefore, also averages biological variations. Regarding cost, it is difficult to predict the final numbers but, if DNP hardware and substrates are produced on a large scale, the cost will most likely be competitive in comparison to PET examinations.

Overall, DNP will most likely evolve to become a useful preclinical tool. However, its clinical use is yet to be determined, and many obstacles remain.

9 Conclusions

The goal of this work was to develop efficient acquisition strategies for magnetic resonance imaging with hyperpolarised biomarkers and to apply them to preclinical in vivo studies in order to validate their performance. Using advanced pulse sequence design and reconstruction methods, a broad spectrum of biomedical applications was examined.

First, an in-depth comparison of existing pulse sequences for hyperpolarised agents was conducted in order to reveal their strengths and weaknesses and to find general guidelines for pulse sequence design in this field. The investigated acquisition strategies differed mainly in their encoding efficiency, gradient demand, and artefact behaviour. Although many different pulse sequences for imaging hyperpolarised compounds emerged over the past decade, a systematic comparison had not been conducted previously. Based on the findings of this analysis, optimal imaging strategies for a specific application can be developed. Furthermore, an extensive and well-documented code framework for simulation and reconstruction of chemical shift imaging acquisitions was created in Matlab and released to the public. This framework has considerably facilitated the workflow for subsequent projects.

Based on the expertise in pulse sequence design and programming acquired previously, a fully automatic bolus tracking sequence for hyperpolarised biomarkers was developed. When active, it constantly evaluates the hyperpolarised signal in real-time to find the predefined point on the bolus curve where to start the image acquisition. Compared to conventional imaging strategies, the bolus tracking sequence reduces artefacts as a result of signal change, allows to use the hyperpolarised magnetisation more efficiently, and ensures more reliable and consistent evaluation of metabolic activity. Moreover, this technique could be developed further into a routine assessment protocol for clinical applications that provides reproducible results and does not rely on a human operator. Real-time data processing offers the possibility for optimal data sampling of the evolving hyperpolarised signals and should therefore be pursued further.

In another effort to increase the efficiency of hyperpolarised imaging methods, a spiral chemical shift imaging sequence for cardiac imaging in pigs using hyperpolarised pyruvate was designed. The potential application of parallel imaging reconstructions was explored by artificially undersampling the in vivo data; up to 4-fold acceleration could be achieved. While the fully sampled sequence delivered good results, only little benefit related to the speed-up provided by parallel imaging was found for the given scenario. Nevertheless, this result is of importance, as the question of when parallel imaging is beneficial for hyperpolarised acquisitions is still open. While some groups have reported nominal advantages for inefficient Cartesian sampling schemes with high encoding demands, this study has demonstrated that, when an encoding-efficient non-Cartesian chemical shift imaging sequence is employed, the benefits of parallel imaging are considerably limited.

A further new application that requires efficient acquisition strategies is hyperpolarised ^{15}N imaging. A pulse sequence for the first in vivo tests of a novel hyperpolarised perfusion marker with an especially long T_1 relaxation time, α-trideuteromethyl[^{15}N]glutamine, was implemented. A single-shot spiral readout in combination with a variable repetition

time was chosen in order to image the incoming hyperpolarised bolus first at a high temporal rate and then monitor uptake at a greater timescale. The glutamine compound was directly compared to hyperpolarised ^{13}C-labelled urea in healthy rats. Whereas the urea signal in a kidney slice had decayed after approximately 90 s, the signal of the glutamine derivative was still detectable after more than 5 minutes, and was strongly localised to renal tissue. Therefore, this compound shows great promise for studying kidney function. To date, the majority of research on hyperpolarised biomarkers has focused on ^{13}C-based compounds with in vivo relaxation times of below one minute. This study emphasises the possibility of very long-lived hyperpolarised compounds based on ^{15}N and could further the development of many other potential applications.

Finally, a novel pulse sequence using a pyruvate saturation pulse in combination with a tailored Gadolinium-based contrast agent for the measurement of metabolite efflux from cells was invented. Indications of high lactate efflux rates were found in rats with mammary carcinoma after injection of hyperpolarised [1-^{13}C]pyruvate. Alanine however was found to remain mostly intracellular during the measurement. This innovative method may facilitate improved understanding of tumour metabolism and progression by detecting cell membrane transporter activity for hyperpolarised metabolites.

In summary, a wide range of aspects of hyperpolarised in vivo imaging has been explored, and new methods to improve the diagnostic value of hyperpolarised examinations have been presented. These contributions are highly relevant for the application of the DNP technique in preclinical studies, and also for its ongoing translation to clinical applications.

Bibliography

[1] P. C. Lauterbur, "Image Formation by Induced Local Interactions: Examples Employing Nuclear Magnetic Resonance," *Nature*, vol. 242, pp. 190–191, 1973.

[2] P. Mansfield and P. K. Grannell, "NMR 'diffraction' in solids?," *Journal of Physics C: Solid State Physics*, vol. 6, no. 22, pp. L422–L426, 1973.

[3] R. B. Moon and J. H. Richards, "Determination of intracellular ph by 31p magnetic resonance," *Journal of Biological Chemistry*, vol. 248, no. 20, pp. 7276–7278, 1973.

[4] D. I. Hoult, S. J. W. Busby, D. G. Gadian, G. K. Radda, R. E. Richards, and P. J. Seeley, "Observation of tissue metabolites using 31p nuclear magnetic resonance," *Nature*, vol. 252, pp. 285–287, 1974.

[5] J. H. Ardenkjaer-Larsen, B. Fridlund, A. Gram, G. Hansson, L. Hansson, M. H. Lerche, R. Servin, M. Thaning, and K. Golman, "Increase in signal-to-noise ratio of $> 10,000$ times in liquid-state nmr," *Proceedings of the National Academy of Sciences of the United States of America*, vol. 100, no. 18, pp. 10158–10163, 2003.

[6] F. A. Gallagher, M. I. Kettunen, and K. M. Brindle, "Biomedical applications of hyperpolarized 13c magnetic resonance imaging," *Progress in Nuclear Magnetic Resonance Spectroscopy*, vol. 55, no. 4, pp. 285–295, 2009.

[7] S. E. Day, M. I. Kettunen, F. A. Gallagher, D. E. Hu, M. Lerche, J. Wolber, K. Golman, J. H. Ardenkjaer-Larsen, and K. M. Brindle, "Detecting tumor response to treatment using hyperpolarized 13c magnetic resonance imaging and spectroscopy," *Nature Medicine*, vol. 13, no. 11, pp. 1382–1387, 2007.

[8] K. Golman, R. I. Zandt, and M. Thaning, "Real-time metabolic imaging," *Proceedings of the National Academy of Sciences of the United States of America*, vol. 103, no. 30, pp. 11270–11275, 2006.

[9] K. Golman, R. I. Zandt, M. Lerche, R. Pehrson, and J. H. Ardenkjaer-Larsen, "Metabolic imaging by hyperpolarized c-13 magnetic resonance imaging for in vivo tumor diagnosis," *Cancer Research*, vol. 66, no. 22, pp. 10855–10860, 2006.

[10] R. E. Hurd, Y. F. Yen, D. Mayer, A. Chen, D. Wilson, S. Kohler, R. Bok, D. Vigneron, J. Kurhanewicz, J. Tropp, D. Spielman, and A. Pfefferbaum, "Metabolic imaging in the anesthetized rat brain using hyperpolarized [1-13c] pyruvate and [1-13c] ethyl pyruvate," *Magnetic Resonance in Medicine*, vol. 63, no. 5, pp. 1137–1143, 2010.

[11] S. J. Kohler, Y. Yen, J. Wolber, A. P. Chen, M. J. Albers, R. Bok, V. Zhang, J. Tropp, S. Nelson, D. B. Vigneron, J. Kurhanewicz, and R. E. Hurd, "In vivo 13 carbon metabolic imaging at 3t with hyperpolarized 13c-1-pyruvate," *Magnetic Resonance in Medicine*, vol. 58, no. 1, pp. 65–69, 2007.

[12] J. D. MacKenzie, Y. F. Yen, D. Mayer, J. S. Tropp, R. E. Hurd, and D. M. Spielman, "Detection of inflammatory arthritis by using hyperpolarized 13c-pyruvate with mr imaging and spectroscopy," *Radiology*, vol. 259, no. 2, pp. 414–420, 2011.

[13] Y. F. Yen, S. J. Kohler, A. P. Chen, J. Tropp, R. Bok, J. Wolber, M. J. Albers, K. A. Gram, M. L. Zierhut, I. Park, V. Zhang, S. Hu, S. J. Nelson, D. B. Vigneron, J. Kurhanewicz, H. A. Dirven, and R. E. Hurd, "Imaging considerations for in vivo 13c metabolic mapping using hyperpolarized 13c-pyruvate," *Magnetic Resonance in Medicine*, vol. 62, no. 1, pp. 1–10, 2009.

[14] A. P. Chen, M. J. Albers, C. H. Cunningham, S. J. Kohler, Y. F. Yen, R. E. Hurd, J. Tropp, R. Bok, J. M. Pauly, S. J. Nelson, J. Kurhanewicz, and D. B. Vigneron, "Hyperpolarized c-13 spectroscopic imaging of the tramp mouse at 3t-initial experience," *Magnetic Resonance in Medicine*, vol. 58, no. 6, pp. 1099–1106, 2007.

[15] C. H. Cunningham, A. P. Chen, M. J. Albers, J. Kurhanewicz, R. E. Hurd, Y. F. Yen, J. M. Pauly, S. J. Nelson, and D. B. Vigneron, "Double spin-echo sequence for rapid spectroscopic imaging of hyperpolarized 13c," *Journal of Magnetic Resonance*, vol. 187, no. 2, pp. 357–362, 2007.

[16] P. E. Larson, R. Bok, A. B. Kerr, M. Lustig, S. Hu, A. P. Chen, S. J. Nelson, J. M. Pauly, J. Kurhanewicz, and D. B. Vigneron, "Investigation of tumor hyperpolarized [1-13c]-pyruvate dynamics using time-resolved multiband rf excitation echo-planar mrsi," *Magnetic Resonance in Medicine*, vol. 63, no. 3, pp. 582–591, 2010.

[17] I. Park, P. E. Larson, J. L. Tropp, L. Carvajal, G. Reed, R. Bok, F. Robb, J. Bringas, A. Kells, P. Pivirotto, K. Bankiewicz, D. B. Vigneron, and S. J. Nelson, "Dynamic hyperpolarized carbon-13 mr metabolic imaging of nonhuman primate brain," *Magnetic Resonance in Medicine*, vol. 71, no. 1, pp. 19–25, 2014.

[18] F. Frijia, F. Wiesinger, M. F. Santarelli, V. Positano, J. H. Ardenkjaer-Larsen, R. Schulte, L. Menichetti, G. Giovannetti, G. Bianchi, and G. Aquaro, "Detection of 3d cardiac metabolism after injection of hyperpolarized [1-13c] pyruvate," *Journal of Cardiovascular Magnetic Resonance*, vol. 13, no. Suppl 1, p. M2, 2011.

[19] F. Wiesinger, E. Weidl, M. I. Menzel, M. A. Janich, O. Khegai, S. J. Glaser, A. Haase, M. Schwaiger, and R. F. Schulte, "Ideal spiral csi for dynamic metabolic mr imaging of hyperpolarized [1-13c]pyruvate," *Magnetic Resonance in Medicine*, vol. 68, no. 1, pp. 8–16, 2012.

[20] A. Flori, F. Frijia, V. Lionetti, J. H. Ardenkjaer-Larsen, V. Positano, G. Giovannetti, R. F. Schulte, F. Wiesinger, F. A. Recchia, L. Landini, M. F. Santarelli, M. Lombardi, and L. Menichetti, "Dnp methods for cardiac metabolic imaging with hyperpolarized [1-13c]pyruvate large dose injection in pigs," *Applied Magnetic Resonance*, vol. 43, no. 1-2, pp. 299–310, 2012.

[21] M. I. Menzel, E. V. Farrell, M. A. Janich, O. Khegai, F. Wiesinger, S. Nekolla, A. M. Otto, A. Haase, R. F. Schulte, and M. Schwaiger, "Multimodal assessment of in vivo metabolism with hyperpolarized [1-13c]mr spectroscopy and 18f-fdg pet imaging in hepatocellular carcinoma tumor-bearing rats," *Journal of Nuclear Medicine*, vol. 54, no. 7, pp. 1113–1119, 2013.

[22] D. Mayer, Y. S. Levin, R. E. Hurd, G. H. Glover, and D. M. Spielman, "Fast metabolic imaging of systems with sparse spectra: application for hyperpolarized 13c imaging," *Magnetic Resonance in Medicine*, vol. 56, no. 4, pp. 932–937, 2006.

[23] Y. S. Levin, D. Mayer, Y. F. Yen, R. E. Hurd, and D. M. Spielman, "Optimization of fast spiral chemical shift imaging using least squares reconstruction: application for hyperpolarized (13)c metabolic imaging," *Magnetic Resonance in Medicine*, vol. 58, no. 2, pp. 245–252, 2007.

[24] D. Mayer, Y. F. Yen, J. Tropp, A. Pfefferbaum, R. E. Hurd, and D. M. Spielman, "Application of subsecond spiral chemical shift imaging to real-time multislice metabolic imaging of the rat in vivo after injection of hyperpolarized 13c1-pyruvate," *Magnetic Resonance in Medicine*, vol. 62, no. 3, pp. 557–564, 2009.

[25] D. Mayer, Y. F. Yen, Y. S. Levin, J. Tropp, A. Pfefferbaum, R. E. Hurd, and D. M. Spielman, "In vivo application of sub-second spiral chemical shift imaging (csi) to hyperpolarized 13c metabolic imaging: comparison with phase-encoded csi," *Journal of Magnetic Resonance*, vol. 204, no. 2, pp. 340–345, 2010.

[26] D. Mayer, Y. F. Yen, A. Takahashi, S. Josan, J. Tropp, B. K. Rutt, R. E. Hurd, D. M. Spielman, and A. Pfefferbaum, "Dynamic and high-resolution metabolic imaging of hyperpolarized [1-13c]-pyruvate in the rat brain using a high-performance gradient insert," *Magnetic Resonance in Medicine*, vol. 65, no. 5, pp. 1228–1233, 2011.

[27] J. M. Park, S. Josan, T. Jang, M. Merchant, Y. F. Yen, R. E. Hurd, L. Recht, D. M. Spielman, and D. Mayer, "Metabolite kinetics in c6 rat glioma model using magnetic resonance spectroscopic imaging of hyperpolarized [1-(13)c]pyruvate," *Magnetic Resonance in Medicine*, vol. 68, no. 6, pp. 1886–1893, 2012.

[28] E. Chiavazza, A. Viale, M. Karlsson, and S. Aime, "15n-permethylated amino acids as efficient probes for mri-dnp applications," *Contrast Media & Molecular Imaging*, vol. 8, no. 5, pp. 417–421, 2013.

[29] D. Bailey, D. Townsend, P. Valk, and M. Maisey, *Positron Emission Tomography: Basic Sciences*. Springer London, 2004.

[30] P. Zeeman, "The Effect of Magnetisation on the Nature of Light Emitted by a Substance," *Nature*, vol. 55, p. 347, 1897.

[31] I. I. Rabi, J. R. Zacharias, S. Millman, and P. Kusch, "A new method of measuring nuclear magnetic moment," *Physical Review*, vol. 53, pp. 318–318, Feb 1938.

[32] E. M. Purcell, H. C. Torrey, and R. V. Pound, "Resonance absorption by nuclear magnetic moments in a solid," *Physical Review*, vol. 69, pp. 37–38, 1946.

[33] F. Bloch, W. W. Hansen, and M. Packard, "Nuclear induction," *Physical Review*, vol. 69, p. 127, 1946.

[34] W. G. Proctor and F. C. Yu, "The dependence of a nuclear magnetic resonance frequency upon chemical compound," *Physical Review*, vol. 77, pp. 717–717, 1950.

[35] W. C. Dickinson, "Dependence of the f^{19} nuclear resonance position on chemical compound," *Physical Review*, vol. 77, pp. 736–737, 1950.

[36] R. R. Ernst and W. A. Anderson, "Application of fourier transform spectroscopy to magnetic resonance," *Review of Scientific Instruments*, vol. 37, no. 1, pp. 93–102, 1966.

[37] M. A. Bouchiat, T. R. Carver, and C. M. Varnum, "Nuclear Polarization in He^3 Gas Induced by Optical Pumping and Dipolar Exchange," *Physical Review Letters*, vol. 5, pp. 373–375, 1960.

[38] G. L. Closs, "Mechanism explaining nuclear spin polarizations in radical combination reactions," *Journal of the American Chemical Society*, vol. 91, no. 16, pp. 4552–4554, 1969.

[39] C. R. Bowers and D. P. Weitekamp, "Parahydrogen and synthesis allow dramatically enhanced nuclear alignment," *Journal of the American Chemical Society*, vol. 109, no. 18, pp. 5541–5542, 1987.

[40] A. W. Overhauser, "Polarization of nuclei in metals," *Physical Review*, vol. 92, pp. 411–415, 1953.

[41] M. E. Merritt, C. Harrison, C. Storey, A. D. Sherry, and C. R. Malloy, "Inhibition of carbohydrate oxidation during the first minute of reperfusion after brief ischemia: Nmr detection of hyperpolarized 13co2 and h13co3," *Magnetic Resonance in Medicine*, vol. 60, no. 5, pp. 1029–1036, 2008.

[42] S. J. Nelson, J. Kurhanewicz, D. B. Vigneron, P. E. Larson, A. L. Harzstark, M. Ferrone, M. van Criekinge, J. W. Chang, R. Bok, I. Park, G. Reed, L. Carvajal, E. J. Small, P. Munster, V. K. Weinberg, J. H. Ardenkjaer-Larsen, A. P. Chen, R. E. Hurd, L. I. Odegardstuen, F. J. Robb, J. Tropp, and J. A. Murray, "Metabolic imaging of patients with prostate cancer using hyperpolarized [1-(1)(3)c]pyruvate," *Science Translational Medicine*, vol. 5, no. 198, p. 198ra108, 2013.

[43] M. H. Levitt, *Spin Dynamics: Basics of Nuclear Magnetic Resonance*. John Wiley and Sons, 2008.

[44] M. Berglund and M. E. Wieser, "Isotopic compositions of the elements 2009 (IUPAC Technical Report)," *Pure and Applied Chemistry*, vol. 83, no. 2, pp. 397–410, 2011.

[45] R. de Graaf, *In Vivo NMR Spectroscopy: Principles and Techniques*. John Wiley and Sons, 2007.

[46] D. M. Wilson, K. R. Keshari, P. E. Larson, A. P. Chen, S. Hu, M. V. Criekinge, R. Bok, S. J. Nelson, J. M. Macdonald, D. B. Vigneron, and J. Kurhanewicz, "Multi-compound polarization by {DNP} allows simultaneous assessment of multiple enzymatic activities in vivo," *Journal of Magnetic Resonance*, vol. 205, no. 1, pp. 141 – 147, 2010.

[47] A. Oppelt, *Imaging Systems for Medical Diagnostics*. Publicis Publishing, 2005.

[48] T. M. Peters and J. Williams, *The Fourier Transform in Biomedical Engineering*. Birkhaeuser Boston, 1998.

[49] D. B. Twieg, "The k-trajectory formulation of the NMR imaging process with applications in analysis and synthesis of imaging methods," *Medical Physics*, vol. 10, pp. 610–621, 1983.

[50] C. E. Shannon, "Communication in the presence of noise," *Proceedings of the Institute of Radio Engineers*, vol. 37, pp. 10–21, 1949.

[51] J. Pauly, D. Nishimura, and A. Macovski, "A k-space analysis of small-tip-angle excitation," *Journal of Magnetic Resonance*, vol. 81, no. 1, pp. 43–56, 1989.

[52] C. H. Meyer, J. M. Pauly, A. Macovskiand, and D. G. Nishimura, "Simultaneous spatial and spectral selective excitation," *Magnetic Resonance in Medicine*, vol. 15, no. 2, pp. 287–304, 1990.

[53] R. F. Schulte and F. Wiesinger, "Direct design of 2d {RF} pulses using matrix inversion," *Journal of Magnetic Resonance*, vol. 235, pp. 115–120, 2013.

[54] W. Block, J. Pauly, A. Kerr, and D. Nishimura, "Consistent fat suppression with compensated spectral-spatial pulses," *Magnetic Resonance in Medicine*, vol. 38, no. 2, pp. 198–206, 1997.

[55] C. H. Cunningham, A. P. Chen, M. Lustig, B. A. Hargreaves, J. Lupo, D. Xu, J. Kurhanewicz, R. E. Hurd, J. M. Pauly, S. J. Nelson, and D. B. Vigneron, "Pulse sequence for dynamic volumetric imaging of hyperpolarized metabolic products," *Journal of Magnetic Resonance*, vol. 193, no. 1, pp. 139–146, 2008.

[56] A. Z. Lau, A. P. Chen, R. E. Hurd, and C. H. Cunningham, "Spectral-spatial excitation for rapid imaging of dnp compounds," *NMR in Biomedicine*, vol. 24, no. 8, pp. 988–996, 2011.

[57] R. F. Schulte, J. I. Sperl, E. Weidl, M. I. Menzel, M. A. Janich, O. Khegai, M. Durst, J. H. Ardenkjaer-Larsen, S. J. Glaser, A. Haase, M. Schwaiger, and F. Wiesinger, "Saturation-recovery metabolic-exchange rate imaging with hyperpolarized [1-13c] pyruvate using spectral-spatial excitation," *Magnetic Resonance in Medicine*, vol. 69, no. 5, pp. 1209–1216, 2013.

[58] M. A. Bernstein, K. F. King, and X. J. Zhou, *Handbook of MRI Pulse Sequences.* Elsevier Academic Press, 2004.

[59] E. L. Hahn, "Spin echoes," *Physical Review*, vol. 80, pp. 580–594, 1950.

[60] M. Durst, *Fast Spectroscopic Magnetic Resonance Imaging of Hyperpolarised 13C with Spiral Acquisition Schemes.* Diplomarbeit, Technische Universität München, 2011.

[61] A. Haase, J. Frahm, D. Matthaei, W. Haenicke, and K.-D. Merboldt, "FLASH Imaging. Rapid NMR Imaging Using Low Flip-Angle Pulses," *Journal of Magnetic Resonance*, vol. 67, pp. 258–266, 1986.

[62] M. Blaimer, F. Breuer, M. Mueller, R. M. Heidemann, M. A. Griswold, and P. M. Jakob, "SMASH, SENSE, PILS, GRAPPA - How to Choose the Optimal Method," *Topics in Magnetic Resonance Imaging*, vol. 15, no. 4, pp. 223–236, 2004.

[63] A. Deshmane, V. Gulani, M. A. Griswold, and N. Seiberlich, "Parallel mr imaging," *Journal of Magnetic Resonance Imaging*, vol. 36, no. 1, pp. 55–72, 2012.

[64] K. P. Pruessmann, M. Weiger, M. B. Scheidegger, and P. Boesiger, "SENSE: Sensitivity Encoding for Fast MRI," *Magnetic Resonance in Medicine*, vol. 42, no. 5, pp. 952–962, 1999.

[65] M. Lustig and J. M. Pauly, "SPIRiT: Iterative self-consistent parallel imaging reconstruction from arbitrary k-space," *Magnetic Resonance in Medicine*, vol. 64, no. 2, pp. 457–471, 2010.

[66] P. M. Jakob, M. A. Griswold, R. R. Edelman, and D. K. Sodickson, "Auto-smash: a self-calibrating technique for smash imaging. simultaneous acquisition of spatial harmonics," *MAGMA*, vol. 7, no. 1, pp. 42–54, 1998.

[67] M. A. Griswold, P. M. Jakob, R. M. Heidemann, M. Nittka, V. Jellus, J. Wang, B. Kiefer, and A. Haase, "Generalized Autocalibrating Partially Parallel Acquisitions (GRAPPA)," *Magnetic Resonance in Medicine*, vol. 47, no. 6, pp. 1202–1210, 2002.

[68] L. A. Shepp and B. F. Logan, "The fourier reconstruction of a head section," *Nuclear Science, IEEE Transactions on*, vol. 21, no. 3, pp. 21–43, 1974.

[69] H. Gudbjartsson and S. Patz, "The rician distribution of noisy mri data," *Magnetic Resonance in Medicine*, vol. 34, no. 6, pp. 910–914, 1995.

[70] E. M. Haacke, R. W. Brown, M. R. Thompson, and R. Venkatesan, *Magnetic Resonance Imaging: Physical Principles and Sequence Design.* Wiley, 1999.

[71] K. Nagashima, "Optimum pulse flip angles for multi-scan acquisition of hyperpolarized nmr and mri," *Journal of Magnetic Resonance*, vol. 190, no. 2, pp. 183–188, 2008.

106

[72] R. N. Bracewell and R. Bracewell, *The Fourier transform and its applications*, vol. 31999. McGraw-Hill New York, 1986.

[73] C. B. Ahn, J. H. Kim, and Z. H. Cho, "High-speed spiral-scan echo planar nmr imaging," *Medical Imaging, IEEE Transactions on*, vol. 5, no. 1, pp. 2–7, 1986.

[74] B. M. Delattre, R. M. Heidemann, L. A. Crowe, J.-P. Vallee, and J.-N. Hyacinthe, "Spiral demystified," *Magnetic Resonance Imaging*, vol. 28, no. 6, pp. 862–881, 2010.

[75] C. M. Lai and P. C. Lauterbur, "True three-dimensional image reconstruction by nuclear magnetic resonance zeugmatography," *Physics in Medicine and Biology*, vol. 26, no. 5, p. 851, 1981.

[76] G. H. Glover and J. M. Pauly, "Projection reconstruction techniques for reduction of motion effects in mri," *Magnetic Resonance in Medicine*, vol. 28, no. 2, pp. 275–289, 1992.

[77] R. D. Hoge, R. K. Kwan, and G. B. Pike, "Density compensation functions for spiral mri," *Magnetic Resonance in Medicine*, vol. 38, no. 1, pp. 117–128, 1997.

[78] J. O'Sullivan, "A fast sinc function gridding algorithm for fourier inversion in computer tomography," *Medical Imaging, IEEE Transactions on*, vol. 4, no. 4, pp. 200–207, 1985.

[79] J. Jackson, C. Meyer, D. Nishimura, and A. Macovski, "Selection of a convolution function for fourier inversion using gridding [computerised tomography application]," *Medical Imaging, IEEE Transactions on*, vol. 10, no. 3, pp. 473–478, 1991.

[80] J. G. Pipe and J. L. Duerk, "Analytical resolution and noise characteristics of linearly reconstructed magnetic resonance data with arbitrary k-space sampling," *Magnetic Resonance in Medicine*, vol. 34, no. 2, pp. 170–178, 1995.

[81] S. Aime, M. Fasano, and E. Terreno, "Lanthanide(iii) chelates for nmr biomedical applications," *Chem. Soc. Rev.*, vol. 27, pp. 19–29, 1998.

[82] P. Caravan, J. J. Ellison, T. J. McMurry, and R. B. Lauffer, "Gadolinium(iii) chelates as mri contrast agents: Structure, dynamics, and applications," *Chemical Reviews*, vol. 99, no. 9, pp. 2293–2352, 1999.

[83] L. T. Kuhn, *Hyperpolarization Methods in NMR Spectroscopy*. Springer, 2013.

[84] J. H. Ardenkjaer-Larsen, "13C Hyperpolarization: Imaging of Agents Pre-polarized by the DNP-NMR Method," in *ISMRM presentation*, 2005.

[85] O. Warburg, "On the origin of cancer cells," *Science*, vol. 123, no. 3191, pp. 309–314, 1956.

[86] O. Warburg, F. Wind, and E. Negelein, "Uber den Stoffwechsel von Tumouren im Korper," *Klinische Wochenschrift*, vol. 5, pp. 829–832, 1926.

[87] M. J. Albers, R. Bok, A. P. Chen, C. H. Cunningham, M. L. Zierhut, V. Y. Zhang, S. J. Kohler, J. Tropp, R. E. Hurd, Y.-F. Yen, S. J. Nelson, D. B. Vigneron, and J. Kurhanewicz, "Hyperpolarized 13c lactate, pyruvate, and alanine: Noninvasive biomarkers for prostate cancer detection and grading," *Cancer Research*, vol. 68, no. 20, pp. 8607–8615, 2008.

[88] K. M. Brindle, S. E. Bohndiek, F. A. Gallagher, and M. I. Kettunen, "Tumor imaging using hyperpolarized 13c magnetic resonance spectroscopy," *Magnetic Resonance in Medicine*, vol. 66, no. 2, pp. 505–519, 2011.

[89] S. E. Day, M. I. Kettunen, M. K. Cherukuri, J. B. Mitchell, M. J. Lizak, H. D. Morris, S. Matsumoto, A. P. Koretsky, and K. M. Brindle, "Detecting response of rat c6 glioma tumors to radiotherapy using hyperpolarized [1- 13c]pyruvate and 13c magnetic resonance spectroscopic imaging," *Magnetic Resonance in Medicine*, vol. 65, no. 2, pp. 557–63, 2011.

[90] J. M. Park, L. D. Recht, S. Josan, M. Merchant, T. Jang, Y. F. Yen, R. E. Hurd, D. M. Spielman, and D. Mayer, "Metabolic response of glioma to dichloroacetate measured in vivo by hyperpolarized (13)c magnetic resonance spectroscopic imaging," *Neuro Oncol*, vol. 15, no. 4, pp. 433–41, 2013.

[91] M. E. Merritt, C. Harrison, C. Storey, F. M. Jeffrey, A. D. Sherry, and C. R. Malloy, "Hyperpolarized 13c allows a direct measure of flux through a single enzyme-catalyzed step by nmr," *Proceedings of the National Academy of Sciences of the United States of America*, vol. 104, no. 50, pp. 19773–19777, 2007.

[92] K. Golman, J. S. Petersson, P. Magnusson, E. Johansson, P. Akeson, C. M. Chai, G. Hansson, and S. Mansson, "Cardiac metabolism measured noninvasively by hyperpolarized 13c mri," *Magnetic Resonance in Medicine*, vol. 59, no. 5, pp. 1005–1013, 2008.

[93] M. A. Schroeder, L. E. Cochlin, L. C. Heather, K. Clarke, G. K. Radda, and D. J. Tyler, "In vivo assessment of pyruvate dehydrogenase flux in the heart using hyperpolarized carbon-13 magnetic resonance," *Proceedings of the National Academy of Sciences of the United States of America*, vol. 105, no. 33, pp. 12051–12056, 2008.

[94] A. Z. Lau, A. P. Chen, N. R. Ghugre, V. Ramanan, W. W. Lam, K. A. Connelly, G. A. Wright, and C. H. Cunningham, "Rapid multislice imaging of hyperpolarized 13c pyruvate and bicarbonate in the heart," *Magnetic Resonance in Medicine*, vol. 64, no. 5, pp. 1323–1331, 2010.

[95] L. Menichetti, F. Frijia, A. Flori, F. Wiesinger, V. Lionetti, G. Giovannetti, G. D. Aquaro, F. A. Recchia, J. H. Ardenkjaer-Larsen, M. F. Santarelli, and M. Lombardi, "Assessment of real-time myocardial uptake and enzymatic conversion of

hyperpolarized [1-(1)(3)c]pyruvate in pigs using slice selective magnetic resonance spectroscopy," *Contrast Media & Molecular Imaging*, vol. 7, no. 1, pp. 85–94, 2012.

[96] C. von Morze, P. E. Larson, S. Hu, K. Keshari, D. M. Wilson, J. H. Ardenkjaer-Larsen, A. Goga, R. Bok, J. Kurhanewicz, and D. B. Vigneron, "Imaging of blood flow using hyperpolarized [(13)c]urea in preclinical cancer models," *Journal of Magnetic Resonance Imaging*, vol. 33, no. 3, pp. 692–697, 2011.

[97] C. von Morze, R. A. Bok, G. D. Reed, J. H. Ardenkjaer-Larsen, J. Kurhanewicz, and D. B. Vigneron, "Simultaneous multiagent hyperpolarized (13)c perfusion imaging," *Magnetic Resonance in Medicine*, vol. 72, no. 6, pp. 1599–1609, 2013.

[98] E. Chiavazza, E. Kubala, C. V. Gringeri, S. Duwel, M. Durst, R. F. Schulte, and M. I. Menzel, "Earth's magnetic field enabled scalar coupling relaxation of 13c nuclei bound to fast-relaxing quadrupolar 14n in amide groups," *Journal of Magnetic Resonance*, vol. 227, pp. 35–38, 2013.

[99] E. Chiavazza, *New Probes for Molecular Imaging*. Phd thesis, University of Turin, 2012.

[100] M. Durst, U. Koellisch, A. Frank, G. Rancan, C. V. Gringeri, V. Karas, F. Wiesinger, M. I. Menzel, M. Schwaiger, A. Haase, and R. F. Schulte, "Comparison of acquisition schemes for hyperpolarised 13c imaging," *NMR in Biomedicine*, vol. 28, no. 6, pp. 715–725, 2015.

[101] S. J. Nelson, E. Ozhinsky, Y. Li, I. Park, and J. Crane, "Strategies for rapid in vivo 1h and hyperpolarized 13c mr spectroscopic imaging," *Journal of Magnetic Resonance*, vol. 229, pp. 187–197, 2013.

[102] S. Josan, Y. F. Yen, R. Hurd, A. Pfefferbaum, D. Spielman, and D. Mayer, "Application of double spin echo spiral chemical shift imaging to rapid metabolic mapping of hyperpolarized [1-(1)(3)c]-pyruvate," *Journal of Magnetic Resonance*, vol. 209, no. 2, pp. 332–336, 2011.

[103] J. Leupold, S. Mansson, J. S. Petersson, J. Hennig, and O. Wieben, "Fast multiecho balanced ssfp metabolite mapping of (1)h and hyperpolarized (13)c compounds," *Magnetic Resonance Materials in Physics, Biology and Medicine*, vol. 22, no. 4, pp. 251–256, 2009.

[104] S. Mansson, J. S. Petersson, and K. Scheffler, "Fast metabolite mapping in the pig heart after injection of hyperpolarized 13c-pyruvate with low-flip angle balanced steady-state free precession imaging," *Magnetic Resonance in Medicine*, vol. 68, no. 6, pp. 1894–1899, 2012.

[105] M. Durst, U. Koellisch, C. Gringeri, M. A. Janich, G. Rancan, A. Frank, F. Wiesinger, M. I. Menzel, A. Haase, and R. F. Schulte, "Bolus tracking for improved metabolic imaging of hyperpolarised compounds," *Journal of Magnetic Resonance*, vol. 243, pp. 40–46, 2014.

[106] P. E. Larson, "Flip angle optimization for kinetic modeling," in *Proceedings of the 4th International DNP Symposium, Copenhagen, Denmark*, p. 109, 2013.

[107] C. M. Tsai and D. G. Nishimura, "Reduced aliasing artifacts using variable-density k-space sampling trajectories," *Magnetic Resonance in Medicine*, vol. 43, no. 3, pp. 452–458, 2000.

[108] Q. Qin, "Point spread functions of the t2 decay in k-space trajectories with long echo train," *Magnetic Resonance Imaging*, vol. 30, no. 8, pp. 1134–1142, 2012.

[109] L. Zhao, R. Mulkern, C. H. Tseng, D. Williamson, S. Patz, R. Kraft, R. L. Walsworth, F. A. Jolesz, and M. S. Albert, "Gradient-echo imaging considerations for hyperpolarized 129xe mr," *Journal of Magnetic Resonance, Series B*, vol. 113, no. 2, pp. 179–183, 1996.

[110] S. B. Reeder, J. H. Brittain, T. M. Grist, and Y. F. Yen, "Least-squares chemical shift separation for (13)c metabolic imaging," *Journal of Magnetic Resonance Imaging*, vol. 26, no. 4, pp. 1145–1152, 2007.

[111] B. A. Hargreaves, *Spin-Manipulation Methods for Efficient Magnetic Resonance Imaging*. Ph.d. thesis, Stanford University, 2001.

[112] J. A. Fessler, "On nufft-based gridding for non-cartesian mri," *Journal of Magnetic Resonance*, vol. 188, no. 2, pp. 191–195, 2007.

[113] Y. Xing, G. D. Reed, J. M. Pauly, A. B. Kerr, and P. E. Larson, "Optimal variable flip angle schemes for dynamic acquisition of exchanging hyperpolarized substrates," *Journal of Magnetic Resonance*, vol. 234, pp. 75 – 81, 2013.

[114] L. Z. Li, S. Kadlececk, H. N. Xu, D. Daye, B. Pullinger, H. Profka, L. Chodosh, and R. Rizi, "Ratiometric analysis in hyperpolarized nmr (i): test of the two-site exchange model and the quantification of reaction rate constants," *NMR in Biomedicine*, vol. 26, no. 10, pp. 1308–1320, 2013.

[115] T. K. Foo, M. Saranathan, M. R. Prince, and T. L. Chenevert, "Automated detection of bolus arrival and initiation of data acquisition in fast, three-dimensional, gadolinium-enhanced mr angiography.," *Radiology*, vol. 203, no. 1, pp. 275–280, 1997.

[116] V. B. Ho and T. K. Foo, "Optimization of gadolinium-enhanced magnetic resonance angiography using an automated bolus-detection algorithm (mr smartprep). original investigation," *Investigative Radiology*, vol. 33, no. 9, pp. 515–523, 1998.

[117] V. B. Ho, P. L. Choyke, T. K. Foo, M. N. Hood, D. L. Miller, J. M. Czum, and A. M. Aisen, "Automated bolus chase peripheral mr angiography: initial practical experiences and future directions of this work-in-progress," *Journal of Magnetic Resonance Imaging*, vol. 10, no. 3, pp. 376–388, 1999.

[118] M. L. Zierhut, Y. F. Yen, A. P. Chen, R. Bok, M. J. Albers, V. Zhang, J. Tropp, I. Park, D. B. Vigneron, J. Kurhanewicz, R. E. Hurd, and S. J. Nelson, "Kinetic modeling of hyperpolarized 13c1-pyruvate metabolism in normal rats and tramp mice," *Journal of Magnetic Resonance*, vol. 202, no. 1, pp. 85–92, 2010.

[119] O. Khegai, R. F. Schulte, M. A. Janich, M. I. Menzel, E. Farrell, A. M. Otto, J. H. Ardenkjaer-Larsen, S. J. Glaser, A. Haase, M. Schwaiger, and F. Wiesinger, "Apparent rate constant mapping using hyperpolarized [1-(13)c]pyruvate," *NMR in Biomedicine*, vol. 27, no. 10, pp. 1256–1265, 2014.

[120] D. K. Hill, M. R. Orton, E. Mariotti, J. K. Boult, R. Panek, M. Jafar, H. G. Parkes, Y. Jamin, M. F. Miniotis, N. M. Al-Saffar, M. Beloueche-Babari, S. P. Robinson, M. O. Leach, Y. L. Chung, and T. R. Eykyn, "Model free approach to kinetic analysis of real-time hyperpolarized 13c magnetic resonance spectroscopy data," *PLoS One*, vol. 8, no. 9, p. e71996, 2013.

[121] M. A. Janich, M. I. Menzel, F. Wiesinger, E. Weidl, O. Khegai, J. H. Ardenkjaer-Larsen, S. J. Glaser, A. Haase, R. F. Schulte, and M. Schwaiger, "Effects of pyruvate dose on in vivo metabolism and quantification of hyperpolarized (1)(3)c spectra," *NMR in Biomedicine*, vol. 25, no. 1, pp. 142–151, 2012.

[122] K. Derby, J. Tropp, and C. Hawryszko, "Design and evaluation of a novel dual-tuned resonator for spectroscopic imaging," *Journal of Magnetic Resonance*, vol. 86, no. 3, pp. 645–651, 1990.

[123] M. A. Schroeder, H. J. Atherton, D. R. Ball, M. A. Cole, L. C. Heather, J. L. Griffin, K. Clarke, G. K. Radda, and D. J. Tyler, "Real-time assessment of krebs cycle metabolism using hyperpolarized 13c magnetic resonance spectroscopy," *FASEB Journal*, vol. 23, no. 8, pp. 2529–2538, 2009.

[124] D. J. Tyler, M. A. Schroeder, L. E. Cochlin, K. Clarke, and G. K. Radda, "Application of hyperpolarized magnetic resonance in the study of cardiac metabolism," *Applied Magnetic Resonance*, vol. 34, no. 3-4, pp. 523–531, 2008.

[125] H. J. Atherton, M. S. Dodd, L. C. Heather, M. A. Schroeder, J. L. Griffin, G. K. Radda, K. Clarke, and D. J. Tyler, "Role of pyruvate dehydrogenase inhibition in the development of hypertrophy in the hyperthyroid rat heart: a combined magnetic resonance imaging and hyperpolarized magnetic resonance spectroscopy study," *Circulation*, vol. 123, no. 22, pp. 2552–2561, 2011.

[126] A. P. Chen, R. E. Hurd, M. A. Schroeder, A. Z. Lau, Y. P. Gu, W. W. Lam, J. Barry, J. Tropp, and C. H. Cunningham, "Simultaneous investigation of cardiac pyruvate dehydrogenase flux, krebs cycle metabolism and ph, using hyperpolarized [1,2-(13)c2]pyruvate in vivo," *NMR in Biomedicine*, vol. 25, no. 2, pp. 305–311, 2012.

[127] M. A. Schroeder, A. Z. Lau, A. P. Chen, Y. Gu, J. Nagendran, J. Barry, X. Hu, J. R. Dyck, D. J. Tyler, K. Clarke, K. A. Connelly, G. A. Wright, and C. H. Cunningham, "Hyperpolarized (13)c magnetic resonance reveals early- and late-onset changes to in vivo pyruvate metabolism in the failing heart," *European Journal of Heart Failure*, vol. 15, no. 2, pp. 130–140, 2013.

[128] A. Z. Lau, A. P. Chen, J. Barry, J. J. Graham, W. Dominguez-Viqueira, N. R. Ghugre, G. A. Wright, and C. H. Cunningham, "Reproducibility study for free-breathing measurements of pyruvate metabolism using hyperpolarized (13) c in the heart," *Magnetic Resonance in Medicine*, vol. 69, no. 4, pp. 1063–1071, 2013.

[129] D. K. Sodickson and W. J. Manning, "Simultaneous Acquisition of Spatial Harmonics (SMASH): Fast Imaging with Radiofrequency Coil Arrays," *Magnetic Resonance in Medicine*, vol. 38, no. 4, pp. 591–603, 1997.

[130] M. A. Griswold, P. M. Jakob, M. Nittka, J. W. Goldfarb, and A. Haase, "Partially parallel imaging with localized sensitivities (PILS)," *Magnetic Resonance in Medicine*, vol. 44, no. 4, pp. 602–609, 2000.

[131] S. Kozerke and J. Tsao, "Reduced data acquisition methods in cardiac imaging," *Topics in Magnetic Resonance Imaging*, vol. 15, no. 3, pp. 161–168, 2004.

[132] S. Kozerke, J. Tsao, R. Razavi, and P. Boesiger, "Accelerating cardiac cine 3d imaging using k-t blast," *Magnetic Resonance in Medicine*, vol. 52, no. 1, pp. 19–26, 2004.

[133] F. A. Breuer, P. Kellman, M. A. Griswold, and P. M. Jakob, "Dynamic autocalibrated parallel imaging using temporal grappa (tgrappa)," *Magnetic Resonance in Medicine*, vol. 53, no. 4, pp. 981–985, 2005.

[134] M. Lustig, J. Santos, D. Donoho, and J. Pauly, "k-t sparse: high frame rate dynamic mri exploiting spatio-temporal sparsity," in *Proceedings of the 14th Annual Meeting of ISMRM*, p. 2420, 2006.

[135] A. Arunachalam, D. Whitt, K. Fish, R. Giaquinto, J. Piel, R. Watkins, and I. Hancu, "Accelerated spectroscopic imaging of hyperpolarized c-13 pyruvate using sense parallel imaging," *NMR in Biomedicine*, vol. 22, no. 8, pp. 867–873, 2009.

[136] J. Tropp, J. M. Lupo, A. Chen, P. Calderon, D. McCune, T. Grafendorfer, E. Ozturk-Isik, P. E. Larson, S. Hu, Y. F. Yen, F. Robb, R. Bok, R. Schulte, D. Xu, R. Hurd, D. Vigneron, and S. Nelson, "Multi-channel metabolic imaging, with sense reconstruction, of hyperpolarized [1-(13)c] pyruvate in a live rat at 3.0 tesla on a clinical mr scanner," *Journal of Magnetic Resonance*, vol. 208, no. 1, pp. 171–177, 2011.

[137] M. A. Ohliger, P. E. Z. Larson, R. A. Bok, P. Shin, S. Hu, J. Tropp, F. Robb, L. Carvajal, S. J. Nelson, J. Kurhanewicz, and D. B. Vigneron, "Combined parallel and partial fourier mr reconstruction for accelerated 8-channel hyperpolarized

carbon-13 in vivo magnetic resonance spectroscopic imaging (mrsi)," *Journal of Magnetic Resonance Imaging*, vol. 38, no. 3, pp. 701–713, 2013.

[138] R. F. Lee, G. Johnson, R. I. Grossman, B. Stoeckel, R. Trampel, and G. McGuinness, "Advantages of parallel imaging in conjunction with hyperpolarized helium–a new approach to mri of the lung," *Magnetic Resonance in Medicine*, vol. 55, no. 5, pp. 1132–1141, 2006.

[139] P. J. Shin, P. E. Z. Larson, M. A. Ohliger, M. Elad, J. M. Pauly, D. B. Vigneron, and M. Lustig, "Calibrationless parallel imaging reconstruction based on structured low-rank matrix completion," *Magnetic Resonance in Medicine*, vol. 72, no. 4, pp. 959–970, 2014.

[140] D. Mayer, D. H. Kim, D. M. Spielman, and R. Bammer, "Fast parallel spiral chemical shift imaging at 3t using iterative sense reconstruction," *Magnetic Resonance in Medicine*, vol. 59, no. 4, pp. 891–897, 2008.

[141] L. Menichetti, F. Frijia, V. Lionetti, M. Santarelli, J. H. Ardenkjaer Larsen, G. Giovannetti, V. Positano, D. De Marchi, G. Aquaro, M. Campan, V. Hartwig, M. Milanesi, F. Recchia, L. Landini, and M. Lombardi, "Cardiac metabolism with hyperpolarized [1-13c]pyruvate: a feasibility study in mini-pig with a large dose injection," *Journal of Cardiovascular Magnetic Resonance*, vol. 12, no. Suppl 1, p. T7, 2010.

[142] E. Ferrannini, D. Santoro, R. Bonadonna, A. Natali, O. Parodi, and P. G. Camici, "Metabolic and hemodynamic effects of insulin on human hearts," *American Journal of Physiology*, vol. 264, no. 2 Pt 1, pp. E308–315, 1993.

[143] G. S. Denyer, "Heterogeneous responses to an intravenous glucose load," *The International Journal of Biochemistry & Cell Biology*, vol. 27, no. 9, pp. 981–986, 1995.

[144] M. Durst, E. Chiavazza, A. Haase, S. Aime, M. Schwaiger, and R. F. Schulte, "α-trideuteromethyl[15N]glutamine: A long-lived hyperpolarized perfusion marker," *Magnetic Resonance in Medicine*, vol. 76, no. 6, pp. 1900–1904, 2016.

[145] E. D. Becker and R. R. Shoup, "13c nmr spectroscopy: relaxation times of 13c and methods for sensitivity enhancement," *Pure Applied Chemistry*, vol. 32, no. 1-4, pp. 51–66, 1972.

[146] E. Johansson, S. Mansson, R. Wirestam, J. Svensson, J. S. Petersson, K. Golman, and F. Stahlberg, "Cerebral perfusion assessment by bolus tracking using hyperpolarized 13c," *Magnetic Resonance in Medicine*, vol. 51, no. 3, pp. 464–472, 2004.

[147] A. K. Grant, E. Vinogradov, X. Wang, R. E. Lenkinski, and D. C. Alsop, "Perfusion imaging with a freely diffusible hyperpolarized contrast agent," *Magnetic Resonance in Medicine*, vol. 66, no. 3, pp. 746–755, 2011.

113

[148] C. von Morze, R. A. Bok, J. M. Sands, J. Kurhanewicz, and D. B. Vigneron, "Monitoring urea transport in rat kidney in vivo using hyperpolarized (1)(3)c magnetic resonance imaging," *American journal of physiology. Renal physiology*, vol. 302, no. 12, pp. F1658–1662, 2012.

[149] C. von Morze, P. E. Larson, S. Hu, H. A. Yoshihara, R. A. Bok, A. Goga, J. H. Ardenkjaer-Larsen, and D. B. Vigneron, "Investigating tumor perfusion and metabolism using multiple hyperpolarized (13)c compounds: Hp001, pyruvate and urea," *Magnetic Resonance Imaging*, vol. 30, no. 3, pp. 305–311, 2012.

[150] G. D. Reed, C. von Morze, R. Bok, B. L. Koelsch, M. Van Criekinge, K. J. Smith, S. Hong, P. E. Larson, J. Kurhanewicz, and D. B. Vigneron, "High resolution (13)c mri with hyperpolarized urea: in vivo t(2) mapping and (15)n labeling effects," *IEEE Transactions on Medical Imaging*, vol. 33, no. 2, pp. 362–371, 2014.

[151] K. H. Rahn, S. Heidenreich, and D. Bruckner, "How to assess glomerular function and damage in humans," *Journal of Hypertension*, vol. 17, no. 3, pp. 309–317, 1999.

[152] D. R. Luke, C. E. Halstenson, J. A. Opsahl, and G. R. Matzke, "Validity of creatinine clearance estimates in the assessment of renal function," *Clinical Pharmacology & Therapeutics*, vol. 48, no. 5, pp. 503–508, 1990.

[153] P. L. Choyke, H. A. Austin, J. A. Frank, M. E. Girton, R. L. Diggs, A. J. Dwyer, L. Miller, R. Nussenblatt, H. McFarland, and T. Simon, "Hydrated clearance of gadolinium-dtpa as a measurement of glomerular filtration rate," *Kidney International*, vol. 41, no. 6, pp. 1595–1598, 1992.

[154] E. Durand and A. Prigent, "The basics of renal imaging and function studies," *The Quarterly Journal of Nuclear Medicine and Molecular Imaging*, vol. 46, no. 4, pp. 249–267, 2002.

[155] C. Cudalbu, A. Comment, F. Kurdzesau, R. B. van Heeswijk, K. Uffmann, S. Jannin, V. Denisov, D. Kirik, and R. Gruetter, "Feasibility of in vivo 15n mrs detection of hyperpolarized 15n labeled choline in rats," *Physical Chemistry Chemical Physics*, vol. 12, no. 22, pp. 5818–5823, 2010.

[156] L. Darrasse and J.-C. Ginefri, "Perspectives with cryogenic {RF} probes in biomedical {MRI}," *Biochimie*, vol. 85, no. 9, pp. 915–937, 2003.

[157] D. Groshar, O. M. Embon, A. Frenkel, and D. Front, "Renal function and technetium-99m-dimercaptosuccinic acid uptake in single kidneys: the value of in vivo spect quantitation," *Journal of Nuclear Medicine*, vol. 32, no. 5, pp. 766–768, 1991.

[158] M. R. Prince, C. Arnoldus, and J. K. Frisoli, "Nephrotoxicity of high-dose gadolinium compared with iodinated contrast," *Journal of Magnetic Resonance Imaging*, vol. 6, no. 1, pp. 162–166, 1996.

[159] L. Bokacheva, H. Rusinek, J. L. Zhang, and V. S. Lee, "Assessment of renal function with dynamic contrast-enhanced mr imaging," *Magnetic Resonance Imaging Clinics of North America*, vol. 16, no. 4, pp. 597–611, viii, 2008.

[160] E. Ledneva, S. Karie, V. Launay-Vacher, N. Janus, and G. Deray, "Renal safety of gadolinium-based contrast media in patients with chronic renal insufficiency," *Radiology*, vol. 250, no. 3, pp. 618–628, 2009.

[161] M. Durst, U. Koellisch, V. Daniele, K. Steiger, M. Schwaiger, A. Haase, M. I. Menzel, R. F. Schulte, S. Aime, and F. Reineri, "Probing lactate secretion in tumours with hyperpolarised NMR," *NMR in Biomedicine*, vol. 29, no. 8, pp. 1079–1087, 2016.

[162] A. P. Halestrap and N. T. Price, "The proton-linked monocarboxylate transporter (mct) family: structure, function and regulation," *Biochemical Journal*, vol. 343 Pt 2, pp. 281–299, 1999.

[163] V. Quennet, A. Yaromina, D. Zips, A. Rosner, S. Walenta, M. Baumann, and W. Mueller-Klieser, "Tumor lactate content predicts for response to fractionated irradiation of human squamous cell carcinomas in nude mice," *Radiotherapy & Oncology*, vol. 81, no. 2, pp. 130–135, 2006.

[164] J. Grotius, C. Dittfeld, M. Huether, W. Mueller-Klieser, M. Baumann, and L. A. Kunz-Schughart, "Impact of exogenous lactate on survival and radioresponse of carcinoma cells in vitro," *International Journal of Radiation Biology*, vol. 85, no. 11, pp. 989–1001, 2009.

[165] U. G. Sattler, S. S. Meyer, V. Quennet, C. Hoerner, H. Knoerzer, C. Fabian, A. Yaromina, D. Zips, S. Walenta, M. Baumann, and W. Mueller-Klieser, "Glycolytic metabolism and tumour response to fractionated irradiation," *Radiotherapy & Oncology*, vol. 94, no. 1, pp. 102–109, 2010.

[166] G. Schwickert, S. Walenta, K. Sundfor, E. K. Rofstad, and W. Mueller-Klieser, "Correlation of high lactate levels in human cervical cancer with incidence of metastasis," *Cancer Research*, vol. 55, no. 21, pp. 4757–4759, 1995.

[167] S. Walenta, M. Wetterling, M. Lehrke, G. Schwickert, K. Sundfor, E. K. Rofstad, and W. Mueller-Klieser, "High lactate levels predict likelihood of metastases, tumor recurrence, and restricted patient survival in human cervical cancers," *Cancer Research*, vol. 60, no. 4, pp. 916–921, 2000.

[168] D. M. Brizel, T. Schroeder, R. L. Scher, S. Walenta, R. W. Clough, M. W. Dewhirst, and W. Mueller-Klieser, "Elevated tumor lactate concentrations predict for an increased risk of metastases in head-and-neck cancer," *International Journal of Radiation Oncology Biology Physics*, vol. 51, no. 2, pp. 349–353, 2001.

[169] K. Goetze, S. Walenta, M. Ksiazkiewicz, L. A. Kunz-Schughart, and W. Mueller-Klieser, "Lactate enhances motility of tumor cells and inhibits monocyte migration and cytokine release," *International Journal of Oncology*, vol. 39, no. 2, pp. 453–463, 2011.

[170] F. Baumann, P. Leukel, A. Doerfelt, C. P. Beier, K. Dettmer, P. J. Oefner, M. Kastenberger, M. Kreutz, T. Nickl-Jockschat, U. Bogdahn, A. K. Bosserhoff, and P. Hau, "Lactate promotes glioma migration by tgf-beta2-dependent regulation of matrix metalloproteinase-2," *Neuro-Oncology*, vol. 11, no. 4, pp. 368–380, 2009.

[171] S. Beckert, F. Farrahi, R. S. Aslam, H. Scheuenstuhl, A. Konigsrainer, M. Z. Hussain, and T. K. Hunt, "Lactate stimulates endothelial cell migration," *Wound Repair and Regeneration*, vol. 14, no. 3, pp. 321–324, 2006.

[172] R. Boidot, F. Vegran, A. Meulle, A. Le Breton, C. Dessy, P. Sonveaux, S. Lizard-Nacol, and O. Feron, "Regulation of monocarboxylate transporter mct1 expression by p53 mediates inward and outward lactate fluxes in tumors," *Cancer Research*, vol. 72, no. 4, pp. 939–948, 2012.

[173] S. Walenta and W. F. Mueller-Klieser, "Lactate: mirror and motor of tumor malignancy," *Seminars in Radiation Oncology*, vol. 14, no. 3, pp. 267–274, 2004.

[174] E. Gottfried, L. A. Kunz-Schughart, S. Ebner, W. Mueller-Klieser, S. Hoves, R. Andreesen, A. Mackensen, and M. Kreutz, "Tumor-derived lactic acid modulates dendritic cell activation and antigen expression," *Blood*, vol. 107, no. 5, pp. 2013–2021, 2006.

[175] K. Fischer, P. Hoffmann, S. Voelkl, N. Meidenbauer, J. Ammer, M. Edinger, E. Gottfried, S. Schwarz, G. Rothe, S. Hoves, K. Renner, B. Timischl, A. Mackensen, L. Kunz-Schughart, R. Andreesen, S. W. Krause, and M. Kreutz, "Inhibitory effect of tumor cell-derived lactic acid on human t cells," *Blood*, vol. 109, no. 9, pp. 3812–3819, 2007.

[176] K. Dietl, K. Renner, K. Dettmer, B. Timischl, K. Eberhart, C. Dorn, C. Hellerbrand, M. Kastenberger, L. A. Kunz-Schughart, P. J. Oefner, R. Andreesen, E. Gottfried, and M. P. Kreutz, "Lactic acid and acidification inhibit tnf secretion and glycolysis of human monocytes," *The Journal of Immunology*, vol. 184, no. 3, pp. 1200–1209, 2010.

[177] F. Hirschhaeuser, U. G. Sattler, and W. Mueller-Klieser, "Lactate: a metabolic key player in cancer," *Cancer Research*, vol. 71, no. 22, pp. 6921–6925, 2011.

[178] C. Pinheiro, A. Longatto-Filho, J. Azevedo-Silva, M. Casal, F. C. Schmitt, and F. Baltazar, "Role of monocarboxylate transporters in human cancers: state of the art," *Journal of Bioenergetics and Biomembranes*, vol. 44, no. 1, pp. 127–139, 2012.

[179] N. Pertega-Gomes and F. Baltazar, "Lactate transporters in the context of prostate cancer metabolism: what do we know?," *International Journal of Molecular Sciences*, vol. 15, no. 10, pp. 18333–18348, 2014.

[180] F. Baltazar, C. Pinheiro, F. Morais-Santos, J. Azevedo-Silva, O. Queiros, A. Preto, and M. Casal, "Monocarboxylate transporters as targets and mediators in cancer therapy response," *Histology and Histopathology*, vol. 29, no. 12, pp. 1511–1524, 2014.

[181] R. A. Coss, C. W. Storck, C. Daskalakis, D. Berd, and M. L. Wahl, "Intracellular acidification abrogates the heat shock response and compromises survival of human melanoma cells," *Molecular Cancer Therapeutics*, vol. 2, no. 4, pp. 383–388, 2003.

[182] C. B. Colen, N. Seraji-Bozorgzad, B. Marples, M. P. Galloway, A. E. Sloan, and S. P. Mathupala, "Metabolic remodeling of malignant gliomas for enhanced sensitization during radiotherapy: an in vitro study," *Neurosurgery*, vol. 59, no. 6, pp. 1313–1323; discussion 1323–1324, 2006.

[183] S. P. Mathupala, C. B. Colen, P. Parajuli, and A. E. Sloan, "Lactate and malignant tumors: a therapeutic target at the end stage of glycolysis," *Journal of Bioenergetics and Biomembranes*, vol. 39, no. 1, pp. 73–77, 2007.

[184] C. B. Colen, Y. Shen, F. Ghoddoussi, P. Yu, T. B. Francis, B. J. Koch, M. D. Monterey, M. P. Galloway, A. E. Sloan, and S. P. Mathupala, "Metabolic targeting of lactate efflux by malignant glioma inhibits invasiveness and induces necrosis: an in vivo study," *Neoplasia*, vol. 13, no. 7, pp. 620–632, 2011.

[185] T. Harris, G. Eliyahu, L. Frydman, and H. Degani, "Kinetics of hyperpolarized 13c1-pyruvate transport and metabolism in living human breast cancer cells," *Proceedings of the National Academy of Sciences of the United States of America*, vol. 106, no. 43, pp. 18131–18136, 2009.

[186] K. R. Keshari, R. Sriram, B. L. Koelsch, M. Van Criekinge, D. M. Wilson, J. Kurhanewicz, and Z. J. Wang, "Hyperpolarized 13c-pyruvate magnetic resonance reveals rapid lactate export in metastatic renal cell carcinomas," *Cancer Research*, vol. 73, no. 2, pp. 529–538, 2013.

[187] M. I. Kettunen, D.-e. Hu, T. H. Witney, R. McLaughlin, F. A. Gallagher, S. E. Bohndiek, S. E. Day, and K. M. Brindle, "Magnetization transfer measurements of exchange between hyperpolarized [1-13c]pyruvate and [1-13c]lactate in a murine lymphoma," *Magnetic Resonance in Medicine*, vol. 63, no. 4, pp. 872–880, 2010.

[188] S. Hu, M. Zhu, H. A. Yoshihara, D. M. Wilson, K. R. Keshari, P. Shin, G. Reed, C. von Morze, R. Bok, P. E. Larson, J. Kurhanewicz, and D. B. Vigneron, "In vivo measurement of normal rat intracellular pyruvate and lactate levels after injection of hyperpolarized [1-(13)c]alanine," *Magnetic Resonance Imaging*, vol. 29, no. 8, pp. 1035–1040, 2011.

[189] M. R. Smith, E. T. Peterson, J. W. Gordon, D. J. Niles, I. J. Rowland, K. N. Kurpad, and S. B. Fain, "In vivo imaging and spectroscopy of dynamic metabolism using simultaneous 13c and 1h mri," *IEEE Transactions on Biomedical Engineering*, vol. 59, no. 1, pp. 45–49, 2012.

[190] M. I. Kettunen, B. W. Kennedy, D. E. Hu, and K. M. Brindle, "Spin echo measurements of the extravasation and tumor cell uptake of hyperpolarized [1-(13) c]lactate and [1-(13) c]pyruvate," *Magnetic Resonance in Medicine*, vol. 70, no. 5, pp. 1200–1209, 2013.

[191] Y. F. Yen, P. Le Roux, D. Mayer, R. King, D. Spielman, J. Tropp, K. Butts Pauly, A. Pfefferbaum, S. Vasanawala, and R. Hurd, "T(2) relaxation times of (13)c metabolites in a rat hepatocellular carcinoma model measured in vivo using (13)c-mrs of hyperpolarized [1-(13)c]pyruvate," *NMR in Biomedicine*, vol. 23, no. 4, pp. 414–423, 2010.

[192] F. Schilling, S. Duwel, U. Kollisch, M. Durst, R. F. Schulte, S. J. Glaser, A. Haase, A. M. Otto, and M. I. Menzel, "Diffusion of hyperpolarized (13) c-metabolites in tumor cell spheroids using real-time nmr spectroscopy," *NMR in Biomedicine*, vol. 26, no. 5, pp. 557–568, 2013.

[193] L. V. Sogaard, F. Schilling, M. A. Janich, M. I. Menzel, and J. H. Ardenkjaer-Larsen, "In vivo measurement of apparent diffusion coefficients of hyperpolarized (1)(3)c-labeled metabolites," *NMR in Biomedicine*, vol. 27, no. 5, pp. 561–569, 2014.

[194] E. Adamson, J. Gordon, K. Johnson, and S. Fain, "Su-e-qi-11: Measurement of renal pyruvate-to-lactate exchange with hyperpolarized 13c mri," *Medical Physics*, vol. 41, no. 6, pp. 379–379, 2014.

[195] P. E. Larson, R. E. Hurd, A. B. Kerr, J. M. Pauly, R. A. Bok, J. Kurhanewicz, and D. B. Vigneron, "Perfusion and diffusion sensitive 13c stimulated-echo mrsi for metabolic imaging of cancer," *Magnetic Resonance Imaging*, vol. 31, no. 5, pp. 635–642, 2013.

[196] B. L. Koelsch, G. D. Reed, K. R. Keshari, M. M. Chaumeil, R. Bok, S. M. Ronen, D. B. Vigneron, J. Kurhanewicz, and P. E. Larson, "Rapid in vivo apparent diffusion coefficient mapping of hyperpolarized 13 c metabolites," *Magnetic Resonance in Medicine*, 2014.

[197] E. Terreno, M. Botta, F. Fedeli, B. Mondino, L. Milone, and S. Aime, "Enantioselective recognition between chiral alpha-hydroxy-carboxylates and macrocyclic heptadentate lanthanide(iii) chelates," *Inorganic Chemistry*, vol. 42, no. 16, pp. 4891–4897, 2003.

[198] C. Gabellieri, M. O. Leach, and T. R. Eykyn, "Modulating the relaxivity of hyperpolarized substrates with gadolinium contrast agents," *Contrast Media & Molecular Imaging*, vol. 4, no. 3, pp. 143–147, 2009.

[199] "https://commons.wikimedia.org/wiki/File:Gadobutrol_skeletal.svg," Sept. 2015.

[200] K.-S. Dimmer, B. Friedrich, F. Lang, J. W. Deitmer, and S. Bröer, "The low-affinity monocarboxylate transporter mct4 is adapted to the export of lactate in highly glycolytic cells," *Biochemical Journal*, vol. 350, no. 1, pp. 219–227, 2000.

[201] M. S. Ullah, A. J. Davies, and A. P. Halestrap, "The plasma membrane lactate transporter mct4, but not mct1, is up-regulated by hypoxia through a hif-1alpha-dependent mechanism," *Journal of Biological Chemistry*, vol. 281, no. 14, pp. 9030–9037, 2006.

[202] S. Broer, "Adaptation of plasma membrane amino acid transport mechanisms to physiological demands," *Pflugers Archiv*, vol. 444, no. 4, pp. 457–466, 2002.

[203] D. B. Shennan, S. A. McNeillie, and D. E. Curran, "The effect of a hyposmotic shock on amino acid efflux from lactating rat mammary tissue: stimulation of taurine and glycine efflux via a pathway distinct from anion exchange and volume-activated anion channels," *Experimental Physiology*, vol. 79, no. 5, pp. 797–808, 1994.

[204] K. Lohmann, "über die pyrophosphatfraktion im muskel," *Naturwissenschaften*, vol. 17, no. 31, pp. 624–625, 1929.

[205] P. Mansfield, "Spatial mapping of the chemical shift in nmr," *Magnetic Resonance in Medicine*, vol. 1, no. 3, pp. 370–86, 1984.

[206] J. W. T. James W. Cooley, "An algorithm for the machine calculation of complex fourier series," *Mathematics of Computation*, vol. 19, no. 90, pp. 297–301, 1965.

[207] E. L. Hahn, "Nuclear induction due to free larmor precession," *Physical Review*, vol. 77, pp. 297–298, 1950.

[208] T. R. Brown, B. M. Kincaid, and K. Ugurbil, "Nmr chemical shift imaging in three dimensions," *Proceedings of the National Academy of Sciences*, vol. 79, no. 11, pp. 3523–3526, 1982.

[209] S. B. Reeder, A. R. Pineda, Z. Wen, A. Shimakawa, H. Yu, J. H. Brittain, G. E. Gold, C. H. Beaulieu, and N. J. Pelc, "Iterative decomposition of water and fat with echo asymmetry and least-squares estimation (ideal): application with fast spin-echo imaging," *Magnetic Resonance in Medicine*, vol. 54, no. 3, pp. 636–44, 2005.

[210] M. Hutchinson and U. Raff, "Fast mri data acquisition using multiple detectors," *Magnetic Resonance in Medicine*, vol. 6, no. 1, pp. 87–91, 1988.

[211] H. Y. Carr, "Steady-state free precession in nuclear magnetic resonance," *Physical Review*, vol. 112, pp. 1693–1701, 1958.

[212] E. Adalsteinsson, P. Irarrazabal, S. Topp, C. Meyer, A. Macovski, and D. M. Spielman, "Volumetric spectroscopic imaging with spiral-based k-space trajectories," *Magnetic Resonance in Medicine*, vol. 39, no. 6, pp. 889–98, 1998.

List of Frequently Used Abbreviations

- **ATP** adenosine triphosphate [204]

- **CSI** chemical shift imaging

- **CT** computed tomography

- **DNP** dynamic nuclear polarisation [40]

- **EPSI** echo-planar spectroscopic imaging [205]

- **FFT** fast Fourier transform [206]

- **FID** free induction decay [207]

- **FIDCSI** free induction decay chemical shift imaging [208]

- **FOV** field of view

- **FRFSE** fast-recovery fast spin-echo

- **FWHM** full width at half-maximum

- **g-factor** geometry-factor [64]

- **GRE** gradient echo [61]

- **IDEAL** Iterative Decomposition of water and fat with Echo Asymmetry and Least-squares estimation [209]

- **ISPCSI** IDEAL spiral chemical shift imaging [19]

- **MCT** monocarboxylate transporter [162]

- **MRI** magnetic resonance imaging [1, 2]

- **MRS** magnetic resonance spectroscopy [3, 4]

- **NMR** nuclear magnetic resonance [31]

- **NUFFT** non-uniform fast Fourier transform

- **PET** positron emission tomography

- **PMRI** parallel magnetic resonance imaging [210]

- **PSF** point spread function

- **RF** radio-frequency

- **ROI** region of interest

- **SENSE** SENSitivity Encoding [64]

- **SNR** signal-to-noise ratio

- **SSFP** steady-state free precession [211]

- **SPCSI** spiral chemical shift imaging [212]

- **SPIRiT** iTerative Self-consistent Parallel Imaging Reconstruction [65]

- **VFA** variable flip angle

List of Publications

Peer-reviewed Articles

M. Durst, U. Koellisch, C. Gringeri, M. A. Janich, G. Rancan, A. Frank, F. Wiesinger, M. I. Menzel, A. Haase, R. F. Schulte, "Bolus tracking for improved metabolic imaging of hyperpolarised compounds," *Journal of Magnetic Resonance*, vol. 243, pp. 40-46, 2014.

M. Durst[†], U. Koellisch[†], A. Frank, G. Rancan, C. V. Gringeri, V. Karas, F. Wiesinger, M. I. Menzel, M. Schwaiger, A. Haase, R. F. Schulte, "Comparison of acquisition schemes for hyperpolarised ^{13}C imaging," *NMR in Biomedicine*, vol. 28(6), pp. 715-725, 2015.

M. Durst, E. Chiavazza, A. Haase, S. Aime, M. Schwaiger, R. F. Schulte, "α-trideutero-methyl[15N]glutamine: A long-lived hyperpolarized perfusion marker," *Magnetic Resonance in Medicine*, vol. 76(6), pp. 1900-1904, 2016.

M. Durst, U. Koellisch, V. Daniele, K. Steiger, M. Schwaiger, A. Haase, M. I. Menzel, R. F. Schulte, S. Aime, F. Reineri, "Probing lactate secretion in tumours with hyperpolarised NMR," *NMR in Biomedicine*, vol. 29(8), pp. 1079-1087, 2016.

R. F. Schulte, J. I. Sperl, E. Weidl, M. I. Menzel, M. A. Janich, O. Khegai, **M. Durst**, J. H. Ardenkjaer-Larsen, S. J. Glaser, A. Haase, M. Schwaiger, F. Wiesinger, "Saturation-recovery metabolic-exchange rate imaging with hyperpolarized [1-^{13}C] pyruvate using spectral-spatial excitation," *Magnetic Resonance in Medicine*, vol. 69(5), pp. 1209-1216, 2013.

F. Schilling, S. Düwel, U. Köllisch, **M. Durst**, R. F. Schulte, S. J. Glaser, A. Haase, A. M. Otto, M. I. Menzel, "Diffusion of hyperpolarized ^{13}C-metabolites in tumor cell spheroids using real-time NMR spectroscopy," *NMR in Biomedicine*, vol. 26(5), pp. 557-568, 2013.

E. Chiavazza, E. Kubala, C. V. Gringeria, S. Düwel, **M. Durst**, R. F. Schulte, M. I. Menzel, "Earth's magnetic field enabled scalar coupling relaxation of ^{13}C nuclei bound to fast-relaxing quadrupolar ^{14}N in amide groups," *Journal of Magnetic Resonance*, vol. 227, pp. 35-38, 2013.

[†]: authors contributed equally

Conference Contributions (Selection)

M. Durst, E. Chiavazza, A. Haase, S. Aime, M. Schwaiger, R.F. Schulte, "Assessing Kidney Function with Magnetic Resonance Imaging of Hyperpolarised 15N-Glutamine". In: *Proceedings of the 2015 World Molecular Imaging Congress*, Honolulu, USA, 2015. Oral presentation.

M. Durst, "Metabolic MR Imaging with Hyperpolarised 13C Substrates". In: *Proceedings of the 10th European Veterinary MRI-User Meeting*, Merelbeke, Belgium, 2014. Invited talk.

M. Durst, S. Düwel, C.V. Gringeri, Y. Kosanke, C. Gross, R. Braren, A. Haase, M.I. Menzel, R.F. Schulte, "Multiband Excitation Pulses for Treatment Response Studies with Hyperpolarised 13C Fumarate". In: *Proceedings of the 21st Annual Meeting of ISMRM*, Salt Lake City, Utah, USA, 2013. p 1931. Traditional poster.

M. Durst, U. Koellisch, C. Gringeri, M.A. Janich, G. Rancan, A. Frank, F. Wiesinger, M.I. Menzel, A. Haase, R.F. Schulte, "Bolus Tracking for Improved Metabolic Imaging of Hyperpolarised Compounds". In: *Proceedings of the 22nd Annual Meeting of ISMRM*, Milan, Italy, 2014. p 2796. Traditional poster.

M. Durst, U. Koellisch, F. Reineri, V. Daniele, C. Gringeri, A. Frank, M.I. Menzel, A. Haase, R.F. Schulte, S. Aime, "Investigation of Cell Membrane Transport and Compartmentalisation of Hyperpolarised Metabolites Using a GdDO3A Relaxation Agent". In: *Proceedings of the 22nd Annual Meeting of ISMRM*, Milan, Italy, 2014. p 2762. Traditional poster.

Acknowledgements

I would like to thank

- **Prof. Haase** for giving me the opportunity and supporting me

- **Dr. Rolf Schulte** for technical support and many scientific discussions

- **Dr. Marion Menzel** for administrative care and scientific discussions

- **Dr. Ulrich Koellisch** for help with my experiments and scientific (and not so scientific) discussions

- **Prof. Aime** for providing interesting ideas and projects

- **Stephan Duewel** for teaching me patience and thoroughness

- **Dr. Enrico Chiavazza** for his hard work on new agents

- **Dr. Concetta Gringeri** for chemical expertise

- **Dr. Geoffrey Topping** for technical support at the 7 T scanner

- **Dr. Giaime Rancan** for animal care and widening my philosophical perspective

- **Dr. Kim Munoz Alvarez** for animal care

- **Annette Frank** for animal care

- **Dr. Luca Menichetti, Dr. Francesca Frijia and the hyperpolarisation team of the CNR in Pisa** for experimental support

- **Dr. Ulrich Koellisch, Tim Sprenger, Nicolas Hehn, Benjamin Fuersich, Dr. Johannes Scholz** for intense scientific meetings